PHOTO-INDUCED MOLECULAR REORIENTATION AND PHOTOTHERMAL HEATING AS MECHANISMS OF THE INTENSITY-DEPENDENT REFRACTIVE INDEX IN DYE-DOPED POLYMERS

By

JEONG JOON PARK

A dissertation submitted in partial fulfillment of
the requirements for the degree of

DOCTOR OF PHILOSOPHY

WASHINGTON STATE UNIVERSITY
Department of Physics and Astronomy

MAY 2006

To the Faculty of Washington State University:

The members of the Committee appointed to examine the dissertation of Jeong Joon Park find it satisfactory and recommend that it be accepted.

_____

Chair

_____

_____

ACKNOWLEDGMENTS

I would like to acknowledge the financial support from Army Research Office. Especially, I thank to my advisor, Dr. Mark G. Kuzyk for showing me how to be a good physicist. I also would like to thank to all my classmates for encouraging me and fruitful discussion.

Foremost, I love to thank to my family in Korea, China, Florida, and NYC for their endless love and support.

PHOTO-INDUCED MOLECULAR REORIENTATION AND PHOTOTHERMAL HEATING AS MECHANISMS OF THE INTENSITY-DEPENDENT REFRACTIVE INDEX IN DYE-DOPED POLYMERS

Abstract

by JEONG JOON PARK, Ph.D.
Washington State University
MAY 2006

Chair: Mark G. Kuzyk

In this dissertation we present a new method to distinguish between nonlocal (thermal lens effect) and local (photoisomerization) optical response with modified time-dependent Z-scan (TZ-scan). In our experiments, two dye-doped polymers are used under similar conditions to illustrate the difference of a local and a nonlocal response. We find that photoisomerization in short-time regime can delay the onset of the thermal lens effect by means of energy storage within the molecules.

Contents

List of Figures

List of Tables

Chapter 1

Introduction

1.1 Preliminaries

This dissertation deals with the mechanisms of how light interacts with matter to yield an intensity-dependent refractive index. While the simple interaction between a photon and an atom is well understood, a bulk material made of a dye molecule embedded in a transparent polymer yields novel mechanisms. Light absorbed by the molecule can change its molecular structure while the absorbed energy can diffuse as heat. These are examples of local and nonlocal mechanisms.

A response of a material can be nonlocal in space and time, and a dye doped polymer exhibits both. As we will show in this dissertation, two mechanism dominate: One is local and the other nonlocal, with coupling between them.

First, let's consider the mechanisms from the perspective of their special manifestations. In a local mechanism, the effect of the light on the material is observed at the point of interaction. In a nonlocal process, the response is transmitted through the material away from the illuminated region. An example of a nonlocal effect is photothermal heating. The photothermal heating mechanism has a long and rich history related to gas lasers. For example, researchers developed a calorimetry technique using the thermal lens effect in a

liquid. This line of research started in the 1960's. Photoisomerization, on the other hand, is an example of a local effect. Disperse red 1 (DR1) azo dye is a classic molecule that has been extensively studied for its large reversible shape change in response to heat or excitation by a laser source. We describe its history as a light-sensitive chromophore. Sekkat's model of light-induced photoisomerization is used as a starting point that we generalize as part of this dissertation. Our modifications to his model in the short times and low intensity is found to accurately describe our data. Our theory takes into account the coupling between photothermal heating followed by angular diffusion and photoisomerization. This coupled theory not only describes the dynamics of the observed light-induced refractive index change, but also predicts new phenomena, such as a change in the minimum beam spot in the sample, an effect that we directly measured and confirmed.

1.2 Historical background

Optics is the branch of physics that studies the light. Historically, ray optics was a good approximation to observation until diffraction required the development of wave optics which led eventually to Maxwell's equations. More recently, the particle nature of light has led to the development of quantum optics. The quantum theory of light and matter made the invention of the MASER (Microwave Amplification by Stimulated Emission of Radiation) possible which led to the first LASER (Light Amplification by Stimulated Emission of Radiation) and shorter wavelength light sources.

One subbranch of optics is nonlinear optics (NLO). Taking advantage of the invention of the laser, the high intensities available make it possible to study nonlinear effects where laser field strengths are a large fraction of typical fields in a molecule. Some applications made possible by nonlinear optics are realtime holography, optical switching, optical fiber communication, etc. In many applications, such as optical communications, large bandwidth is required. To achieve large bandwidth, the response time for the device is required to be

short, which makes signal recognition a challenge.[1][2] To have both a fast response and a large signals appears incompatible.[3] The strength of a nonlinear process is determined by the nonlinear susceptibility, which appears to be bounded by a fundamental limit.[4][5]

1.2.1 Materials

Inorganic and organic materials are two broad classes of nonlinear-optical materials. Our work focused on organic dye-doped polymers. Polymers have several advantage over inorganic materials: They are inexpensive, have good optical quality, and have a low glass transition temperature compared to silica so they can easily be processed to make large-area thin films and fibers. Furthermore, the low glass transition temperature allows the polymer to be doped with organic chromophores with large nonlinear optical response. We use the azobenzene DR1 because of its chemical stability and large nonlinear susceptibility due to trans-cis conversion through photoisomerization.

1.2.2 Physics

Second harmonic generation was first observed the nonlinear optical effect in 1961, shortly after the first working laser was made by Maiman in 1960.[6] In early laser systems, stability and reliability were important issues. Gordon observed the first thermal lens effect by inserting polar or nonpolar liquid cells in the resonator of a HeNe laser.[7] Akhmanov explained self-focusing in cubic nonlinear media with 2-D and 3-D gaussian beams in the parabolic approximation.[8][9] Harris performed an experiment measuring thermally induced beam distortion by solvents used in calorimetry.[10] At the time, these nonlinear processes were found to be a nuisance in making reliable lasers. Today, they are central to the design of optical devices.

1.3 Motivation

1.3.1 The Z-scan technique

Sheik-Bahae developed a technique called Z-scan to measure nonlinear refraction. In the Z-scan experiment, a laser beam is focused into a sample and the intensity measured through an aperture while the sample is translated along the beam axis, hence the name Z-scan. He modelled the experimental geometry and found that the technique has high sensitivity and easily determines the sign and magnitude of nonlinear refraction.[11]

Castillo used pump-probe time-resolved Z-scan to study the thermal changes in refractive index originates from one- and two-photon absorption in organic solvents. In their experiment, a strong pump beam induces a refractive index change in the sample while a colinear weak probe beam is measured through the aperture. By using pulsed light, the temporal dependence of the signal could be measured allowing the pure thermal signal to be determined.[12]

Zhang studied the nonlinear refractive index n_2 of two push-pull azobenzenes, which have a similar molecular structure to DR1, using the single beam Z-scan method and suggested that the origins of the large nonlinear optical response of the two doped polymer materials are found to be cis-trans interconversion.[13]

After Catunda developed a method to distinguish between the thermal and nonthermal lens effect with a transient Z-scan measurement by using a chopper in Argon laser, which allowed the thermal lensing effect to be determined.[14] Mendonca developed a more advanced method. That uses a Fourier analysis of the transmitted time evolution at various chopper frequencies at off resonance wavelengths and found the mechanism to be a thermal effect.[15] An analysis of the data showed that the thermal diffusivity coefficient in DR1-doped polystyrene contradicts the mechanism proposed by Zhang.

Falconieri studied the effects on Z-scan measurements of thermo-optical nonlinearities due to cumulative heating in a liquid CS_2 sample with a femtosecond mode-locked Ti:Sappire

laser. At short times ($15\mu s$), a positive nonlinear refractive index is observed, but at longer times ($150 - 200\mu s$), a large negative nonlinear refractive index is observed. Given that each mechanism has a distinct sign and response time. Due to the opposite sign, it was possible to separate the two mechanisms.[16][17]

Recently, Gnoli found that with a high repetition rate laser (76 MHz repetition rate with 120 fs pulse width) the cumulative thermal effects in CS_2 and toluence could be controlled by the method used by Falconieri.[18]

Cuppo analyzed intensity-dependent optical nonlinearities of the thermal lens model of Gorden and the Z-scan model (a gaussian decomposition analysis) of Sheik-Bahae. The thermal-lens model is nonlocal in space and time, whereas the Gaussian decomposition is dependent on a strictly local response. Limitations of these models in describing Z-scan experiments on systems with nonlocal response are discussed in the literature.[19]

Most recently, Z-scan with a CW laser (He-Ne) was used for the investigation of the refractive index change associated with the photoisomerization of azobenzene polymers (disperse red 13-doped PMMA film). By using circularly and linearly polarized light, from the ratio of the nonlinear refractive index due to the two polarized lights the dominant mechanism is found to be photoisomerization.[20]

1.3.2 Mechanisms

Thermal effects are generally any kind of effects that are caused by a change in temperature. Specifically, we are interested in two types of thermal effect. One is the thermal lens effect, which is caused by temperature gradients. This occurs when light energy is absorbed by the material and dissipated as heat. The second effect is the process by which thermal agitation randomizes the orientation of molecules.

Due to a small potential barrier between the trans and cis isomer of an azo dye, the trans isomer can be easily excited to a cis isomer by photons. The related phenomenon of the reversible cis-trans photoisomerization of disperse red 1 (DR1) in PMMA thin films has

been demonstrated previously by using the Attenuated Total Reflection (ATR) method. Two mechanisms are identified in the literature: angular hole burning and angular redistribution of molecules. The evolution of the second-order nonlinear susceptibility, $\chi^{(2)}$, is monitored by measuring the electro-optic effect by attenuated total reflection and by second-harmonic generation.[21][22] For the most complete theoretical study, a phenomenon based on the enhanced mobility of the azo chromophores during the isomerization process is used. It is observed that irradiation with linearly polarized blue light induces a strong anisotropy in an azobenzene-containing polyglutamate film. Also, a theoretical model that describes the trans $\Rightarrow$ cis photoisomerization-induced reorientation of azobenzenes in a viscous environment is presented.[23] A more detailed theoretical study of this phenomenon based on the enhanced mobility of the azo chromophores during the isomerization process is presented including cis $\Rightarrow$ trans photoisomerization and thermal relaxation. Analytical expressions are derived for the photoinduced polar order and its related anisotropy for both cis and trans molecular distributions.[24] Recently, Sekkat and Knoll summarized all their work and other related recent work in photorefractive materials in films.[25]

1.4 Organization

Chapter 2 starts with the theory of geometrical optics in a nonlinear medium using Akhmanov's model under the condition that the radius of curvature of the beam wave front is infinite. By solving a thermal diffusion equation for a heat source that originates directly form a light source with a gaussian profile, the nonlinear refractive index as a function of time is derived. We generalized Sekkat's theory of photoisomerization of a polar azo-dye doped in a polymer in the limit of short time and low intensity. The photothermal effect is included by combining the temperature increase of the thermal lens effect and rotational diffusion of rod-shaped molecules, using the Einstein relation.

In Chapter 3, sample fabrication and experimental procedures such as TZ-scan (Tran-

sient Z-scan or Time-dependent Z-scan) and temperature-dependent OKE experiments are described. The method of fabricating thin slabs of dye-doped PMMA from bulk materials is presented. The method of conversion of transient signals at fixed positions to position-dependent Z-scan curves at fixed times is described. By using this method, the time-dependent nonlinear refractive index is obtained, which we use as a tool to study nonlinear mechanisms. To show time- and temperature-dependency of the refractive index independent of optical excitation, temperature-dependent birefringence measurement using an external, controllable oven is performed.

Chapter 4 presents our results and discusses their implications. Two different chromophores were used in our studies: DR1 and disperse blue 14 (DB14). Their concentrations in PMMA are adjusted so that their absorption coefficients are within the same order of magnitude at their off-resonance wavelengths. This makes it possible to compare sample and aids to separate the thermal lens effect and photoisomerization. In DB14/PMMA, an increase of the effective beam waist is observed that fits our theory, which is developed in Chapter 2 of the nonlinear refractive index due to the thermal lens effect and in Section 3.7 for physical justification. Our modification to the standard theory is motivated by the comparison of the thermal conductivity, κ, of PMMA, to previously published results.[26][27] When the modification of the beam waist as a function of time is taken account aside from discrepancies due to the boundary of the air/sample interface which is not included in our theory. In DR1/PMMA, TZ-scan data agrees with the theory developed in Chapter 2. By using circularly and linearly polarized beams, polarization-dependent and -independent mechanisms are demonstrated. In the polarization-dependent mechanism, a linearly polarized beam shows more influence than a circularly polarized beam on quantum yield. The ratio of the quantum yields and that of the nonlinear refractive indices as a function of time are compared with values of the index ratios given in literature,[20] and good agreements is found.

For the polarization-independent mechanisms such as thermal effects, instead of observ-

ing an increase of the effective beam waist as in DB14/PMMA, energy storage in molecule is proposed in DR1/PMMA, which delays the temperature diffusion to PMMA. Temperature-dependent birefringence measurements are performed in DR1/PMMA to confirm that thermal agitation of molecular orientation obtained by photoisomerization is the responsible mechanism.

Chapter 5 serves a conclusion, and summarizes our interpretation of the results. Possible applications and experiments for further studies are suggested.

1.5 Summary of the contribution of this work

The goal of our work is to understand complicated mechanisms of the nonlinear optical response in azo dye-doped polymers. The mechanisms that are found to be photoisomerization, photothermal heating, and coupling between them.

The method used in this work is an analysis of the time-dependent refractive index data on two representative samples. To find the time-dependent refractive index, we developed a new TZ-scan technique.[28] TZ-scan is a time sequence of Z-scan at fixed time frames. Combining all sequences leads us to the time-dependent refractive index.

One of common nonlinear optical mechanisms is the thermal lens effect. The thermal refractive index and its nonlinear refractive index are calculated by modifying Akhmanov's theory of self-focusing and thermal diffusion equation which originates from photothermal effect.

Disperse Blue 14 (DB14) doped PMMA is used as a control sample to understand the thermal lens effect related to the theory we developed because it does not have isomers. Comparing the thermal conductivity of PMMA to our results confirms our experiment and theory. When the thermal lens effect of DB14 is applied to DR1, it is found that there is no thermal lens effect in DR1. We propose that the thermal lens effect is delayed due to complicated mechanisms of DR1 molecules such as energy storage in the ground cis state.

Another significant mechanism is photoisomerization. In short times and low intensities, the photoisomerization mechanism is dominant due to the absorption of polarized photons. The ratio of circular to linear polarization of light of the nonlinear refractive index of DR1 as a function of time shows that the dominant mechanism is photoisomerization.

Bibliography

[1] M. G. Kuzyk and C. W. Dirk, *Characterization techniques and tabulations for organic nonlinear optical materials* (Marcel Dekker, 1998).

[2] R. W. Boyd, *Nonlinear Optics* (Academic Press, 1992).

[3] B. E. A. Saleh and M. C. Teich, *Fundamentals of photonics* (Wiley, New York, 1991).

[4] M. G. Kuzyk, "Physical Limits on Electronic Nonlinear Molecular Susceptibilities," Phys. Rev. Lett. **85**, 1218 (2000).

[5] M. G. Kuzyk, "Compact sum-over-states expression without dipolar terms for calculating nonlinear susceptibilities," Phys. Rev. A. **72** (2005).

[6] P. A. Franken, A. E. Hill, C. W. Peters, and G. Weinreich, "Generation of Optical Harmonics," Phys. Rev. Lett. **7**, 118–119 (1961).

[7] J. P. Gordon, R. C. C. Leite, R. S. Moore, S. P. S. Porto, and J. R. Whinnery, "Long-Transient Effects in Lasers with Inserted Liquid Samples," J. Appl. Phys. **36**, 3–8 (1965).

[8] S. A. Akhmanov, A. P. Sukhorukov, and R. V. Khokhlov, "Self-Focusing and Self-Trapping of Intense Light Beams in A Nonlinear Medium," Sov. Phys. JETP **23**, 1025–33 (1966).

[9] S. A. Akhmanov, A. P. Sukhorukov, and R. V. Khokhlov, "Self-Focusing and Diffraction of Light in a Nonlinear Medium," Sov. Phys. Usp. **93**, 609–36 (1968).

[10] J. M. Harris and N. J. Dovichi, "Thermal Lens Calorimetry," Anal. Chem. **52**, 695A–706A (1980).

[11] M. Sheik-Bahae, A. A. Said, T. H. Wei, D. J. Hagan, and E. W. Vanstryland, "Sensitive Measurement of Optical Nonlinearities Using a Single Beam," IEEE J. Quantum Electron. **26**, 760–769 (1990).

[12] J. Castillo, V. P. Kozich, and A. Marcano, "Thermal Lensing Resulting from One-Photon and 2-Photon Absorption Studied with a 2-Color Time-Resolved Z Scan," Opt. Lett. **19**, 171–173 (1994).

[13] Z. X. Zhang, W. Qiu, E. Y. B. Pun, P. S. Chung, and Y. Q. Shen, "Doped polymer films with high nonlinear refractive indices," Electron. Lett. **32**, 129–130 (1996).

[14] T. Catunda, M. L. Baesso, Y. Messaddeq, and M. A. Aegerter, "Time-resolved Z-scan and thermal lens measurements in Er+3 and Nd+3 doped fluoroindate glasses," J. Non-Cryst. Solids **213**, 225–230 (1997).

[15] C. R. Mendonca, M. M. Costa, J. Giacometti, F. D. Nunes, and S. C. Zilio, "Nonlinear refractive indices of polystyrene films doped with azobenzene dye Disperse Red 1," Electron. Lett. **34**, 116–117 (1998).

[16] M. Falconieri, "Thermo-optical effects in Z-scan measurements using high-repetition-rate lasers," J. Opt. A. **1**, 662–667 (1999).

[17] M. Falconieri and G. Salvetti, "Simultaneous measurement of pure-optical and thermo-optical nonlinearities induced by high-repetition-rate, femtosecond laser pulses: application to CS2," Appl. Phys. B **69**, 133–136 (1999).

[18] A. Gnoli, L. Razzari, and M. Righini, "Z-scan measurements using high repetition rate lasers: how to manage thermal effects," Opt. Express **13**, 7976–7981 (2005).

[19] F. L. S. Cuppo, A. M. F. Neto, S. L. Gomez, and P. Palffy-Muhoray, "Thermal-lens model compared with the Sheik-Bahae formalism in interpreting Z-scan experiments on lyotropic liquid crystals," J. Opt. Soc. Am B **19**, 1342–1348 (2002).

[20] J. C. Liang and X. Q. Zhou, "Application of continuous-wave laser Z-scan technique to photoisomerization," J. Opt. Soc. Am B **22**, 2468–2471 (2005).

[21] Z. Sekkat and M. Dumont, "Polarization Effects in Photoisomerization of Azo Dyes in Polymeric Films," Appl. Phys. B **53**, 121–123 (1991).

[22] Z. Sekkat and M. Dumont, "Photoassisted Poling of Azo Dye Doped Polymeric Films at Room Temperature," Appl. Phys. B **54**, 486–489 (1992).

[23] Z. Sekkat, J. Wood, and W. Knoll, "Reorientation Mechanism of Azobenzenes within the Trans ⇒ Cis Photoisomerization," J. Phys. Chem. **99**, 17 226–17 234 (1995).

[24] Z. Sekkat and W. Knoll, "Creation of Second-order Nonlinear Optical Effects by Photoisomerization of Polar Azo Dyes in Polymeric Films: Theoretical Study of Steady-state and Transient Properties," J. Opt. Soc. Am. B. **12**, 1855–67 (1995).

[25] Z. Sekkat and W. Knoll, *Photorefractive Organic Thin Films* (Academic Press, San Diego, 2002).

[26] J. Brandrup and E. H. Immergut, *Polymer Handbook* (Wiley, New York, 1975).

[27] D. C. Chu, M. Touzelbaev, K. E. Goodson, S. Babin, and R. F. Pease, "Thermal conductivity measurements of thin-film resist," J. Vac. Sci. Technol., B **19**, 2874–2877 (2001).

[28] J. J. Park, S. Bian, and M. G. Kuzyk, "Dynamics of intensity dependent refractive index using T-Scan," Proc. SPIE **4798**, 116–122 (2002).

Chapter 2

Theory

2.1 Introduction

The purpose of this chapter is to develop the theory of how a gaussian beam propagates in a nonlinear medium in the parabolic approximation. The intensity dependence of changes in the beam radius depend on time and the nature of the mechanisms that contribute. We treat the case of a non-instantaneous response that includes both a spatial local and nonlocal response that is capable of modeling the behavior of photothermal heating and photo-isomerization.

We use Akhmanov's self-(de)focusing theory[1][2] under the condition that the Rayleigh length is much larger than the sample thickness in which self-(de)focusing is the sole nonlinear optical phenomenon at work. We generalize the nonlinear refractive index by using a gaussian beam-shaped light source and the intensity-dependent transmittance through an aperture that is small compared to the beam waist-a geometry that is used in our experiments.

For nonlocal mechanisms, such as thermal lens effect, we calculate the spatial temperature difference from ambient derived using the thermal diffusion equation with the beam as heat source. As such, the heat source is proportional to the local beam intensity, which is used as the source of the ray inclination in the wave equation to obtain the generalized thermal

nonlinear refractive index distribution, leading to a model of photo-thermal heating.

For the local mechanisms of photo-isomerization, we calculate the nonlinear refractive index for a continuous wave as the light source in low the intensity and short time regime following the method of Sekkat and coworkers.[3]

The contribution of photothermal heating and photo-isomerization are necessarily coupled since the absorbance depends on the degree of molecule alignment. To couple these mechanisms, we combine the photo-thermal heating model with the Einstein relation for rod-like molecules includes the order parameters that we calculate due to the photo-isomerization mechanism.

The individual mechanisms can be separately tested by independent experiments that do not yield coupling. For example, the temperature can be varied independently from the light source, we yielding a measurement of how the temperature agitates the polymer leading to angular molecular redistribution.

Our models are motivated by our observation of an intensity-dependent de-focusing effect of the transmitted beam profile through a dye-doped polymer, which we propose is due to two dominant mechanisms: a nonlocal effect and local effect, such as photo-thermal heating and photo-isomerization.

Our approach is to first assume that those two mechanisms are uncoupled, so that we can derive two separate models. Then, we generalize the theory to a coupled model of these mechanisms by using the Einstein relation and generalized photothermal heating.

In all our calculations, we consider a spatial gaussian light source whose Rayleigh length is much larger than the sample thickness so that we can make the assumption that the beam is collimated in the sample. We assume that an intensity dependent refractive index causes the beam radius of the transmitted beam to change while retaining the gaussian profile. We are particularly interested in the intensity profile at the center of the beam since our experiments use the transmittance through an aperture on the beam axis as a measure of the beam shape. From this measurement, we can calculate how the beam size changes as

long as the shape of the beam remains approximately gaussian.

Specially, our contribution to the calculations are

- Generalization of the nonlinear refractive index as a function of intensity and the normalized transmittance through an aperture in modification of Akhmanov's results of the dimensionless of beam radius f when $R \gg 1$.
- The nonlinear refractive index for thermal lens effect as a function of time extended from the generalization above.
- Analytical relationship between the photothermal effect and the photo-isomerization followed by the molecular reorientation with the modification of Sekkat's model to a short time and low intensity regime via the Einstein relation.

2.2 The nonlinear refractive index

2.2.1 Geometrical optics of a nonlinear medium

In this section, we review self de-focusing based on Akhmanov's theory.[2] In his paper, Akhmanov made the assumption that the beam could be approximated in the geometric limit as follows:

1. Diffraction is smaller than nonlinear refraction so that the wavevector, $k \to \infty$, or the wavelength $\lambda \to 0$.

2. Only terms to second order in the slowly varying amplitude are included in the eikonal. For a slowly varying amplitude, A, the electric field $\vec{E}$ can be expressed as:

$$\vec{E} = \frac{1}{2}\hat{e}A\exp\left[i(\omega t - \vec{k}\cdot\vec{r})\right] + c.c, \tag{2.1}$$

where $\hat{e}$ is the polarization direction, ω the angular frequency, $A = A_0\exp(-iks)$, and s is the eikonal. With the slowly varying amplitude approximation, substituting Equation (2.1)

into Maxwell's wave equation to second-order in the transverse derivative yields

$$2\frac{\partial s}{\partial z} + \left(\frac{\partial s}{\partial r}\right)^2 = \frac{\epsilon_2}{\epsilon_0} A_0^2 \tag{2.2}$$

and

$$\frac{\partial A_0^2}{\partial z} + \frac{\partial s}{\partial r}\frac{\partial A_0^2}{\partial r} + A_0^2\left(\frac{\partial^2 s}{\partial r^2} + \frac{m}{r}\frac{\partial s}{\partial r}\right) = 0, \tag{2.3}$$

where ϵ_2 is the intensity dependent refractive index defined through the dielectric function $\epsilon = \epsilon_0 + \epsilon_2 E^2$. This term originates from a nonlinear term in the polarization in Maxwell's equations. $m = 0$ corresponds to a two dimensional beam and $m = 1$ to a three dimensional beam. It is impossible to obtain an analytical solution to the coupled set of equations given by Equation (2.2) and (2.3).

In a nonlinear medium ($\epsilon_2 \neq 0$), the eikonal and the amplitude can be expressed in the parabolic approximation by,

$$\begin{aligned} s &= \frac{r^2}{2}\beta(z) + \varphi(z) \\ A_0^2 &= \frac{E_0^2}{f^{1+m}(z)}\left[1 - \frac{2r^2}{a^2 f^2(z)}\right], \end{aligned} \tag{2.4}$$

where $\beta^{-1}(z)$ is the radius of curvature, $\varphi(z)$ is the addition to the eikonal due to the intensity dependent refractive index change., $f(z)$ is the dimensionless width of the beam, and E_0^2 is the square of the field amplitude on the beam axis. Figure 2.1 shows a diagram of the beam parameters. At the entrance to the nonlinear medium, we have,

$$\begin{aligned} \beta(0) &= \frac{1}{R} \\ \varphi(0) &= 0 \\ f(0) &= 1 \\ A_0^2(r,0) &= E_0^2\left(1 - \frac{2r^2}{a^2}\right), \end{aligned} \tag{2.5}$$

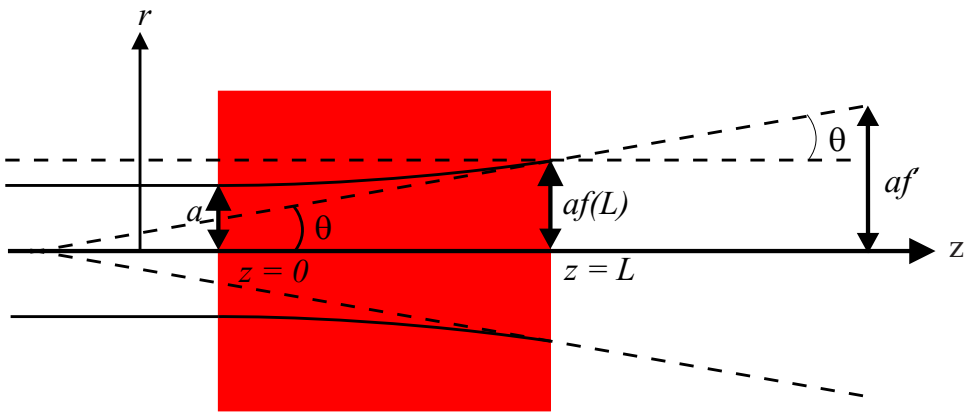

Figure 2.1: Schematic diagram of a beam propagating through the sample as given by the self de-focusing theory. a and $af(L)$ are the radius of the beam at the entrance and the exit of the sample, respectively. r is the radial coordinate and z is the propagating axis. θ is the divergence angle due to the self de-focusing effect. af' is the radius of the beam at the closed aperture which is proportional to $af(L)$ at a given time.

where A_0 is the parabolic approximation of a gaussian beam near its center, i.e. for $r \ll a$. We find the solution of $f^2(z)$ by substituting Equations (2.4) into Equations (2.3) and (2.2) with the boundary condition of Equations (2.5).

For the case of a spherical wave ($m = 1$), the dependence of the beam width on the distance is given by solving Equations (2.2) through (2.5), which yields:

$$f^2(z) = \left(\frac{1}{R^2} - \frac{2\epsilon_2 E_0^2}{\epsilon_0 a^2}\right) z^2 + \frac{2}{R} z + 1. \tag{2.6}$$

Appendix 2.8.1 shows the details of how Equation (2.6) is derived. In the experimental setup, the radius of curvature is large compared to the length of the sample. Therefore, we assume that the $\frac{1}{R}$ terms can be ignored so that Equation (2.6) can be written as,

$$f^2(z) = -\frac{2\epsilon_2 E_0^2}{\epsilon_0 a^2} z^2 + 1. \tag{2.7}$$

2.2.2 Transmittance through an aperture

A change of the beam waist is induced by the nonlinear refractive index by a change of refractive index, which depends on the value of the intensity at a given point according to:

$$\Delta n = n_2 I, \tag{2.8}$$

where n_2 is related to ϵ_2 in Gaussian units by,

$$\frac{n_2}{n_0} I = \frac{1}{2} \frac{\epsilon_2}{\epsilon_0} E^2. \tag{2.9}$$

Note that we will derive this relationship later. We now apply the theory in section 2.2.1 to calculate the change in transmittance through an aperture due to a change in the beam waist induced by an intensity dependent refractive index. We begin by considering the transmitted power passing through an aperture that is small compared to the beam radius, a. When the nonlinear refractive index is zero, the dimensionless width f is unity. Therefore, we do not observe any transmittance change as a function of the intensity.

The intensity distribution of a gaussian beam is given by,

$$I(r) = \frac{2P_0}{\pi a^2} \exp\left(-\frac{2r^2}{a^2 f^2}\right). \tag{2.10}$$

We assume that nonlinear absorption is very small compared to nonlinear refraction, i.e., the real part of nonlinear refractive index is much larger than its imaginary part. In our experiment, power is measure by a photo detector as a voltage. Therefore, the transmitted

power through an aperture with a radius r_d is calculated as,

$$\begin{aligned} P(t) &= \int_0^{r_d} I(r)dA \\ &= \int_0^{r_d} \frac{2P_0}{\pi a^2} \exp\left(-\frac{2r^2}{a^2 f^2}\right) r dr d\phi \\ &= P_0 \left[1 - \exp\left(-\frac{2r_d^2}{a^2 f^2}\right)\right]. \end{aligned} \tag{2.11}$$

The transmitted power normalized to the initial value with $\epsilon_2 = 0$ ($f = 1$) yields the normalized transmittance:

$$\begin{aligned} \mathcal{T} &= \frac{P(t)}{P(0)} = \frac{1 - \exp\left(-\frac{2r_d^2}{a^2 f^2(t)}\right)}{1 - \exp\left(-\frac{2r_d^2}{a^2}\right)} \\ &= \frac{1 - \exp\left[-\frac{2r_d^2}{a^2(1-2\epsilon_2(t)E^2L^2/\epsilon_0 a^2)}\right]}{1 - \exp\left[-\frac{2r_d^2}{a^2}\right]}, \end{aligned} \tag{2.12}$$

where we assume that the nonlinear response is time dependent. As such, the dependence of the transmittance on time is a measure of the time response of the nonlinearity of the material. Note that in reality, the response will be given by a convolution of n_2 and I, as we will discuss later. We convert ϵ_2 to n_2 by using the relationship,

$$\begin{aligned} \vec{D} &= \epsilon \vec{E} \\ &= \left(\epsilon_0 + \epsilon_2 E^2\right) \vec{E} \end{aligned} \tag{2.13}$$

and

$$n = \sqrt{\epsilon} = \sqrt{\epsilon_0} \left(1 + \frac{\epsilon_2}{\epsilon_0} E^2\right)^{1/2}. \tag{2.14}$$

Since the second term in Equation (2.14) is very small compared to unity, we can rewrite Equation (2.14) as

$$n \simeq \sqrt{\epsilon_0} \left(1 + \frac{1}{2}\frac{\epsilon_2}{\epsilon_0} E^2\right). \tag{2.15}$$

By using the relationship $n = n_0 + n_2 I$ and Equation (2.15), we find

$$\frac{1}{2}\frac{\epsilon_2}{\epsilon_0}E^2 = \frac{n_2}{n_0}I. \tag{2.16}$$

Substituting Equation (2.16) into Equation (2.12) yields

$$\mathcal{T} = \frac{1 - \exp\left[-\frac{2r_d^2}{a^2(1-4n_2IL^2/n_0a^2)}\right]}{1 - \exp\left[-\frac{2r_d^2}{a^2}\right]}. \tag{2.17}$$

The argument of the exponential function in the numerator of Equation (2.17) can be approximated by a binomial expansion when the nonlinear phase shift is small:

$$\begin{aligned} Arg &= -\frac{2r_d^2}{a^2}\left[1 - 4\frac{n_2}{n_0}I\left(\frac{L}{a}\right)^2\right]^{-1} \\ &\simeq -\frac{2r_d^2}{a^2}\left[1 + 4\frac{n_2}{n_0}\left(\frac{L}{a}\right)^2 I\right]. \end{aligned} \tag{2.18}$$

By substituting Equation (2.18) into Equation (2.17) and expanding the exponential function, we have the normalized transmittance,

$$\begin{aligned} \mathcal{T} &= \frac{1 - \exp\left[-2\left(\frac{r_d}{a}\right)^2\right]\exp\left[-\frac{8n_2}{n_0}\left(\frac{r_d}{a}\right)^2\left(\frac{L}{a}\right)^2 I\right]}{1 - \exp\left[-2\left(\frac{r_d}{a}\right)^2\right]} \\ &\simeq \frac{1 - \exp\left[-2\left(\frac{r_d}{a}\right)^2\right]\left[1 - \frac{8n_2}{n_0}\left(\frac{r_d}{a}\right)^2\left(\frac{L}{a}\right)^2 I\right]}{1 - \exp\left[-2\left(\frac{r_d}{a}\right)^2\right]}. \end{aligned} \tag{2.19}$$

In experiments, it is straightforward to measure $d\mathcal{T}/dI$. In our small n_2 approximation, $\mathcal{T}$ is a linear function of I, so the theory for the measured intensity dependent transmittance from Equation (2.19) yields

$$\frac{d\mathcal{T}}{dI} = \frac{\frac{8n_2}{n_0}\left(\frac{r_d}{a}\right)^2\left(\frac{L}{a}\right)^2\exp\left[-2\left(\frac{r_d}{a}\right)^2\right]}{1 - \exp\left[-2\left(\frac{r_d}{a}\right)^2\right]}. \tag{2.20}$$

Therefore, given the experimental measure of the slope, dT/dI, we can get n_2 by inverting Equation (2.20),

$$n_2 = \frac{n_0}{8}\left(\frac{a}{r_d}\right)^2\left(\frac{a}{L}\right)^2\frac{1-\exp\left[-2\left(\frac{r_d}{a}\right)^2\right]}{\exp\left[-2\left(\frac{r_d}{a}\right)^2\right]}\frac{d\mathcal{T}}{dI}. \tag{2.21}$$

If the aperture radius r_d is small compared to a, which we can experimentally control, the exponentials can be approximated as

$$\exp\left[-2\left(\frac{r_d}{a}\right)^2\right] \simeq 1 \quad \text{and} \quad 1-\exp\left[-2\left(\frac{r_d}{a}\right)^2\right] \simeq 2\left(\frac{r_d}{a}\right)^2. \tag{2.22}$$

Finally, Substituting Equation (2.22) into (2.21) we get n_2 in the form,

$$\boxed{n_2 = \frac{n_0}{4}\left(\frac{a}{L}\right)^2\frac{d\mathcal{T}}{dI}.} \tag{2.23}$$

2.2.3 Nonlinear absorption

In the previous section, we considered nonlinear refraction. Next, we consider the effects of nonlinear absorption. The transmitted power, $P(t)$, for open aperture case, where the aperture is much larger than the beam waist, is given by

$$P(t) = P_0\exp\left(-\alpha(t)L\right) = P_0\exp\left\{-\left(\alpha_0+\alpha_2(t)I\right)L\right\}, \tag{2.24}$$

where P_0 is the power measured before the sample and $\alpha(t)$ is the loss as a function of time. The normalized transmittance for the open aperture case can be evaluated with the assumption that $\alpha_2(t)$ is very small:

$$\begin{aligned}\mathcal{T}_o &= \frac{P(t)}{P(0)} = \frac{P_0\exp\left(-\alpha(t)L\right)}{P_0\exp\left(-\alpha(0)L\right)} \\ &= \exp\left(-\alpha_2(t)IL\right) \\ &\simeq 1-\alpha_2(t)IL,\end{aligned} \tag{2.25}$$

where we assume $\alpha(0) = \alpha_0$. By taking the derivative with respect to I of Equation (2.25), we get the experimentally determined quantity:

$$\frac{d\mathcal{T}_o}{dI} = -\alpha_2(t)L. \tag{2.26}$$

2.2.4 Nonlinear absorption and refraction

In this section we combine self de-focusing with nonlinear absorption. The goal is to develop a theory that can separate the real and imaginary parts of n_2 from the normalized transmittance which has mixed information.

The intensity profile passed by the sample is given by

$$I(t) = \frac{2P}{\pi a^2 f^2} \exp\left[-\frac{2r^2}{a^2 f^2}\right] \exp\left[-\alpha(t)L\right] \tag{2.27}$$

By using Equation (2.19) and (2.25), the normalized closed aperture transmittance, $\mathcal{T}^t$, with complex n_2 yields

$$\begin{aligned}
\frac{P(t)}{P(0)} &= \mathcal{T}^t = (1-\alpha_2(t)IL)\,\frac{1-\exp\left[-2\left(\frac{r_d}{a}\right)^2\right]\left[1-\frac{8n_2}{n_0}\left(\frac{r_d}{a}\right)^2\left(\frac{L}{a}\right)^2 I\right]}{1-\exp\left[-2\left(\frac{r_d}{a}\right)^2\right]} \\
&= 1-\alpha_2(t)IL+\frac{\frac{8n_2}{n_0}\left(\frac{r_d}{a}\right)^2\left(\frac{L}{a}\right)^2\exp\left(-\frac{2r_d^2}{a^2}\right)}{1-\exp\left(-\frac{2r_d^2}{a^2}\right)}I \\
&\quad -\alpha_2(t)L\frac{\frac{8n_2}{n_0}\left(\frac{r_d}{a}\right)^2\left(\frac{L}{a}\right)^2\exp\left(-\frac{2r_d^2}{a^2}\right)}{1-\exp\left(-\frac{2r_d^2}{a^2}\right)}I^2.
\end{aligned} \tag{2.28}$$

We assume that the nonlinear absorption coefficient has no significant effect on the path of rays near the beam axis. This assumption is satisfied when the aperture size is small

compared to the size of the beam. From Equation (2.28), the slope $\frac{d\mathcal{T}^t}{dI}$ is

$$\begin{aligned}\frac{d\mathcal{T}^t}{dI} &= -\alpha_2(t)L + \frac{\frac{8n_2}{n_0}\left(\frac{r_d}{a}\right)^2\left(\frac{L}{a}\right)^2\exp\left[-2\left(\frac{r_d}{a}\right)^2\right]}{1-\exp\left[-2\left(\frac{r_d}{a}\right)^2\right]} \\ &- \frac{16\alpha_2(t)L\frac{n_2}{n_0}\left(\frac{r_d}{a}\right)^2\left(\frac{L}{a}\right)^2\exp\left[-2\left(\frac{r_d}{a}\right)^2\right]}{1-\exp\left[-2\left(\frac{r_d}{a}\right)^2\right]}I. \end{aligned} \tag{2.29}$$

When only the center of the beam is considered so that $r_d \ll a$, we can expand Equation (2.29) to first order in the nonlinearity,

$$\begin{aligned}\frac{d\mathcal{T}^t}{dI} &\simeq -\alpha_2(t)L + \frac{4n_2}{n_0}\left(\frac{L}{a}\right)^2 \\ &= \frac{d\mathcal{T}_o}{dI} + \frac{d\mathcal{T}}{dI}. \end{aligned} \tag{2.30}$$

The first term on the RHS is the slope for the open aperture case as given by Equation (2.26) and is related solely to nonlinear absorption. Therefore, the real part of n_2 can be obtained by subtracting the slope derived from the open aperture experiment from the closed aperture data.

2.3 Nonlocal nonlinear optical effect

The previous calculation was a local one since it assumed that the refractive index change at a point in the material depends on the intensity at that point only. There are many mechanisms in which the refractive index is a function of the intensity at other points. These are called non-local mechanisms, of which photo-thermal heating is one example. In this section, we model the photo-thermal mechanism.

2.3.1 Thermal diffusion

In the thermal mechanism, we assume that the temperature gradient response time of the sample is very slow compared to the light transit time through the sample. Therefore, the beam acts as the heat source with cylindrical symmetry and instantaneously follows the beam's intensity profile through the sample. We should also consider the boundary condition at the surfaces of the sample due to its contact with the environment. We assume that the ambient temperature outside the surfaces changes simultaneously as inside the surface of the sample to simplify the heat transfer equation. Also, we assume that the beam waist is small compared with the length of the sample so that the sample can be considered infinite. Along the propagation direction, we assume that the temperature gradient is too small to cause the beam's shape to change appreciably compared to the effect in the radial direction. We assume that there are no aberrations so that the beam shape remains the same, with only a change in its width and amplitude,[4] and the amount of heat generation per unit length along the propagation direction, per unit time at a point inside the material is instantaneous and proportional to the beam intensity at that point. We introduce the dimensionless beam width, f, so that the heat source term changes width within the sample as the beam width changes, i.e.,

$$\begin{aligned} Q(r,z) &= \frac{2P}{\pi a^2 f^2}\exp\left(-\frac{2r^2}{a^2 f^2}\right)\alpha\exp\left(-\alpha z\right) \\ &= I_p \exp\left(-\frac{2r^2}{a^2 f^2}\right)\frac{\alpha\exp(-\alpha z)}{f^2}, \end{aligned} \tag{2.31}$$

where α is an absorption coefficient and I_p is a peak intensity at the entrance to the medium. The heat transfer equation is given by

$$c\rho\frac{\partial}{\partial t}\Delta T(r,t) - \kappa\nabla^2(\Delta T(r,t)) = Q(r,z), \tag{2.32}$$

where c, ρ, κ, and ΔT are specific heat, density, thermal conductivity, and temperature difference from ambient in the sample, respectively. The solution to Equation (2.32) yields the temperature, $\Delta T(r, z, t)$,which can be found by using

$$\Delta T(r, z, t) = \int_0^\infty \int_0^t Q(r')G(r, r', t')2\pi r' dr' dt', \tag{2.33}$$

where $G(r, r', t)$ is the Green's function. The Green's function in cylindrical coordinates for the heat equation is given by[5]

$$G(r, r', t') = \frac{1}{4\pi\kappa t'} \exp\left(-\frac{r^2 + r'^2}{4Dt'}\right) I_0\left(\frac{rr'}{2Dt'}\right), \tag{2.34}$$

where D is diffusivity given by $\kappa/\rho c$ and I_0 is the modified Bessel function. By substituting Equation (2.34) and (3.25) into Equation (2.33), we have

$$\begin{aligned} \Delta T(r, z, t) &= \int_0^t \int_0^\infty \frac{I_p \alpha}{2f^2} \frac{\exp(-\alpha z)}{\kappa t'} \exp\left(-\frac{r^2 + r'^2}{4Dt'}\right) \exp\left(-\frac{2r'^2}{a^2 f^2}\right) \\ &\quad \times I_0\left(\frac{rr'}{2Dt'}\right) r' dr' dt'. \end{aligned} \tag{2.35}$$

By using the integral formula given by Equation (B-1), we can evaluate the r integral in Equation (2.35) as follows (see appendix 2.8.2),

$$\begin{aligned} \Delta T(r, z) &= \int_0^\infty \exp\left(-\frac{2r'^2}{a^2 f^2}\right) \exp\left(-\frac{r'^2}{4Dt'}\right) I_0\left(\frac{rr'}{2Dt'}\right) r' dr' \\ &= \frac{2Dt'}{1 + 8Dt'/a^2 f^2} \exp\left[\frac{r^2}{4Dt'\left(1 + 8Dt'/a^2 f^2\right)}\right]. \end{aligned} \tag{2.36}$$

By substituting Equation (2.36) into Equation (2.35) and by using Equation (B-4) through (B-7), the integration over time yields

$$\begin{aligned}\Delta T(r,z,t) &= \frac{I_p\alpha\exp(-\alpha z)}{a^2f^2\rho c}\int_0^t dt'\frac{1}{1+\frac{8D}{a^2f^2}t'}\exp\left[-\frac{2r^2}{a^2f^2\left(1+\frac{8Dt'}{a^2f^2}\right)}\right] \\ &= \frac{I_p\alpha\exp(-\alpha z)}{8\kappa}\left[Ei\left(-\frac{2r^2}{a^2f^2}\right)-Ei\left(-\frac{2r^2}{a^2f^2\left(1+\frac{8Dt}{a^2f^2}\right)}\right)\right], \quad (2.37)\end{aligned}$$

where Ei is an exponential integral function given by Equation (B-7). Figure 2.2 shows a plot of the temperature distribution as a function of the position in the sample for typical experimental parameters used in Equation (3.26).

2.3.2 Time-dependent thermal lens effect

In this section, we generalize Akhmanov's derivation of beam propagation in the parabolic approximation to get the time dependence of thermal lensing. We begin with the ray inclination to the beam axis determined from the eikonal Equation (2.4),[4]

$$u = \frac{\partial s}{\partial r} = r\beta(z) = \frac{r}{f}\frac{df}{dz}. \quad (2.38)$$

Using the wave equation and the relationship $\delta n = \frac{\partial n}{\partial T}\delta T$, analogous to the case we developed for $\delta n = n_2 I$, we have

$$\frac{\partial u}{\partial z} + u\frac{\partial u}{\partial r} = -\frac{1}{n_0}\frac{\partial n}{\partial T}\frac{\partial \Delta T}{\partial r}, \quad (2.39)$$

where the thermal lens effect is explicitly shown with a negative sign on the right hand side. Taking the derivative of Equation (3.26) yields

$$\frac{\partial \Delta T}{\partial r} = \frac{I_p a^2\alpha\exp(-\alpha z)}{4\kappa}\left[\frac{\exp\left(-\frac{2r^2}{a^2f^2}\right)-\exp\left(-\frac{2r^2}{a^2f^2+8Dt}\right)}{r}\right]. \quad (2.40)$$

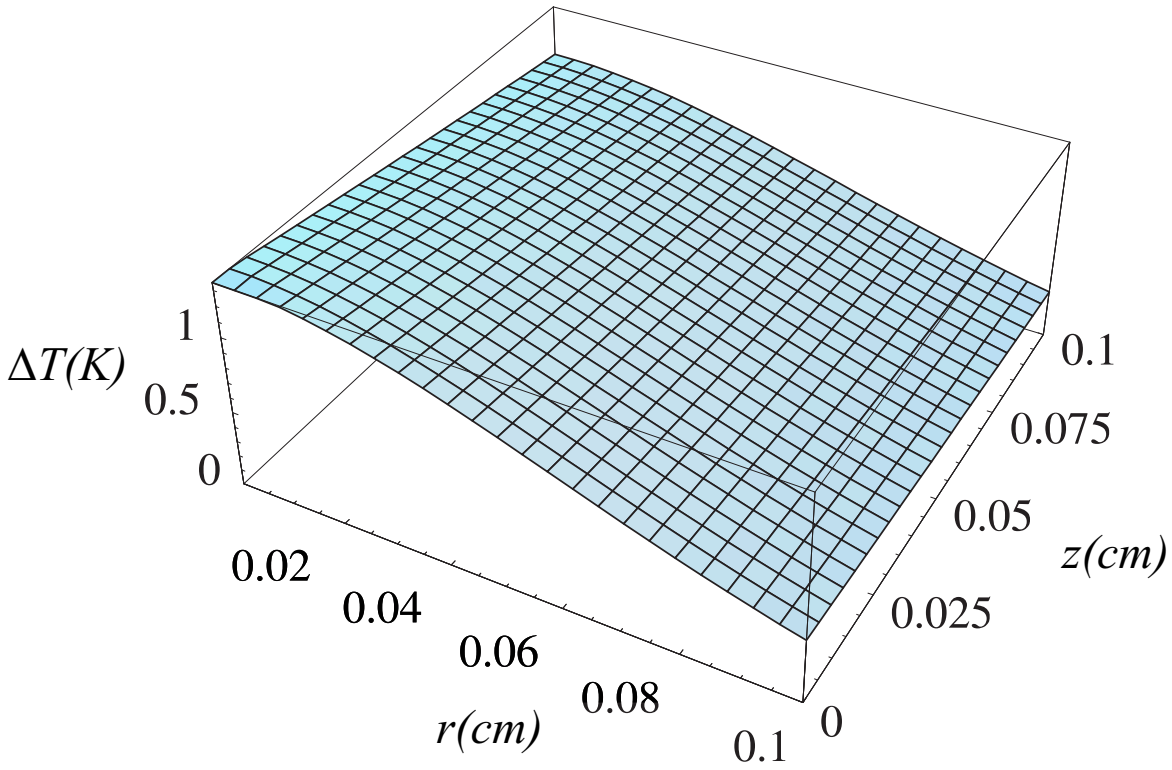

Figure 2.2: Temperature gradient in space with a pump intensity of $600mW/cm^2$, absorption coefficient $\alpha = 3cm^{-1}$, thermal conductivity $\kappa = 0.193W/m \cdot K$, beam radius $a = 0.09cm$, density $\rho = 1.19 \times 10^3 kg/m^3$, specific heat $c = 1.42 \times 10^3 J/kg \cdot K$, and thermal refractive index change coefficient $\frac{\partial n}{\partial T} = 1.5 \times 10^{-4}$. ΔT is the difference in temperature from ambient according to Equation (3.26), r is the radial coordinate, and z is the beam propagation direction in the sample at time $t = \tau = 1.77s$.

After substituting Equation (2.38) and (2.40) into Equation (2.39), we get (see Equation (B-8))

$$\frac{d^2f}{dz^2} = \frac{I_p a^2 \alpha \exp\left(-\alpha z\right)}{4\kappa} \left(\frac{f}{r}\right) \left(-\frac{1}{n_0}\frac{\partial n}{\partial T}\right) \left[\frac{\exp\left(-\frac{2r^2}{a^2 f^2}\right) - \exp\left(-\frac{2r^2}{a^2 f^2\left(1+\frac{8Dt}{a^2 f^2}\right)}\right)}{r}\right]. \quad (2.41)$$

We are interested only in the region close to the beam axis where $r \ll a$. In the on-axis condition, we can make a parabolic approximation, which leads us to (see Equation (B-9))

$$\frac{d^2f}{dz^2} \simeq \frac{I_p \alpha \exp(-\alpha z)}{2n_0 \kappa f}\frac{\partial n}{\partial T}\left[1 + f^2\left(\tau/2t\right)\right]^{-1}, \quad (2.42)$$

where $\tau = a^2/4D$. We assume that the length of the sample is short enough that the beam width does not change appreciable from one end to the other, which allows us to make the approximation that $f \simeq 1$. We can rewrite Equation (2.42) as

$$\frac{d^2f}{dz^2} \simeq \frac{I_p \alpha \exp(-\alpha z)}{2n_0 \kappa}\frac{\partial n}{\partial T}\frac{1}{1+\tau/2t}. \quad (2.43)$$

By solving Equation (2.43) with the boundary condition given by Equation (2.5), we get

$$f(z) = \frac{I_p}{2n_0 \alpha \kappa}\frac{\partial n}{\partial T}\frac{\exp(-\alpha z) + \alpha z - 1}{1+\tau/2t} + 1. \quad (2.44)$$

We assume that the amount of absorption is small enough to expand $\exp(-\alpha z)$ up to the third term. With $B = \frac{I_p}{2n_0\kappa\alpha(1+2\tau/t)}\frac{\partial n}{\partial T}$, the dimensionless beam width, $f^2(z)$, is approximated

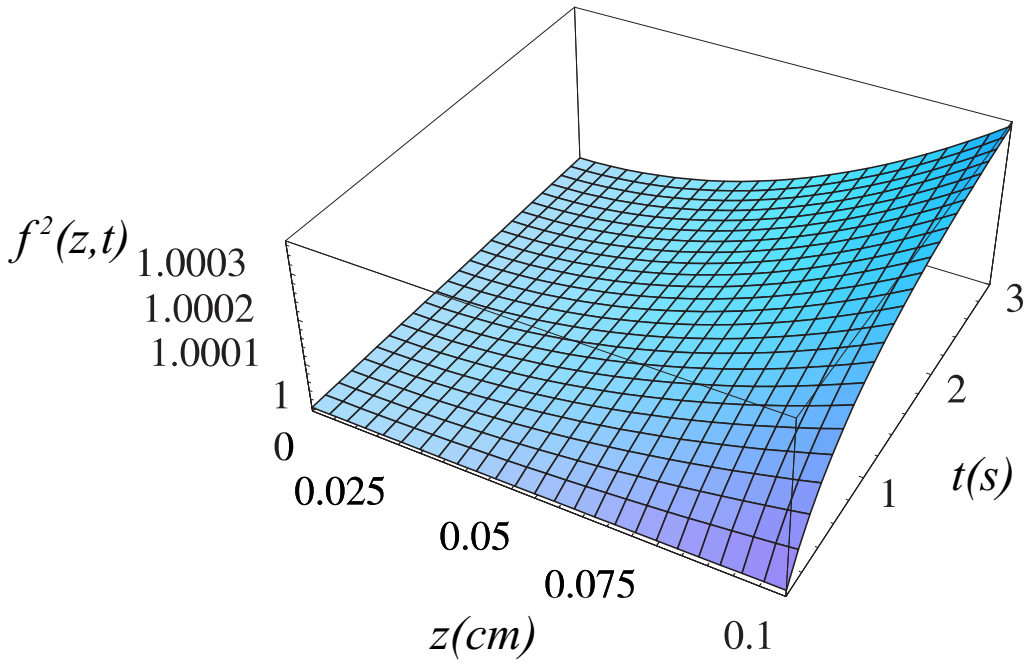

Figure 2.3: Equation (2.45) with a pump intensity of $600mW/cm^2$, absorption coefficient $\alpha = 3cm^{-1}$, thermal conductivity $\kappa = 0.193W/m \cdot K$, beam radius $a = 900\mu m$, density $\rho = 1.19 \times 10^3 kg/m^3$, specific heat $c = 1.42 \times 10^3 J/kg \cdot K$, and thermal refractive index change coefficient $\frac{\partial n}{\partial T} = 1.5 \times 10^{-4}$. z is in the beam propagation direction and t is the time.

as

$$\begin{aligned} f^2(z) &= B^2\left(\exp(-\alpha z)+\alpha z-1\right)^2+2B\left(\exp(-\alpha z)+\alpha z-1\right)+1 \\ &\simeq \frac{B^2}{4}\alpha^4 z^4+B\alpha^2 z^2+1 \\ &\simeq B\alpha^2 z^2+1 \\ &= \frac{\alpha I_p}{2n_0\kappa\left(1+2\tau/t\right)}\frac{\partial n}{\partial T}z^2+1. \end{aligned} \tag{2.45}$$

Figure 2.3 shows a plot of f^2 as a function of time after the beam is turned on and propagation distance in the sample, z, with typical value of experimental parameters substituted into Equation (2.45). As we have discussed in Section 2.2.2, the normalized transmittance is given by (see (B-10))

$$\begin{aligned} \mathcal{T} &= \frac{1-\exp\left(-\frac{2r_d^2}{a^2 f^2(L)}\right)}{1-\exp\left(-\frac{2r_d^2}{a^2}\right)} \\ &\simeq 1-\frac{\alpha L^2}{2n_0\kappa\left(1+\tau/2t\right)}\frac{\partial n}{\partial T}I_p. \end{aligned} \tag{2.46}$$

The slope of transmittance with respect to the intensity is

$$\begin{aligned} \frac{d\mathcal{T}}{dI} &= -\frac{r_d^2}{a^2}\frac{\exp\left(-\frac{2r_d^2}{a^2}\right)\alpha L^2}{1-\exp\left(-\frac{2r_d^2}{a^2}\right)}\frac{dn/dT}{n_0\kappa\left(1+\tau/2t\right)} \\ &\simeq -\frac{\alpha L^2}{2n_0\kappa\left(1+\tau/2t\right)}\frac{\partial n}{\partial T}. \end{aligned} \tag{2.47}$$

By substituting Equation (2.47) into Equation (2.23), we get the nonlinear refractive index from the thermal response mechanism.

$$\boxed{n_2(t)=-\frac{\alpha a^2}{8\kappa\left(1+\tau/2t\right)}\frac{\partial n}{\partial T}.} \tag{2.48}$$

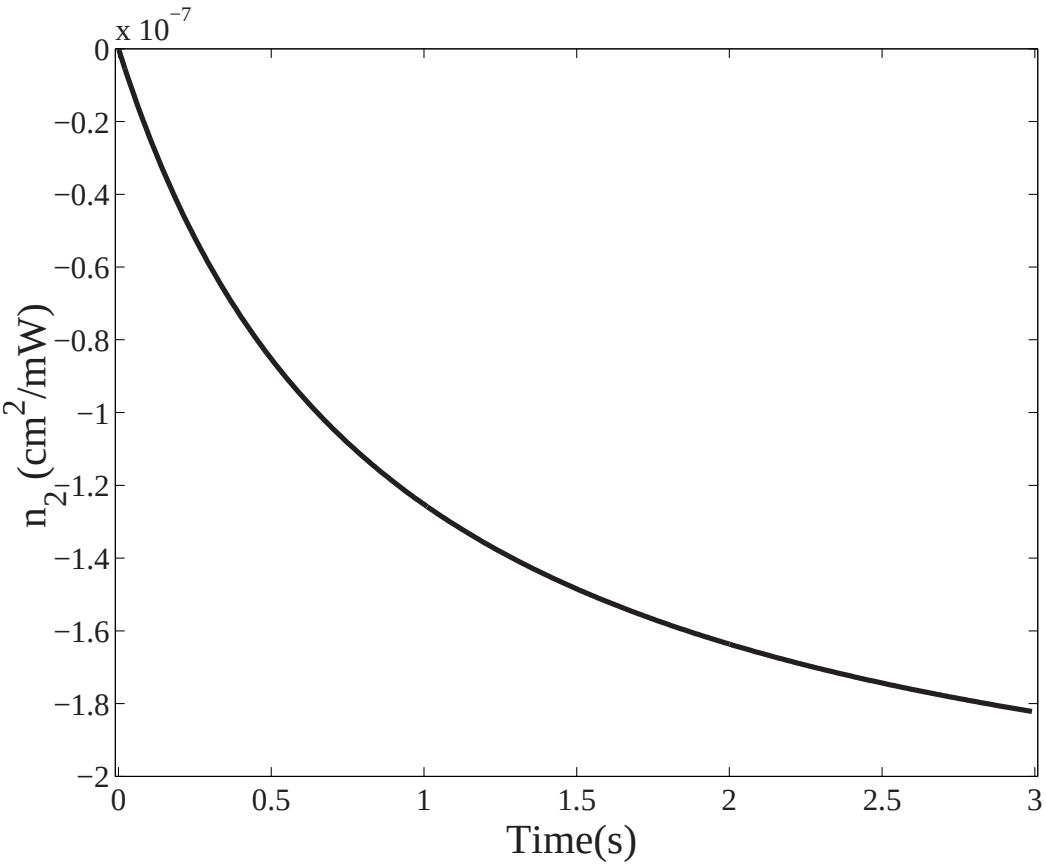

Figure 2.4: n_2 from Equation (2.48) as a function of time with a pump intensity of $600mW/cm^2$, absorption coefficient $\alpha = 3cm^{-1}$, thermal conductivity $\kappa = 0.193W/m \cdot K$, beam radius $a = 0.09cm$, density $\rho = 1.19 \times 10^3 kg/m^3$, specific heat $c = 1.42 \times 10^3 J/kg \cdot K$, and thermal refractive index coefficient $\frac{\partial n}{\partial T} = 1.5 \times 10^{-4}$.

We note that our generalizations to the theory are required for the results to be properly interpreted as we discuss later. Figure 2.4 shows Equation (2.48) plotted as a function of time after a beam is turned on for typical experimental parameters.

2.4 Mechanisms of local nonlinear optical effects

2.4.1 Photo-isomerization

It is known that the azo bond, a double bond between the nitrogen atoms, has low excitation energy for nuclear conformational changes compared to other covalent double bonds. Figure 2.5 shows a typical azo molecule that has two isomers, trans and cis. The ellipse drawn shows how the molecules can be approximated as a cigar shape of distinct aspect ratio. As depicted in Figure 2.6, each isomer has an anisotropic absorption cross section. Figure 2.7 shows the energy diagram of photo-isomerization and thermal relaxation mechanisms. We consider a molecule whose principle axis is aligned along the Euler angle axis represented by $\vec{\Omega}$ as we see from Figure 2.8 and the direction of linear polarization of the incident beam of light is in the 3-direction.

We assume that the rate of conversion of the number density of each isomer per unit time in the direction $\vec{\Omega}$ for photo-isomerization is proportional to the number density of molecules, the number of absorbed photons per unit area per unit time associated with the quantum yield, ϕ, and the cross section, σ, for a uniaxial system, which is given by $\sigma_\perp \sin^2\theta + \sigma_\parallel \cos^2\theta$, where $\sigma_\parallel$ and $\sigma_\perp$ are the cross section for the long axis and perpendicular to the long axis, respectively.

The change of number density of molecules per unit time is given by

$$\begin{aligned}\frac{dn_t(\vec{\Omega})}{dt} &= -I\phi_{tc}\left[\sigma_\perp^t + \left(\sigma_\parallel^t - \sigma_\perp^t\right)\cos^2\theta\right] n_t\left(\vec{\Omega}\right) \\ &\quad + I\phi_{ct}\iint n_c\left(\vec{\Omega}'\right)\left[\sigma_\perp^c + \left(\sigma_\parallel^c - \sigma_\perp^c\right)\cos^2\theta'\right] \\ &\quad \times P^{ct}\left(\vec{\Omega}' \to \vec{\Omega}\right) d\Omega' \\ &\quad + \frac{1}{\tau_c}\iint Q\left(\vec{\Omega}' \to \vec{\Omega}\right) n_c\left(\vec{\Omega}'\right) d\Omega' + D_t \mathbf{R}\cdot\mathbf{R} n_t\left(\vec{\Omega}, t\right) \end{aligned} \tag{2.49}$$

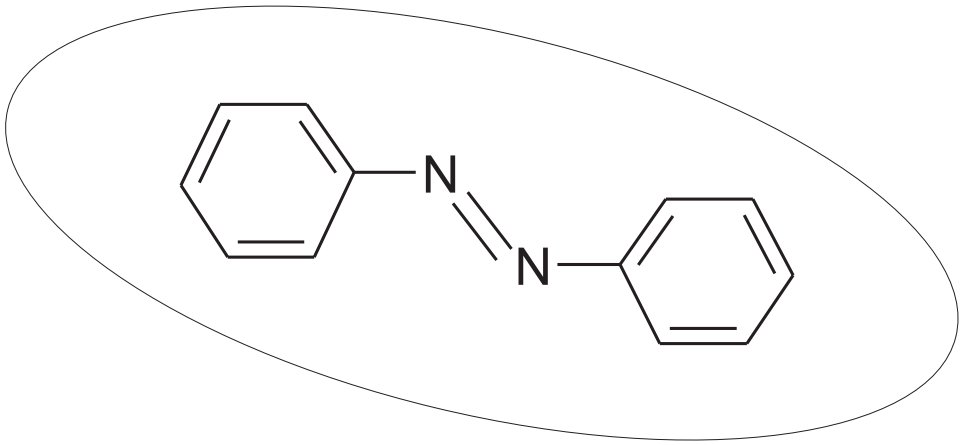

(a) Trans-isomer

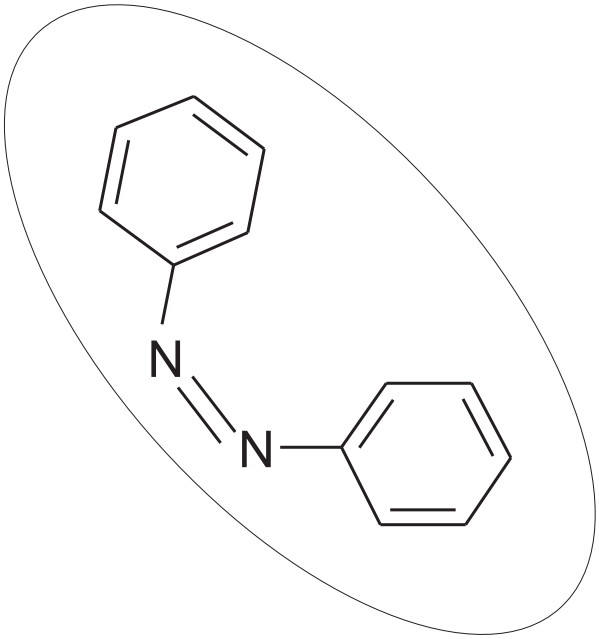

(b) Cis-isomer

Figure 2.5: Schematic diagram of isomers of Disperse Red 1 azo dye.

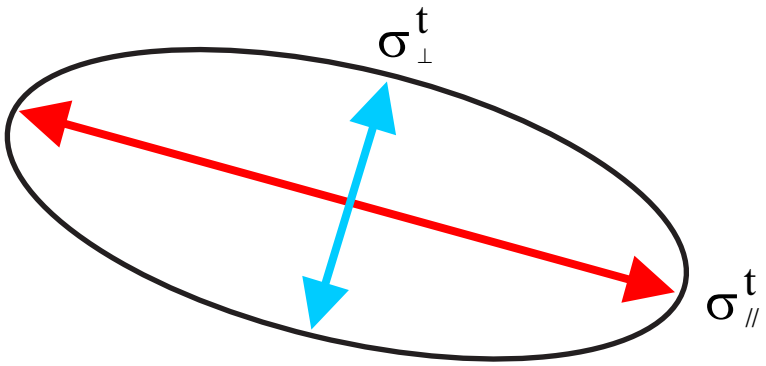

(a) Trans-isomer

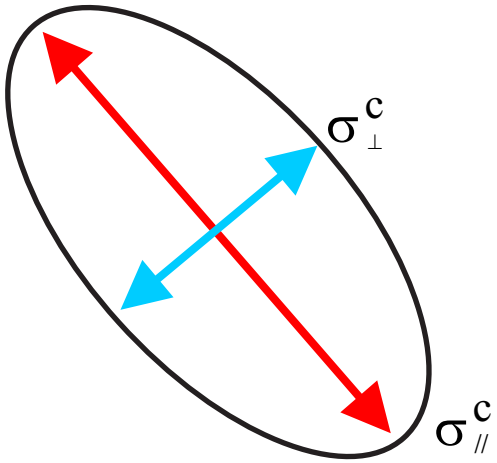

(b) Cis-isomer

Figure 2.6: The DR1 isomers are idealized as cigar-shaped molecules. The anisotropic absorption cross section causes birefringence and dichroism. $\sigma_{\parallel}^{t,c}$ and $\sigma_{\perp}^{t,c}$ are the absorption cross sections for the long axis and short axis of trans(t) and cis(c) molecules, respectively.

and similarly for the cis population

$$\begin{aligned}\frac{dn_c(\vec{\Omega})}{dt} &= -I\phi_{ct}\left[\sigma_{\perp}^{c}+\left(\sigma_{\parallel}^{c}-\sigma_{\perp}^{c}\right)\cos^2\theta\right]n_c\left(\vec{\Omega}\right)\\ &\quad +I\phi_{tc}\iint n_t\left(\vec{\Omega}'\right)\left[\sigma_{\perp}^{t}+\left(\sigma_{\parallel}^{t}-\sigma_{\perp}^{t}\right)\cos^2\theta'\right]\\ &\quad \times P^{tc}\left(\vec{\Omega}'\rightarrow\vec{\Omega}\right)d\Omega'\\ &\quad -\frac{1}{\tau_c}n_c\left(\vec{\Omega}\right)+D_c\mathbf{R}\cdot\mathbf{R}n_c\left(\vec{\Omega},t\right). \end{aligned} \tag{2.50}$$

The first terms in each of Equations (2.49) and (2.50) show the depletion rate of cis and trans molecules around the angle $\vec{\Omega}$ due to angular hole burning by the pump polarization. The second terms are the rate of angular redistribution of cis and trans molecules from other angles ($\vec{\Omega}'$) to fill the angular holes. We define the probability of the redistribution process of cis to trans transition by $P^{ct}\left(\vec{\Omega}'\rightarrow\vec{\Omega}\right)$, and $P^{tc}\left(\vec{\Omega}'\rightarrow\vec{\Omega}\right)$ for trans to cis. In the third term, $Q\left(\vec{\Omega}'\rightarrow\vec{\Omega}\right)$ is the probability of redistribution due to thermal relaxation of cis to trans molecule which has a $3\frac{1}{2}$ hour life time.[6] The last term is from the angular Brownian motion due to temperature agitation. $D_{c,t}$ are the angular diffusion constants in units of s^{-1} for the cis and trans isomer, respectively,[7] and $\mathbf{R}$ is the the rotational operator defined in Equation (C-13). (See appendix 2.8.3).

Using the Legendre polynomials and the boundary condition, Equation (2.49) and (2.50) become (see appendix 2.8.3):

$$\frac{dT_n}{dt}=-I_t\{T\}+I_cP_n^{ct}\{C\}+\gamma Q_nC_n-T_nn\left(n+1\right)D_t \tag{2.51}$$

and

$$\frac{dC_n}{dt}=-I_c\{C\}+I_tP_n^{tc}\{T\}-\gamma C_n-C_nn\left(n+1\right)D_c, \tag{2.52}$$

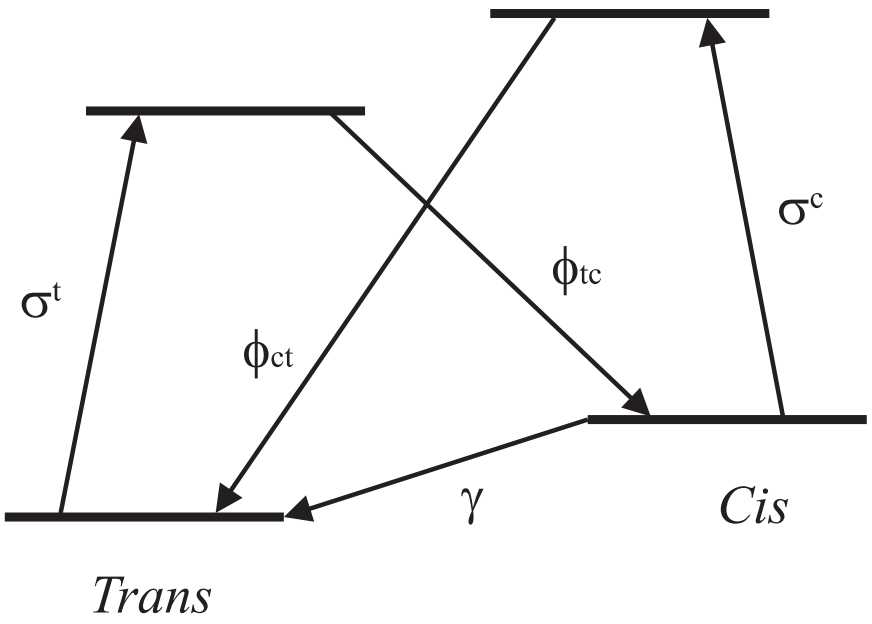

Figure 2.7: Energy diagram of photo-isomerization and cis to trans thermal relaxation mechanisms. σ^t and σ^c are the absorption cross sections of trans and cis molecule to their first excited state per one photon absorbed, respectively. ϕ_{tc} and ϕ_{ct} are non-radiative quantum yields for trans to cis and cis to trans isomerizations, respectively. γ is the rate of thermal relaxation from cis to trans molecule.

where T_n and C_n are the expansion coefficients given by Equation (C-2) and (C-3), and

$$\begin{aligned}
\{T\} &= 3er^t\kappa_{n+}T_{n+2} + \left[1 + er^t\left(3\kappa_n - 1\right)\right]T_n \\
&\quad +3er^t\kappa_{n-}T_{n-2}, \\
\{C\} &= 3er^c\kappa_{n+}C_{n+2} + \left[1 + er^c\left(3\kappa_n - 1\right)\right]C_n \\
&\quad +3er^c\kappa_{n-}C_{n-2}, \\
\kappa_{n+} &= \frac{(n+1)(n+2)}{(2n+1)(2n+3)},\ \kappa_n = \frac{(2n^2+2n-1)}{(2n-1)(2n+3)}, \\
&\text{and} \\
\kappa_{n-} &= \frac{n(n-1)}{(2n-1)(2n+1)}.
\end{aligned} \tag{2.53}$$

For the case of a linear polarized pump beam along the 3 axis, $e = 1$ because the probability of the angular hole burning is proportional to $\cos^2\theta$. For other cases, such as for a circularly

polarized pump beam on the plain containing axis 1 and 2, or an unpolarized beam, $e = -1/2$ because the probability is proportional to $(\sin^2\theta)/2$ instead of $\cos^2\theta$.

We assume that molecules are randomly distributed in angle. In a short time after the pump is turned on, we can assume that the process of trans to cis conversion leading to angular redistribution is dominant compared to that of cis to trans ($P_n^{ct} \to 0$). We can also assume that the thermal conversion from cis to trans is also ignorable because thermal relaxation is a slow process compared to angular hole burning and redistribution by photo-isomerization ($\gamma \to 0$ or $1/\tau_c \to 0$).[6] Thus, we rewrite Equation (2.51) and (2.52) as:

$$\frac{dT_n}{dt} = -I_t\{T\} - T_n n\,(n+1)\,D_t \tag{2.54}$$

and

$$\frac{dC_n}{dt} = -I_c\{C\} + I_t P_n^{tc}\{T\} - C_n n\,(n+1)\,D_c. \tag{2.55}$$

We assume that the higher order terms do not appreciably affect conversion between isomers at low intensity so we keep up to only the second-order parameters. By substituting $n = 0$ in Equation (2.54), we get

$$\frac{dT_0}{dt} = -I_t\left[2er^t T_2 + T_0\right]. \tag{2.56}$$

And when n=2, we get

$$\frac{dT_2}{dt} = -I_t\left[(1 + \frac{4}{7}er^t)T_2 + \frac{2}{5}er^t T_0\right] - 6D_t T_2. \tag{2.57}$$

By solving for T_2 in Equation (2.56) and substituting T_2 into Equation (2.57), we get

$$\frac{d^2T_0}{dt^2} + \left[2I_t\left(1 + \frac{2}{7}er^t\right) + 6D_t\right]\frac{dT_0}{dt} + \left[I_t^2\left(1 + \frac{4}{5}(er^t)^2 + \frac{4}{7}er^t\right) + 6D_t I_t\right]T_0 = 0. \tag{2.58}$$

We assume that $\frac{d^2T_0}{dt^2}$ is negligibly small so that T_0 varies roughly monotonically in time. By

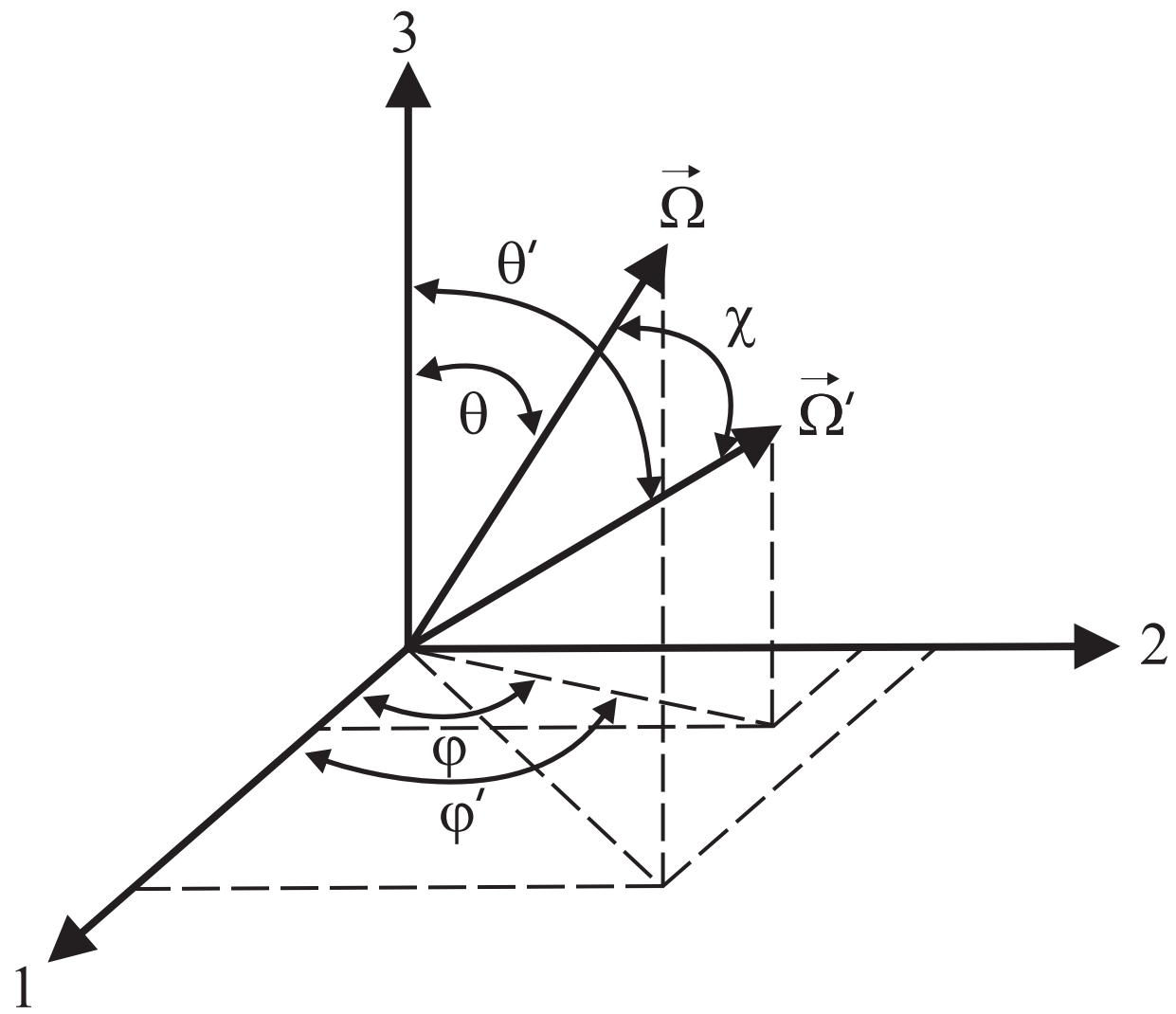

Figure 2.8: Coordinate systems of the molecules in two principle directions, $\vec{\Omega}$ and $\vec{\Omega}'$. The polarization direction of the pumping beam is along axis 3. For the molecules in direction Ω, the angular hole burning probability is proportional to $\sigma_{\parallel}\cos^2\theta + \sigma_{\perp}\sin^2\theta$. χ is the angle between $\vec{\Omega}$ and $\vec{\Omega}'$.

using the initial condition that at $t = 0, T_0 = 1$ in Equation (2.58), we get

$$T_0(t) = \exp\left[-\frac{I_t\left(1+\frac{4}{5}\left(er^t\right)^2+\frac{4}{7}er^t+6\frac{D_t}{I_t}\right)}{2\left(1+\frac{2}{7}er^t+3\frac{D_t}{I_t}\right)}t\right], \tag{2.59}$$

where we have normalized the number density to unity. Since the total number of molecules is conserved, C_0 is given by:

$$\begin{aligned} C_0(t) &= 1 - T_0 \\ &= 1 - \exp\left[-\frac{I_t\left(1+\frac{4}{5}\left(er^t\right)^2+\frac{4}{7}er^t+6\frac{D_t}{I_t}\right)}{2\left(1+\frac{2}{7}er^t+3\frac{D_t}{I_t}\right)}t\right]. \end{aligned} \tag{2.60}$$

Equation (2.59) and (2.60) become

$$T_0(t) = \exp\left(-\lambda_0 t\right) \tag{2.61}$$

and

$$C_0(t) = 1 - \exp\left(-\lambda_0 t\right), \tag{2.62}$$

with the definition of that $\lambda_0 = \frac{I_t\left(1+\frac{4}{5}(er^t)^2+\frac{4}{7}er^t+6\frac{D_t}{I_t}\right)}{2\left(1+\frac{2}{7}er^t+3\frac{D_t}{I_t}\right)}$. By substituting Equation (2.61) into Equation (2.57) and by using the initial condition that when $t = 0, T_2 = 0$, we can solve for $T_2(t)$:

$$T_2(t) = \frac{a_t}{\lambda_t - \lambda_0}\left(\exp(-\lambda_t t) - \exp(-\lambda_0 t)\right), \tag{2.63}$$

where $\lambda_t = I_t(1 + \frac{4}{7}er^t + 6\frac{D_t}{I_t})$ and $a_t = \frac{2}{5}I_t er^t$.

When $n = 2$, Equation (2.55) becomes

$$\frac{dC_2}{dt} = -I_c\left[\left(1+\frac{4}{7}er^c\right)C_2+\frac{2}{5}er^c C_0\right] + I_t P_2^{tc}\left[\left(1+\frac{4}{7}er^t\right)T_2+\frac{2}{5}er^t T_0\right] - 6D_c C_2. \tag{2.64}$$

By substituting Equation(2.61), (2.62), and (2.63) into Equation (2.64) and by using the

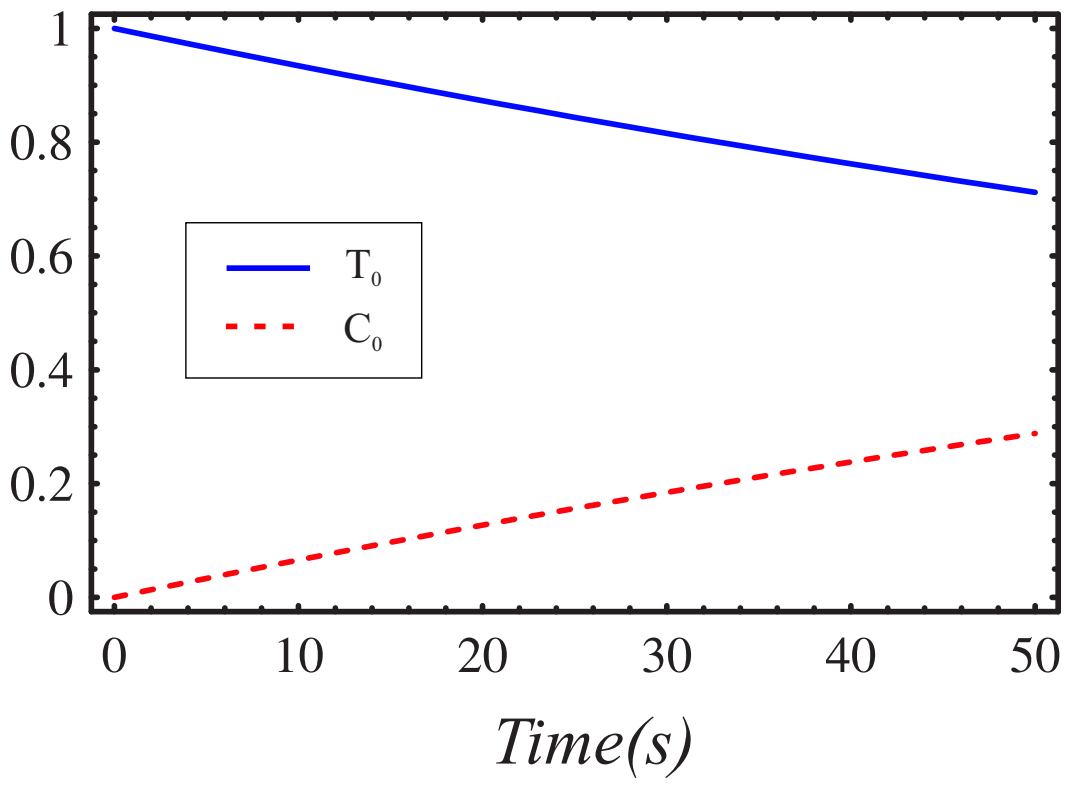

Figure 2.9: The order parameters T_0, C_0 in blue solid and red dashed line, respectively when $D_t = 0.0001$ (low temperature) as a function of time. D_t is proportional to the temperature difference in the sample compared to the ambient temperature. $I_t = 0.011$ and $I_c = 0.00946$.

initial condition that when $t = 0, C_2 = 0$, we can solve for $C_2(t)$:

$$\begin{aligned} C_2(t) &= \frac{a_c(\lambda_t - \lambda_0) - a_t P_2^{tc}(\lambda_0 - 6D_t)}{(\lambda_t - \lambda_0)(\lambda_c - \lambda_0)} \left[\exp(-\lambda_0 t) - \exp(-\lambda_c t)\right] \\ &\quad - \frac{a_t P_2^{tc}(\lambda_t - 6D_t)}{(\lambda_t - \lambda_0)(\lambda_c - \lambda_0)} \left[\exp(-\lambda_t t) - \exp(-\lambda_c t)\right], \end{aligned} \tag{2.65}$$

where $a_c = \frac{2}{5} I_c e r^c$ and $\lambda_c = I_c \left(1 + \frac{4}{7} e r^c + 6\frac{D_c}{I_t}\right)$. Figure 2.9 and 2.10 show the order parameters in the low temperature limit with the physical dimensions we have estimated for DR1. (see Appendix 2.8.3).

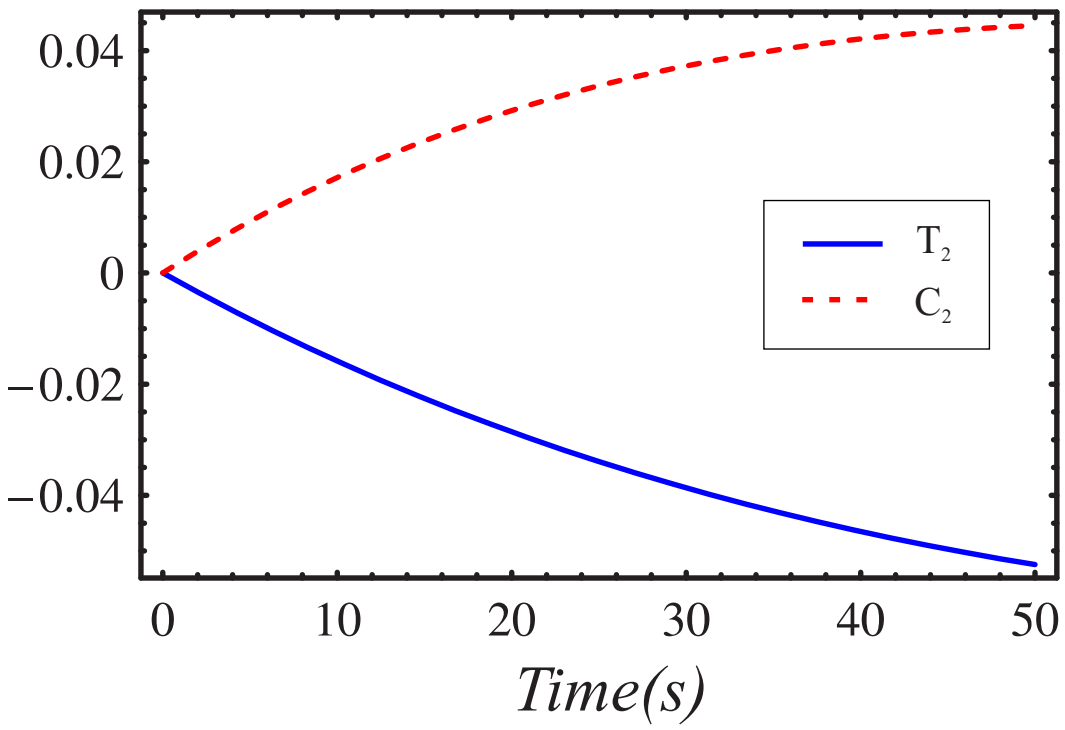

Figure 2.10: The order parameters T_2, C_2 in blue solid and red dashed line, respectively when $D_t = 0.0001$ (low temperatue) as a function of time. $I_t = 0.011$ and $I_c = 0.00946$.

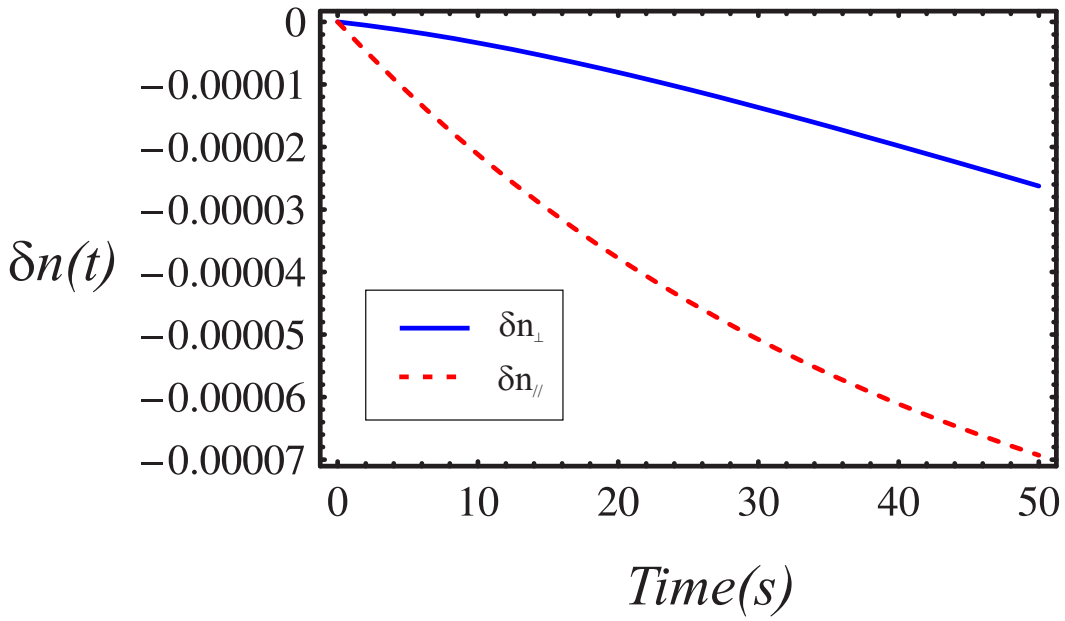

Figure 2.11: The changes of refractive indices of parallel (red dashed) and perpendicular (blue solid) to the polarization of pump when $D_t = 0.0001, I_t = 0.011$, and, $I_c = 0.0096$.

2.4.2 Calculation of the first order susceptibilities and the refractive indices

In our experiment, we use a CW light source whose energy is known to be weak enough that the refractive index changes due to a change of the electron cloud around the nuclei is smaller than the refractive index change due to isomerization. Ignoring this electronic $\chi^{(3)}$ effect, the relationship between the order parameters A_i and the tensor components of the linear electronic susceptibilities $\chi^{(1)}$ for a two dimensional molecule are given by,[3][8]

$$\begin{aligned} \chi_{11}^{(1)} &= N\bar{\alpha}^{\omega}\left(1 - r^{\omega}A_2\right), \\ \chi_{33}^{(1)} &= N\bar{\alpha}^{\omega}\left(1 + 2r^{\omega}A_2\right), \end{aligned} \tag{2.66}$$

where N is the density of molecules, $\bar{\alpha}^{\omega} = (\alpha_{\parallel}^{*} + 2\alpha_{\perp}^{*})/3$ is the isotropic molecular polarizability, $r^{\omega} = (\alpha_{\parallel}^{*} - \alpha_{\perp}^{*})/(\alpha_{\parallel}^{*} + 2\alpha_{\perp}^{*})$ is the molecule anisotropy and $\alpha_{\parallel,\perp}^{*}$ are the dressed polarizabilities along and perpendicular to the long axis, respectively.

As we have seen in previous section, the order parameters are not constant in time nor as a function of intensity. We can write the refractive index parallel and perpendicular to the polarization of the pump as follows:

$$\begin{aligned} n_{zz}(t) &= n_{\parallel} \\ &= \left[\epsilon_{zz}^{0} + 4\pi\left\{N_t(t)\bar{\alpha}^{t}\left(1 + 2r^{t}T_2(t)\right) + N_c(t)\bar{\alpha}^{c}\left(1 + 2r^{c}C_2(t)\right)\right\}\right]^{\frac{1}{2}} \\ &\simeq n_{zz}^{0} + \frac{2\pi N}{n_{zz}^{0}}\left\{T_0(t)\bar{\alpha}^{t}\left(1 + 2r^{t}T_2(t)\right) + \left(1 - T_0(t)\right)\bar{\alpha}^{c}\left(1 + 2r^{c}C_2(t)\right)\right\} \end{aligned} \tag{2.67}$$

and

$$\begin{aligned} n_{xx}(t) &= n_{\perp} \\ &= \left[\epsilon_{xx}^{0} + 4\pi\left\{N_t(t)\bar{\alpha}^{t}\left(1 - r^{t}T_2(t)\right) + N_c(t)\bar{\alpha}^{c}\left(1 - r^{c}C_2(t)\right)\right\}\right]^{\frac{1}{2}} \\ &\simeq n_{xx}^{0} + \frac{2\pi N}{n_{xx}^{0}}\left\{T_0(t)\bar{\alpha}^{t}\left(1 - r^{t}T_2(t)\right) + \left(1 - T_0(t)\right)\bar{\alpha}^{c}\left(1 - r^{c}C_2(t)\right)\right\}, \end{aligned} \tag{2.68}$$

where we have used the relationship, $n = \sqrt{1 + 4\pi\chi^{(1)}}$ and that the change in refractive index due to isomerization and reorientation is small compared to the initial refractive index. We can determine the linear refractive index of dye doped PMMA at $t = 0$ or $I = 0$, as follows:

$$\begin{aligned} n_{xx}(0) &= n^0_{xx} + \frac{2\pi N\bar{\alpha}^t}{n^0_{xx}} \\ &= n^0_{PMMA} + n^0_{DR1} \\ &= n_0 \end{aligned} \tag{2.69}$$

and

$$\begin{aligned} n_{zz}(0) &= n^0_{zz} + \frac{2\pi N\bar{\alpha}^t}{n^0_{zz}} \\ &= n^0_{PMMA} + n^0_{DR1} \\ &= n_0, \end{aligned} \tag{2.70}$$

where n^0_{PMMA} is the linear refractive index of PMMA and n^0_{DR1} is the additional linear refractive index due to the DR1 dye molecules, which is consistent with the initial condition $(t = 0; I = 0)$ that most of the molecules are trans-isomers in random angular distribution as we have assumed in section 2.4.1.

Finally, we can separate the linear and nonlinear part of refractive index as follows:

$$\begin{aligned} n_{xx} &= n_0 + \delta n_\perp \\ &= n_0 + \frac{2\pi N}{n^0_{PMMA}} \left\{ T_0(t)\bar{\alpha}^t \left(1 - r^t T_2(t)\right) \right. \\ &\quad \left. + \left(1 - T_0(t)\right) \bar{\alpha}^c \left(1 - r^c C_2(t)\right) - \bar{\alpha}^t \right\} \end{aligned} \tag{2.71}$$

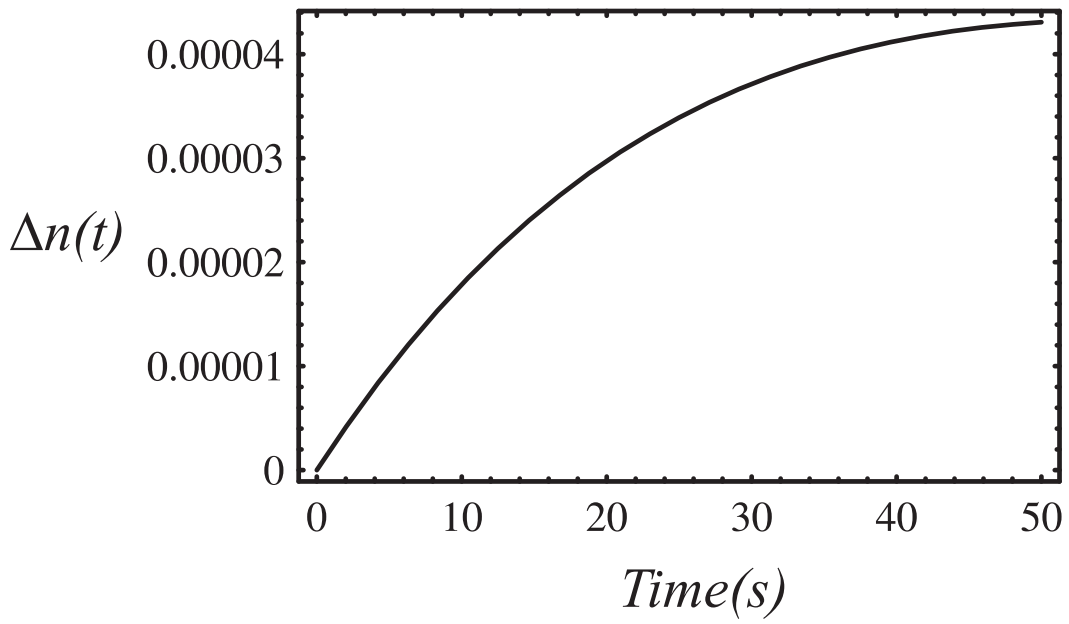

Figure 2.12: Birefringence, $\Delta n(t)$when photothermal heating is negligible. $I_t = 0.011$ and $I_c = 0.00946$.

and

$$\begin{aligned} n_{zz} &= n_0 + \delta n_{\parallel} \\ &= n_0 + \frac{2\pi N}{n^0_{PMMA}} \left\{ T_0(t)\bar{\alpha}^t \left(1 + 2r^t T_2(t)\right) \right. \\ &\quad \left. + \left(1 - T_0(t)\right) \bar{\alpha}^c \left(1 + 2r^c C_2(t)\right) - \bar{\alpha}^t \right\}, \end{aligned} \tag{2.72}$$

where n_0 is the linear refractive index of the host and dye and $\delta n_{\parallel}$ and $\delta n_{\perp}$ are the intensity dependent refractive indices for parallel and perpendicular to the polarization of the pump, respectively. Note that δn is a function of time.

We can define the birefringence as the difference between the parallel and perpendicular refractive indices:

$$\begin{aligned} \Delta n &= n_{xx} - n_{zz} \\ &= -\frac{2\pi N}{n^0_{PMMA}} \left\{ 3\bar{\alpha}^t r^t T_0 T_2 + 3\bar{\alpha}^c r^c \left(1 - T_0\right) C_2 \right\}. \end{aligned} \tag{2.73}$$

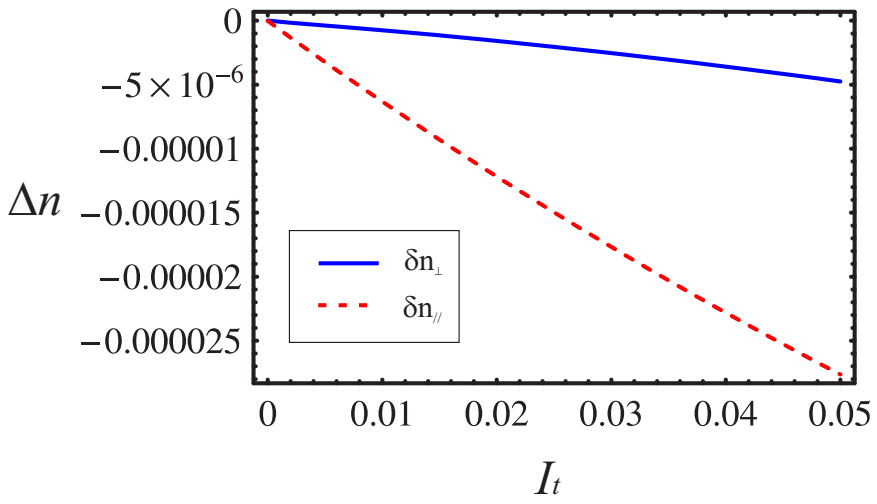

Figure 2.13: The change of refractive indices of parallel(red dashed) and perpendicular(blue solid) polarizations when $t = 3$ in low intensity region. The refractive index change is negative.

Figure 2.12 shows the birefringence as a function of time when $I_t = 0.011$, $I_c = 0.00946$, and $D_t = 0.0001$. Figure 2.13 shows the nonlinear refractive indices of parallel and perpendicular in low intensity limit at $t = 3s$ where the relationship between δn and I_t appear linear. On the other hand, Figure 2.14 shows $\delta n_{\|}$ and $\delta n_{\perp}$ at high intensity. The refractive indices saturate as the intensity increases and the high intensity limit, they are very close to each other.

2.5 Brownian motion of dyes in a polymer

In this section, we review the effect of Brownian motion of dyes in polymers, based on Reference,[7] considering cigar-shaped molecules as we have modeled in the previous section. By understanding this process, we should be able to understand how local and nonlocal optical effects are coupled.We begin by considering particle diffusion, followed by rotational diffusion.

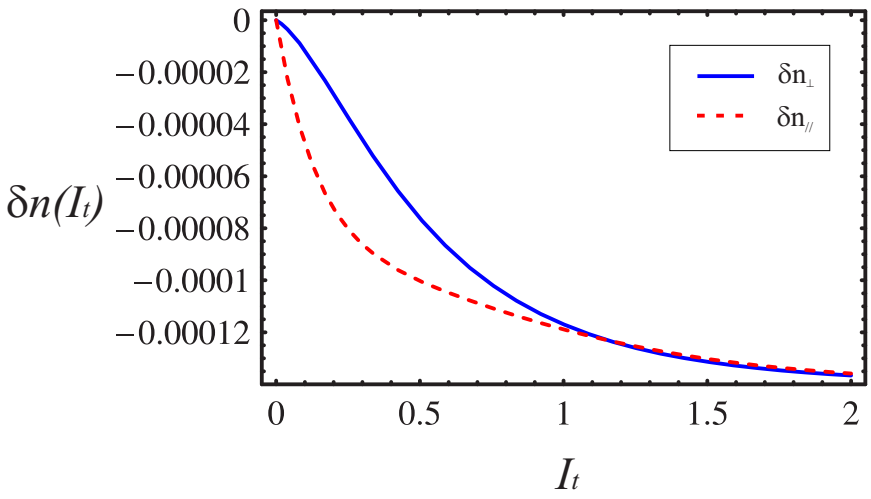

Figure 2.14: The change of refractive indices of parallel(red dashed) and perpendicular(blue solid) polarizations when $t = 3$ in high intensity region. The refractive index saturates as the intensity increases.

2.5.1 Diffusion of particles in 1-D

The process of diffusion is phenomenologically described by Fick's law, which says that if concentration is not uniform, there is a flux, $j(x,t)$, such as

$$j(x,t) = -D\frac{\partial C}{\partial x}, \tag{2.74}$$

where C is the concentration of particles and D is the diffusion constant. When there is no sink and source, the continuity equation,

$$\frac{\partial C}{\partial t} = -\frac{\partial j}{\partial x}, \tag{2.75}$$

should be satisfied. By substituting Equation (2.74) into (2.75), we get the diffusion equation for the concentration of molecules,

$$\frac{\partial C}{\partial t} - D\frac{\partial^2 C}{\partial x^2} = 0. \tag{2.76}$$

When the particles are in a viscous medium, a weak resistant force, F, is proportional to the velocity:

$$\begin{aligned} F &= -\frac{\partial U}{\partial x} \\ &= \zeta v \end{aligned}$$

or

$$v = -\frac{1}{\zeta}\frac{\partial U}{\partial x}, \tag{2.77}$$

where ζ is the friction constant. This leads to an additional flux Cv on Equation (2.74) which becomes

$$j(x,t) = -D\frac{\partial C}{\partial x} - \frac{C}{\zeta}\frac{\partial U}{\partial x}. \tag{2.78}$$

In equilibrium, the concentration is given by the Boltzmann distribution,

$$C_{eq} \propto \exp[-U(x)/k_B T], \tag{2.79}$$

and the flux, $j(x,t)$, is zero, which gives us the Einstein relation,

$$D = \frac{k_B T}{\zeta}. \tag{2.80}$$

By substituting Equation (2.80) into (2.78), the flux equation becomes

$$\begin{aligned} j &= -\frac{1}{\zeta}\left(k_B T\frac{\partial C}{\partial x} + C\frac{\partial U}{\partial x}\right) \\ &= -\frac{1}{\zeta}C\frac{\partial}{\partial x}\left(k_B T \ln C + U\right) \end{aligned} \tag{2.81}$$

Note that $k_B T \ln C + U$ is the chemical potential. By substituting Equation (2.81) into

Equation (2.75), the continuity equation becomes

$$\frac{\partial C}{\partial t} = \frac{\partial}{\partial x}\frac{1}{\zeta}\left(k_B T\frac{\partial C}{\partial x} + C\frac{\partial U}{\partial x}\right), \tag{2.82}$$

which is known as the Smoluchowski equation.

2.5.2 Rotational Brownian motion

In the previous section, we described Brownian motion in 1 dimension. In this section, we are going to extend the translational Brownian motion in one dimension to the case of rotational Brownian motion. In the rotational frame, the linear velocity is analogous to the angular velocity and the force is analogous to the torque. The angular velocity is given by

$$\omega = -\frac{1}{\zeta_r}\mathbf{R}U, \tag{2.83}$$

where ζ_r is the rotational friction constant and $\mathbf{R}$ is the rotational operator given by $\mathbf{u} \times \frac{\partial}{\partial \mathbf{u}}$ and $\mathbf{u}$ is the unit vector in the direction of the long axis of the molecule. In a similar manner as we have done in Equation (2.82), we get the angular diffusion equation,

$$\begin{aligned}\frac{\partial C}{\partial t} &= \frac{1}{\zeta_r}\mathbf{R}\cdot(k_B T\mathbf{R}C + C\mathbf{R}U) \\ &= D_r\mathbf{R}\cdot\left(\mathbf{R}C + \frac{C}{k_B T}\mathbf{R}U\right),\end{aligned} \tag{2.84}$$

where the rotational diffusion constant,

$$D_r = k_B T/\zeta_r. \tag{2.85}$$

Note that we have used this result when considering thermal rotational diffusion as given by Equations (2.49) and (2.50).

2.6 The refractive index due to coupling between photo isomerization and photo thermal heating

In Section 2.4.1, we have calculated the nonlinear refractive index due to the change of order parameters when molecules reorient due to photo isomerization. The order parameters are related to the rotational diffusion constants $D_{t,c}$ which are related to the temperature. Note that $D_{t,c}$ are the rotational diffusion constants for trans and cis isomers, respectively.

In Equation (2.85), $D_{t,c}$ are proportional to temperature. We can vary the angular diffusion constants by controlling the temperature directly with an oven and indirectly by photothermal heating. In this section, we show how the refractive index changes in each of these methods.

2.6.1 The refractive index as a function of the external temperature

We have calculated the dependence of the refractive indices on temperature in Equations (2.71) and (2.72). In this section, we show how the refractive index changes relate to temperature at a low fixed beam intensity with the assumption that photothermal heating is negligible compared with the temperature change due to the external heat source.

Figures 2.15 and 2.16 show the time dependence of the refractive index. As the sample temperature increases, the magnitude of the parallel component of the refractive index decreases while the perpendicular component of the refractive index increases. As such, we control the temperature independently with the intensity of the pump beam. Figure 2.17 shows the birefringence change as a function of time and temperature. As the temperature increases and the diffusion constants increase, the birefringence, Δn decreases as the molecules approach random orientation. We can test these results by measuring the temperature-dependent optical kerr effect (OKE) of a sample in an oven.

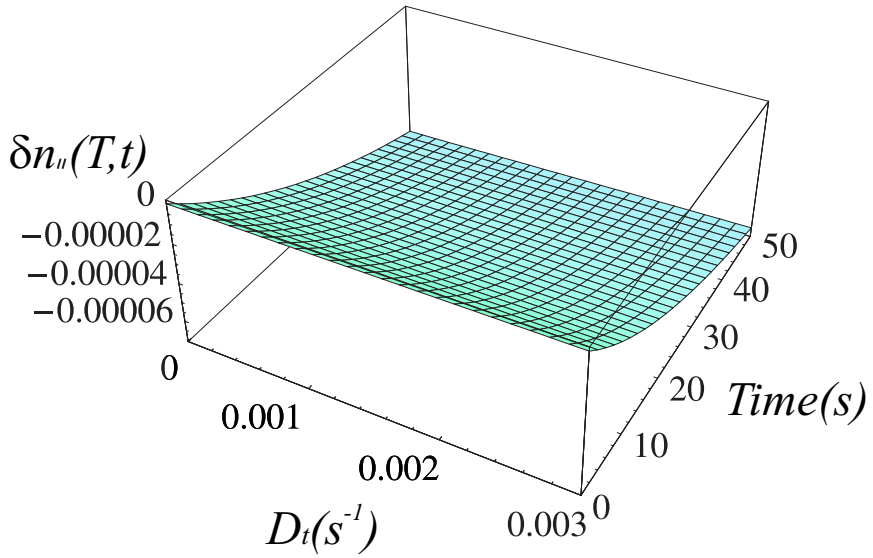

Figure 2.15: The refractive index parallel to the pump polarization. As the temperature increases, D_t, the rotational diffusion constant of the trans molecules, increases and the magnitude of the parallel refractive index decreases. $I_t = 0.011$ and $I_c = 0.00946$

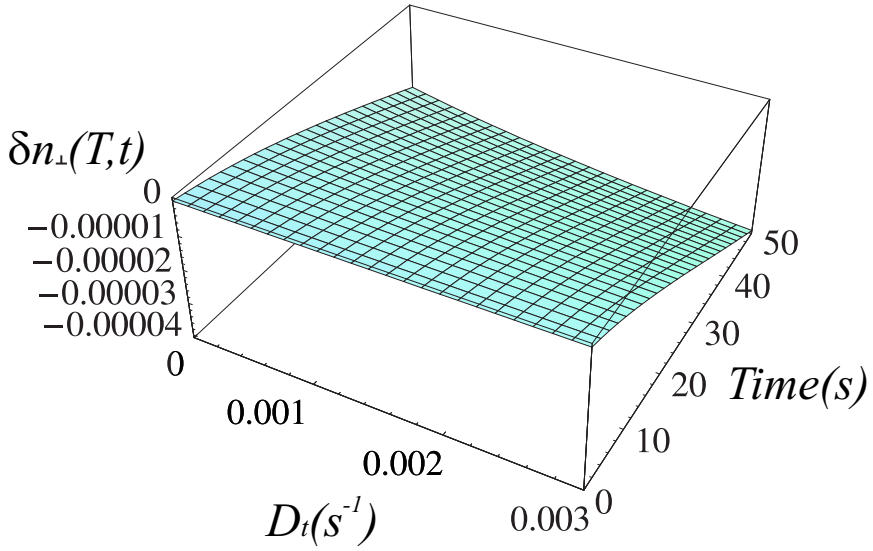

Figure 2.16: The refractive index perpendicular to the pump polarization. As the temperature increases, D_t, the rotational diffusion constant of the trans molecules, increases and the magnitude of the refractive index increases. $I_t = 0.011$ and $I_c = 0.00946$.

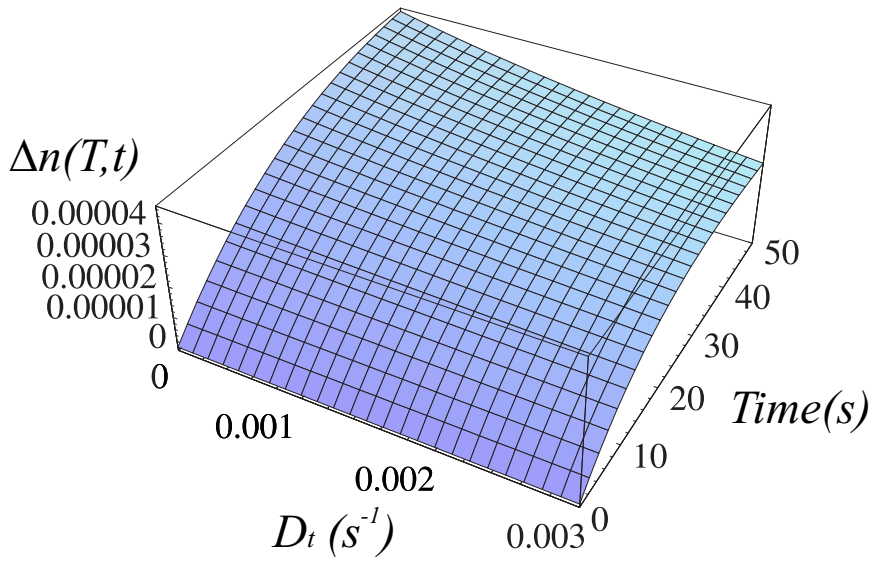

Figure 2.17: $\Delta n(T,t)$ as a function of D_t in the range from $D_t = 0$ to $D_t = 0.003$ and the time in the range from $t = 0$ to $t = 50$. $I_t = 0.011$ and $I_c = 0.00946$.

2.6.2 The refractive index due to photothermal heating at fixed beam intensity

In this section, we consider the beam of light as a heat source through photothermal heating and include the thermal effect of angular diffusion by incorporating the laser heat source into the diffusion constant.

We can find the change in temperature due to the intensity by using the relationship $\Delta n = n_2 I = -\frac{\partial n}{\partial T}\delta T$, where δT is the temperature difference from ambient and the negative sign is for defocusing. As we have derived in Section 2.3, by using Equation (2.48), we get the temperature as follows:

$$\begin{aligned} \delta T &= \frac{\alpha a^2 I}{8\kappa\,(1+\tau/2t)} \\ &= \frac{\alpha P}{4\pi\kappa\,(1+\tau/2t)}. \end{aligned} \tag{2.86}$$

Equation (2.86) shows that the temperature is proportional to the area of the beam waist and the intensity. Therefore, the temperature is proportional to the power. The beam waist,

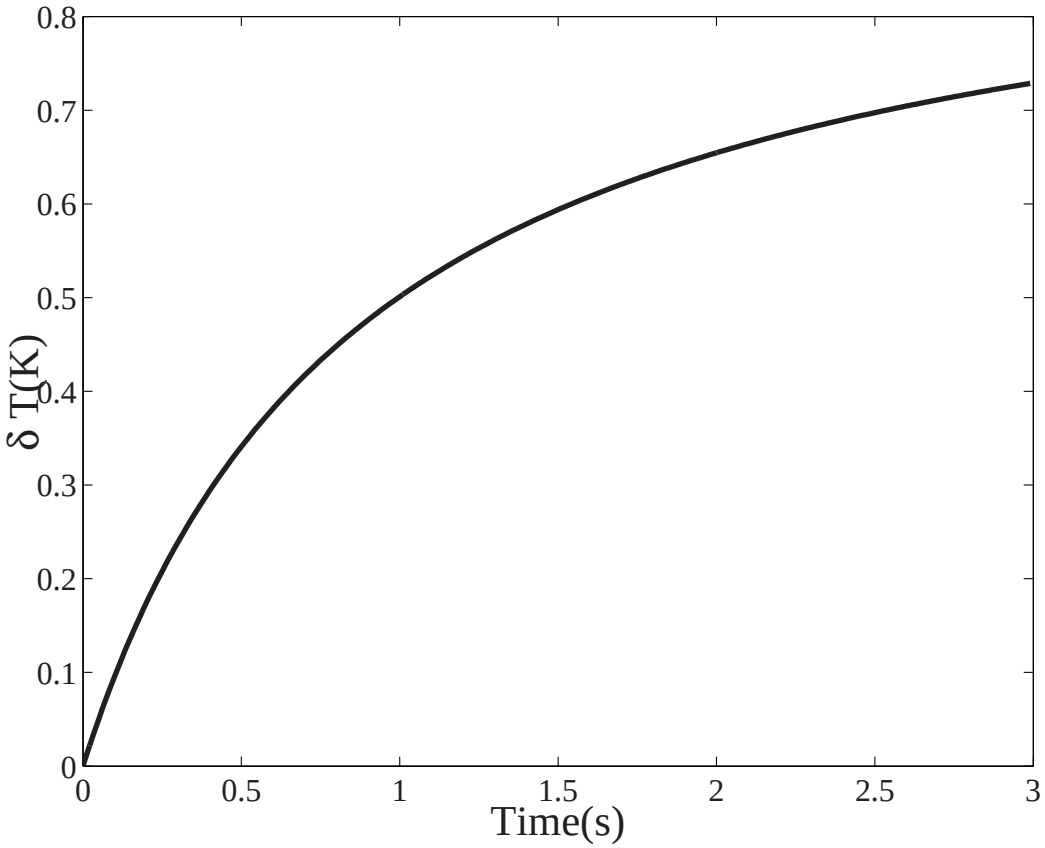

Figure 2.18: Equation (2.86) as a function of time, with a pump intensity of $600mW/cm^2$, absorption coefficient $\alpha = 3cm^{-1}$, thermal conductivity $\kappa = 0.193W/m \cdot K$, beam radius $a = 900\mu m$, density $\rho = 1.19 \times 10^3 kg/m^3$, and specific heat $c = 1.42 \times 10^3 J/kg \cdot K$.

a, also contributes to the time constant τ since the temperature saturates faster as a gets smaller, assuming of course, that all other parameters are held constant. Figure 2.18 shows how the temperature increases in the sample as a function of time as given by Equation (2.86).

To couple the thermal mechanisms leading to refractive index changes that we obtained in Section 2.4.2, we use the diffusion constant defined by the Einstein relation, which includes

the temperature. The Einstein relation for rod-like molecules is given by[7]

$$\begin{aligned} D_{t,c} &= \frac{4k_BT}{\pi\eta_s L_{t,c}^3} \\ &= \frac{k_B\alpha a^2 I}{2\pi\eta_s\kappa\left(1+\tau/2t\right)L_{t,c}^3} \\ &= \frac{k_B\alpha P}{\pi^2\eta_s\kappa\left(1+\tau/2t\right)L_{t,c}^3}, \end{aligned} \tag{2.87}$$

where we have used Equation (2.86) for T, $L_{t,c}$ are the lengths of the trans and cis molecules along their principle axes, and η_s is the viscosity of PMMA. The relationship between D_t and D_c is found to be

$$D_t \simeq 6D_c, \tag{2.88}$$

which we have calculated in appendix 2.8.3.

In Equation (2.87), the angular diffusion constant is a linear function of power. The time constant, τ, is proportional to a^2. Therefore, we predict that for small beam size and low power, the temperature and the time constant are small, which results in a small thermal effect. On the other hand, for larger beam size and larger power but with fixed intensity as in the previous case, the thermal mechanism contributing to Δn is larger with a larger time constant. Figures 2.19 and 2.20 show the refractive index changes as a function of time, where the temperature is controlled with the power. To keep the intensity fixed, the gaussian beam waist is given by

$$a = \sqrt{\frac{2P}{\pi I_p}}, \tag{2.89}$$

where I_p is the peak intensity. In this way, we are able to emulate temperature change without affecting the intensity.

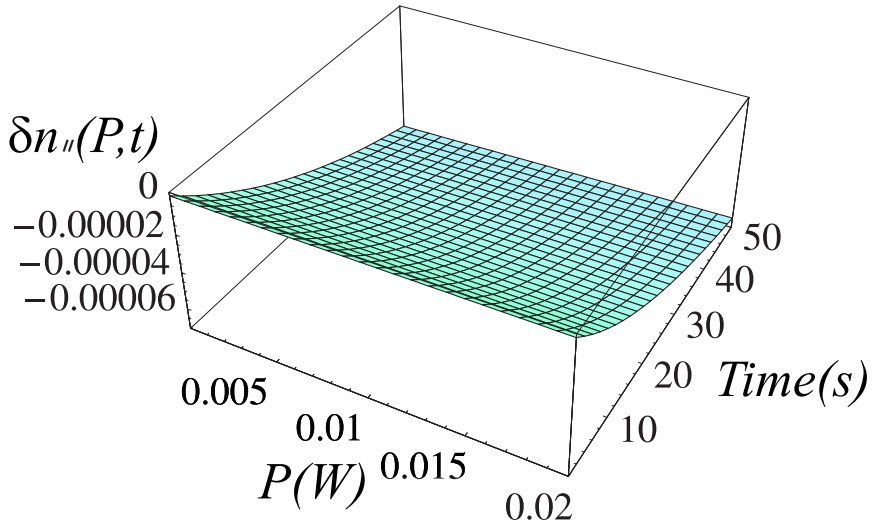

Figure 2.19: The refractive index parallel to the pump polarization. As laser power increases, the magnitude of the refractive index decreases.

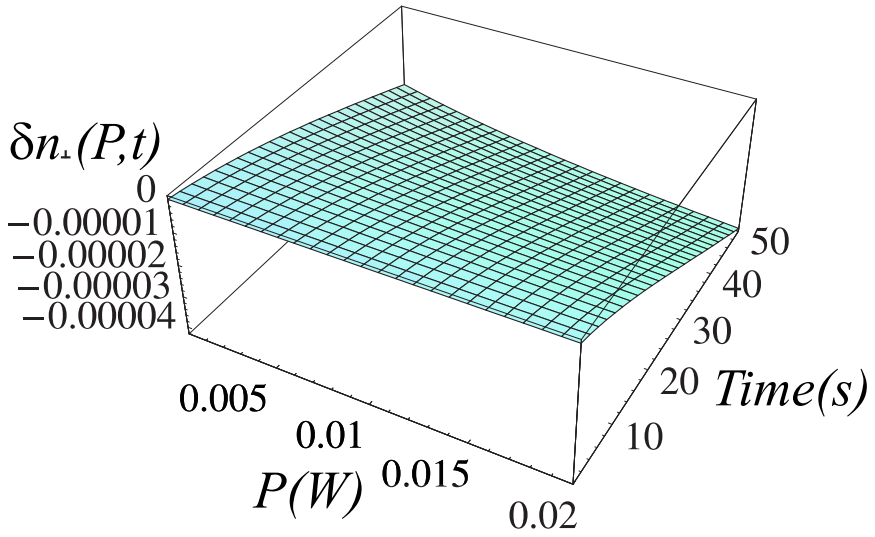

Figure 2.20: The refractive index perpendicular to the pump polarization. As the laser power increases, the magnitude of the refractive index increases.

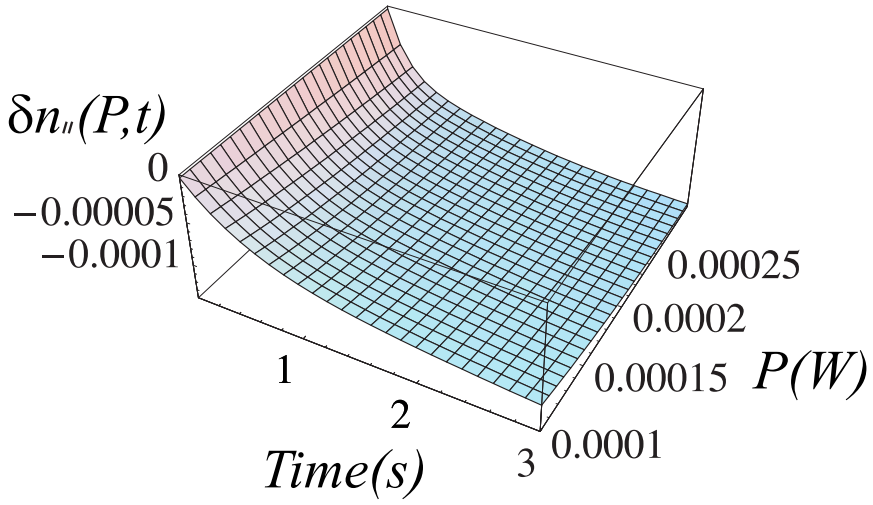

Figure 2.21: The parallel component of the refractive index change becomes more negative as power and intensity increases. Beam size $a = 0.09cm$ and kinetic viscosity of PMMA, $\eta_s = 10^{10} N \cdot s/cm^2 = 10^{14} Pa \cdot s$.

2.6.3 The refractive index due to photothermal heating with a fixed beam waist

When keeping the beam waist fixed and increasing the intensity, the power will increase in proportion to the intensity. Figure 2.21 shows the change of the refractive index as a function of time with increasing power while keeping the beam waist constant. As intensity increases, the change of refractive index increases. By using the nonlinear refractive index relationship, $\Delta n = n_2 I_p$, we get n_2, which is plotted in Figure 2.22. As intensity increases, the magnitude of the nonlinear refractive index, n_2, decreases. In Figure 2.22, we see that thermal agitation reduces the magnitude of n_2 while increasing the temperature in the sample. Recall that an increase of the beam waist (See the previous section) corresponds to thermal defocusing. On the other hand, when the beam waist is constant, more thermal agitation of the molecules results. This is observed in Z-scan experiments for DB14 and DR1, which we will discuss in Chapters 3 and 4.

To eliminate the thermal effect, we need to use a small diameter and a low power of the single beam Z-scan experiment. Since intensity is power per unit area, under these

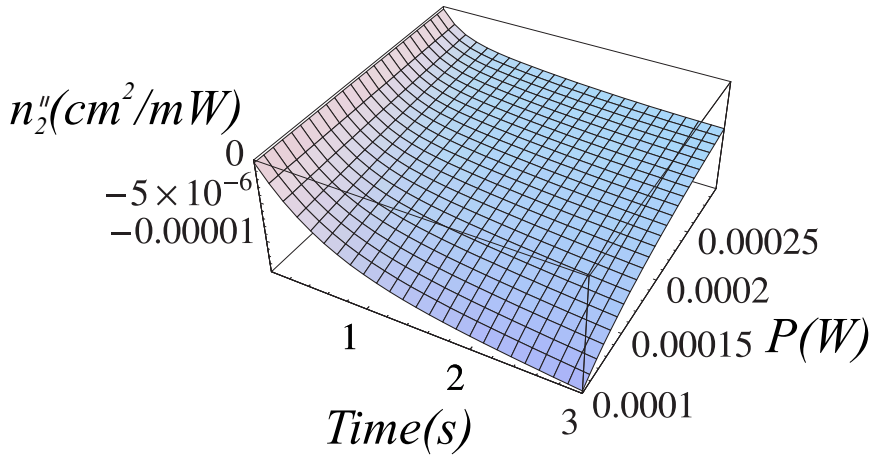

Figure 2.22: The parallel component of the nonlinear refractive index $n_2^{\parallel} = \delta n_{\parallel}/I_p$, where I_p is the peak intensity for a given power, P. Parameters used are the same as in Figure 2.21

conditions, the intensity can be large. Note we will discuss the experimental results of how power, intensity, and the beam size are related to the nonlinear refractive indices in Chapter 4.

2.7 Summary

In this chapter, we have derived our theory that generalized the nonlinear refractive index by using the on-axis normalized transmittance through a small aperture and Akhmanov's self-(de)focusing theory under the condition that the beam waist is larger than the thickness of the sample and the radius of the gaussian beam is large enough to consider it a collimated beam ($R \gg 1$) over the thickness of the sample.

For the photothermal effect, we have derived the nonlinear refractive index as a function of time as a nonlocal nonlinear optical process by solving the temperature-dependent diffusion equation with a heat source of the laser related to the linear absorption in the sample. Consequently, the spatial temperature gradient developed by the heat source causes the refractive index change. The on-axis temperature in the sample as a function of time is obtained as:

$$T = \frac{\alpha P}{4\pi\kappa\left(1+\tau/2t\right)}. \tag{2.90}$$

For the photo-isomerization mechanism of our model, we have started with Sekkat's model[3] and modified it in the low intensity, short time regime (the probability of cis to trans is ignorable in short time, $P_n^{ct} \rightarrow 0$), and for a slow rate of cis to trans thermal relaxation ($\gamma \rightarrow 0$) as:

$$\frac{dT_n}{dt} = -I_t\{T\} - T_n n\left(n+1\right) D_t \tag{2.91}$$

and

$$\frac{dC_n}{dt} = -I_c\{C\} + I_t P_n^{tc}\{T\} - C_n n\left(n+1\right) D_c. \tag{2.92}$$

Since CW laser in low intensity was used for our experiment, the refractive index changes as a function of time due to the molecular reorientation which is directly related to the order parameters. As such, we calculated the refractive index change as a function of time from $\chi^{(1)}(t)$:

$$\delta n_{\perp}(t) = \frac{2\pi N}{n_{PMMA}^0}\left\{T_0(t)\bar{\alpha}^t\left(1 - r^t T_2(t)\right) + \left(1 - T_0(t)\right)\bar{\alpha}^c\left(1 - r^c C_2(t)\right) - \bar{\alpha}^t\right\} \tag{2.93}$$

and

$$\delta n_{\parallel}(t) = \frac{2\pi N}{n_{PMMA}^0}\left\{T_0(t)\bar{\alpha}^t\left(1 + 2r^t T_2(t)\right) + \left(1 - T_0(t)\right)\bar{\alpha}^c\left(1 + 2r^c C_2(t)\right) - \bar{\alpha}^t\right\}. \tag{2.94}$$

Finally, we combined photothermal and photo-isomerization mechanisms by introducing temperature-dependent coupling in the angular molecular diffusion constants, $D_{t,c}$, via the Einstein relation which describes the effects of temperature agitation on the angular distribution of the molecules. As we increase the intensity of the laser, the number of reoriented molecules increase and also temperature in the sample increases from photothermal effect. In

this final model, we understand how the photothermal and molecular reorientation following photo-isomerization are competing each other, which is a new analytical theory.

Our theory shows:

1. The birefringence decreases in higher temperature to show how the temperature in the sample agitates the anisotropic angular molecular distribution due to the molecular reorientation following the photo-isomerization (See Figure 2.17).

2. The parallel component of the nonlinear refractive index, $n_2^{\parallel}$ reduces the magnitude as the power of the beam increases since the power is linear to the temperature in the sample due to photothermal effect. (See Figure 2.22).

2.8 Appendices

In these appendices, we fill in the details of the calculations presented in this chapter.

2.8.1 Appendix A: Solving for the dimensionless beam waist function

In this Appendix, we show the details leading to Equation (2.6). Substituting Equation (2.4) into Equation (2.2) and (2.3) yields

$$r^2\left[\beta^2+\frac{\partial\beta}{\partial z}+\frac{2}{f^{1+m}}\frac{\epsilon_2}{\epsilon_0}\frac{E_0^2}{a^2f^2}\right]+\frac{\partial\varphi}{\partial z}-\frac{\epsilon_2}{2\epsilon_0}\frac{E_0^2}{f^{1+m}}=0 \tag{A-1}$$

and

$$2r^2\frac{E_0^2}{a^2f^2}\frac{m+3}{f^{1+m}}\left(\frac{1}{f}\frac{\partial f}{\partial z}-\beta\right)-\frac{(m+1)E_0^2}{f^{1+m}}\left(\frac{1}{f}\frac{\partial f}{\partial z}-\beta\right)=0, \tag{A-2}$$

respectively. Equation (A-1) and (A-2) leads to

$$\begin{aligned}\frac{\partial\varphi}{\partial z} &= \frac{\epsilon_2}{2\epsilon_0}\frac{E_0^2}{f^{1+m}},\\ \beta &= \frac{1}{f}\frac{\partial f}{\partial z},\end{aligned} \tag{A-3}$$

and

$$\frac{\partial^2 f}{\partial z^2}=-\frac{\epsilon_2}{\epsilon_0}\frac{E_0^2}{f^{2+m}a^2}. \tag{A-4}$$

By multiplying Equation (A-4) by $\frac{df}{dz}$ and integrating over z, we get

$$\left(\frac{\partial f}{\partial z}\right)^2=\frac{2}{1+m}\frac{\epsilon_2}{\epsilon_0}\frac{E_0^2}{f^{1+m}a^2}+C. \tag{A-5}$$

We can determine C by using the boundary condition given by Equation (2.5). For a three dimensional beam($m = 1$), we have

$$\left(\frac{\partial f}{\partial z}\right)^2 = \frac{\epsilon_2}{\epsilon_0}\frac{E_0^2}{a^2}\left(\frac{1}{f^2} - 1\right) + \frac{1}{R^2}. \tag{A-6}$$

We do the integral by using

$$\begin{aligned}\frac{\partial^2 f^2}{\partial z^2} &= \frac{\partial}{\partial z}\left(\frac{\partial f^2}{\partial z}\right) = \frac{\partial}{\partial z}\left(2f\frac{\partial f}{\partial z}\right) = 2\left(\frac{\partial f}{\partial z}\right)^2 + 2f\frac{\partial^2 f}{\partial z^2} \\ &= \frac{1}{R^2} - \frac{2\epsilon_2}{\epsilon_0}\frac{E_0^2}{a^2},\end{aligned} \tag{A-7}$$

where we have used Equation (A-4) and (A-5) with the condition of a 3-dimensional beam ($m = 1$) to get the righthand side. Finally, we integrate Equation (A-7) by using the boundary condition given by Equation (2.5),

$$f^2(z) = \left(\frac{1}{R^2} - \frac{2\epsilon_2 E_0^2}{\epsilon_0 a^2}\right) z^2 + \frac{2}{R}z + 1. \tag{A-8}$$

2.8.2 Appendix B: Thermal Diffusion

Integration of the radial component to get the temperature

In this appendix, we shows the details that lead to the derivation of Equation (2.36),

$$\Delta T(r, z) = \int_0^\infty \exp\left(-\frac{2r'^2}{a^2 f^2}\right) \exp\left(-\frac{r'^2}{4Dt'}\right) I_0\left(\frac{rr'}{2Dt'}\right) r' dr'. \tag{B-1}$$

To be able to integrate Equation (B-1), we use the relationship:

$$\int_0^\infty I_0\left(\alpha r'\right) \exp\left(-p^2 r'^2\right) r' dr' = \frac{1}{2p^2} \exp\left(\frac{\alpha^2}{4p^2}\right), \tag{B-2}$$

By comparing Equation (B-1) and (B-2), we get that $p^2 = \frac{2}{a^2 f^2} + \frac{1}{4Dt'}$ and $\alpha = \frac{r}{2Dt'}$, which leads to

$$\Delta T(r,z) = \frac{2Dt'}{1 + 8Dt'/a^2 f^2} \exp\left[\frac{r^2}{4Dt'\left(1 + 8Dt'/a^2 f^2\right)}\right]. \tag{B-3}$$

Integration of time component to get the temperature

In this appendix, we shows the details of deriving Equation (3.26).

$$\Delta T(r,z,t) = \frac{I_p \alpha \exp(-\alpha z)}{a^2 f^2 \rho c} \int_0^t dt' \frac{1}{1 + \frac{8D}{a^2 f^2} t'} \exp\left[-\frac{2r^2}{a^2 f^2 \left(1 + \frac{8Dt'}{a^2 f^2}\right)}\right]. \tag{B-4}$$

By making the following substitutions,

$$y = (1 + \frac{8Dt'}{a^2 f^2})^{-1} \quad \text{and} \quad dy = -\frac{8D}{a^2 f^2} y^{-2} dt', \tag{B-5}$$

we evaluate the integral part of Equation (B-4) as follows:

$$\begin{aligned}
\int_0^t dt' \frac{1}{1 + \frac{8D}{a^2 f^2} t'} \exp\left[-\frac{2r^2}{a^2 f^2 \left(1 + \frac{8Dt'}{a^2 f^2}\right)}\right] &= -\frac{a^2 f^2}{8D} \int_1^{(1 + \frac{8Dt}{a^2 f^2})^{-1}} \frac{\exp\left(-\frac{2r^2}{a^2 f^2} y\right)}{y} dy \\
&= \frac{a^2 f^2 \rho c}{8\kappa} \left[Ei\left(-\frac{2r^2}{a^2 f^2}\right)\right. \\
&\quad \left. -Ei\left(-\frac{2r^2}{a^2 f^2 \left(1 + \frac{8Dt}{a^2 f^2}\right)}\right)\right],
\end{aligned} \tag{B-6}$$

where we have used the definition of the exponential integral function Ei:

$$Ei\left(-ax\right) = \int \frac{\exp\left(-ax\right)}{x} dx. \tag{B-7}$$

Solving for the dimensionless beam waist of the thermal effect

In this appendix, we show the details for the derivation of Equation (2.39) to (2.42). We use the ray inclination to the beam axis $u = \frac{r}{f}\frac{df}{dz}$, then Equation (2.39) gives us

$$-\frac{r}{f^2}\left(\frac{df}{dz}\right)^2 + \frac{r}{f}\frac{d^2f}{dz^2} + \frac{r}{f^2}\left(\frac{df}{dz}\right)^2 = -\frac{1}{n_0}\frac{\partial n}{\partial T}\frac{\partial T}{\partial r}, \tag{B-8}$$

which leads to Equation (2.41). Therefore, Equation (2.41) becomes

$$\begin{aligned}
\frac{d^2f}{dz^2} &= \frac{I_p a^2 \alpha \exp(-\alpha z)}{4\kappa}\left(\frac{f}{r}\right)\left(-\frac{1}{n_0}\frac{\partial n}{\partial T}\right)\left[\frac{\exp\left(-\frac{2r^2}{a^2f^2}\right) - \exp\left(-\frac{2r^2}{a^2f^2\left(1+\frac{8Dt}{a^2f^2}\right)}\right)}{r}\right] \\
&\simeq -\frac{I_p a^2 \alpha \exp(-\alpha z)}{4\kappa}\left(\frac{1}{n_0}\frac{\partial n}{\partial T}\right)\left(\frac{f}{r^2}\right)\left[1 - \frac{2r^2}{a^2f^2} - 1 + \frac{2r^2}{a^2f^2\left(1+\frac{8Dt}{a^2f^2}\right)}\right] \\
&= \frac{I_p a^2 \alpha \exp(-\alpha z)}{4\kappa}\left(\frac{1}{n_0}\frac{\partial n}{\partial T}\right)\left(\frac{f}{r^2}\right)\left(\frac{2r^2}{a^2f^2}\right)\left(1 + \frac{a^2f^2}{8Dt}\right)^{-1} \\
&= \frac{I_p \alpha \exp(-\alpha z)}{2n_0\kappa f}\frac{\partial n}{\partial T}\left[1 + f^2(\tau/2t)\right]^{-1},
\end{aligned} \tag{B-9}$$

where we have used the approximation of the on-axis condition.

Solving for the normalized transmittance for the thermal effect

In this appendix we show the details leading to Equation (2.46). By substituting $f^2(L)$ which we have found in Equation (2.45), we get

$$\begin{aligned}
\mathcal{T} &= \frac{1 - \exp\left(-\frac{2r_d^2}{a^2}\right)\exp\left(\frac{2r_d^2}{a^2}B\alpha^2L^2\right)}{1 - \exp\left(-\frac{2r_d^2}{a^2}\right)} \\
&\simeq \frac{1 - \exp\left(-\frac{2r_d^2}{a^2}\right)\left(1 + \frac{2r_d^2}{a^2}B\alpha^2L^2\right)}{1 - \exp\left(-\frac{2r_d^2}{a^2}\right)} \\
&\simeq 1 - B\alpha^2L^2 \\
&= 1 - \frac{\alpha L^2}{2n_0\kappa(1 + \tau/2t)}\frac{\partial n}{\partial T}I_p,
\end{aligned} \tag{B-10}$$

where we have used the conditions that the argument $\frac{2r_d^2}{a^2}B\alpha^2L^2$ is very small compared to unity and that $r_d \ll a$.

2.8.3 Appendix C: Photo-isomerization mechanism and parameters

Simplifying the population differential equation

In this appendix, we show the details of deriving Equation (2.49) and (2.50) to Equation (2.51) and (2.52) using the orthogonality of Legendre polynomials.

The normalization conditions are given by

$$\begin{aligned} \iint n_{t,c}(\Omega)\, d\Omega &= N_{t,c}, \\ N_t + N_c &= N, \\ \iint P^{ct,tc}(\Omega' \to \Omega)\, d\Omega' &= 1, \\ \iint Q(\Omega' \to \Omega)\, d\Omega' &= 1, \end{aligned} \tag{C-1}$$

where N_t and N_c are the molecular densities of the trans and the cis states, respectively, and N is the total molecular density.

Since random molecular distribution is azimuthally symmetric about the pump beam polarization direction, we consider the eigenfunction of the system in terms of the Legendre polynomials[8]. The cis and trans populations can be described in terms of orientational distribution functions $n_c(\vec{\Omega})$ and $n_t(\vec{\Omega})$:

$$\begin{aligned} n_t(\Omega) &= \frac{1}{2\pi}\sum_{n=0}^{\infty}\frac{2n+1}{2}T_nP_n(\cos\theta) \\ &\text{and} \\ n_c(\Omega) &= \frac{1}{2\pi}\sum_{k=0}^{\infty}\frac{2k+1}{2}C_kP_k(\cos\theta). \end{aligned} \tag{C-2}$$

By using orthogonality of the polynomials, we find that

$$\begin{aligned} T_n &= \int_0^{\pi} n_t(\theta) P_n(\cos\theta) \sin\theta d\theta \\ \text{and} & \\ C_n &= \int_0^{\pi} n_c(\theta) P_n(\cos\theta) \sin\theta d\theta. \end{aligned} \tag{C-3}$$

We can write the redistribution processes in the same fashion with the rotation angle χ between Ω' and Ω as follows:

$$\begin{aligned} P^{ct}(\chi) &= \frac{1}{2\pi} \sum_{q=0}^{\infty} \frac{2q+1}{2} P_q^{ct} P_q(\cos\chi), \\ P^{tc}(\chi) &= \frac{1}{2\pi} \sum_{q=0}^{\infty} \frac{2q+1}{2} P_q^{tc} P_q(\cos\chi), \\ \text{and} & \\ Q(\chi) &= \frac{1}{2\pi} \sum_{m=0}^{\infty} \frac{2m+1}{2} Q_m P_m(\cos\chi), \end{aligned} \tag{C-4}$$

where P_q^{ct} and P_q^{tc} are the order parameters of angular redistribution of a cis to trans molecule and a trans to cis molecule, respectively. By multiplying Equation (2.49) by $P_n(\cos\theta)$ and by using orthogonality of the Legendre polynomials, we get Equation (2.51) and (2.52). When $n = m$, the LHS of Equation (2.49) is

$$\begin{aligned} \frac{d}{dt} \iint n_t(\vec{\Omega}) P_m(\cos\theta) d\Omega &= \frac{d}{dt} \left[\frac{1}{2\pi} \iint \sum_{n=0}^{\infty} \frac{2n+1}{2} T_n P_n(\cos\theta) P_m(\cos\theta) d\Omega \right] \\ &= \frac{dT_m}{dt}. \end{aligned} \tag{C-5}$$

The first term of the RHS of Equation (2.49) has the zeroth and the second order combinations of Legendre polynomials. In the same manner as Equation (C-5), we can rewrite the

RHS of Equation (2.49) to zeroth order as

$$-I\phi_{tc}\sigma_{\perp}^{t}\iint n_t(\vec{\Omega})P_m(\cos\theta)d\Omega = -I\phi_{tc}\sigma_{\perp}^{t}T_m \tag{C-6}$$

For the second order term, we need to use the recursion relationship:

$$\begin{aligned} x^2P_n(x) &= \frac{(n+1)(n+2)}{(2n+1)(2n+3)}P_{n+2}(x) \\ &+ \left[\frac{(n+1)^2}{2n+3}+\frac{n^2}{2n-1}\right]\frac{P_n(x)}{2n+1} \\ &+ \frac{n(n-1)}{(2n-1)(2n+1)}P_{n-2}(x). \end{aligned} \tag{C-7}$$

After integrating the second order term in Equation (2.49), we get

$$\begin{aligned} & -I\phi_{tc}\left(\sigma_{\parallel}^{t}-\sigma_{\perp}^{t}\right)\iint n_t(\vec{\Omega})cos^2\theta P_m(\cos\theta)d\Omega \\ = \; & -I\phi_{tc}(\sigma_{\parallel}^{t}-\sigma_{\perp}^{t})\left[\frac{m(m-1)}{(2m+1)(2m-1)}T_{m-2}\right. \\ & +\left\{\frac{(m+1)^2}{(2m+3)(2m+1)}+\frac{m^2}{(2m+1)(2m-1)}\right\}T_m \\ & \left.+\frac{(m+1)(m+2)}{(2m+1)(2m+3)}T_{m+2}\right] \\ = \; & -I\phi_{tc}(\sigma_{\parallel}^{t}-\sigma_{\perp}^{t})\left[\frac{m(m-1)}{(2m+1)(2m-1)}T_{m-2}\right. \\ & +\left\{\frac{2m^2+2m-1}{(2m-1)(2m+3)}\right\}T_m \\ & \left.+\frac{(m+1)(m+2)}{(2m+1)(2m+3)}T_{m+2}\right] \\ = \; & -I\phi_{tc}(\sigma_{\parallel}^{t}-\sigma_{\perp}^{t})(\kappa_{n-}T_{m-2}+\kappa_nT_m+\kappa_{n+}T_{m+2}), \end{aligned} \tag{C-8}$$

where we have used the conventional notation κ_{n-}, κ_n, and κ_{n+} defined in Equation (2.53).

We denote the anisotropic and the isotropic absorption cross sections,

$$r^{t,c}=\frac{\sigma_{\parallel}^{t,c}-\sigma_{\perp}^{t,c}}{\sigma_{\parallel}^{t,c}+2\sigma_{\perp}^{t,c}}, \quad \bar{\sigma}^{t,c}=\frac{\sigma_{\parallel}^{t,c}+2\sigma_{\perp}^{t,c}}{3}, \tag{C-9}$$

respectively. We can rewrite Equation (C-9) in terms of $\sigma_{\parallel}^{t,c}$ and $\sigma_{\perp}^{t,c}$ as,

$$\sigma_{\parallel}^{t,c} - \sigma_{\perp}^{t,c} = 3\bar{\sigma}^{t,c} r^{t,c}, \quad \sigma_{\perp}^{t,c} = \bar{\sigma}^{t,c}(1 - r^{t,c}). \tag{C-10}$$

Finally, We can add Equation (C-6) and Equation (C-8) together, which leads to the photo-depletion terms as following:

$$\begin{aligned}
& -I\phi_{tc} \iint \left[\sigma_{\perp}^{t} + \left(\sigma_{\parallel}^{t} - \sigma_{\perp}^{t}\right) cos^2\theta\right] n_t\left(\vec{\Omega}\right) P_m(\cos\theta) d\Omega \\
= \; & -I\phi_{tc}\sigma_{\perp}^{t} T_m - I\phi_{tc}(\sigma_{\parallel}^{t} - \sigma_{\perp}^{t})(\kappa_{m-} T_{m-2} + \kappa_m T_m + \kappa_{m+} T_{m+2}) \\
= \; & -I\phi_{tc}\bar{\sigma}^{t}\left[(1 - r^t + 3\kappa_n r^t) T_m + 3r^t \kappa_{m-} T_{m-2} + 3r^t \kappa_{m+} T_{m+2}\right] \\
= \; & -I_t\left[\left\{1 + r^t(3\kappa_m - 1)\right\} T_m + 3r^t \kappa_{m-} T_{m-2} + 3r^t \kappa_{m+} T_{m+2}\right] \\
= \; & -I_t\left\{T\right\},
\end{aligned} \tag{C-11}$$

where $I_t = I\phi_{tc}\bar{\sigma}^t$. In the similar manner, we can rewrite the second term and the third term of Equation (2.49)

$$\begin{aligned}
& \left[I\phi_{ct} \iint n_c\left(\vec{\Omega}'\right)\left\{\sigma_{\perp}^{c} + \left(\sigma_{\parallel}^{c} - \sigma_{\perp}^{c}\right) cos^2\theta'\right\} P^{ct}\left(\vec{\Omega}' \rightarrow \vec{\Omega}\right) d\Omega' \right. \\
& \left. + \frac{1}{\tau_c} \iint Q\left(\vec{\Omega}' \rightarrow \vec{\Omega}\right) n_c\left(\vec{\Omega}'\right) d\Omega' \right] P_m(\cos\theta) d\Omega \\
= \; & I_c P_m^{ct}\{C\} + \gamma C_m Q_m,
\end{aligned} \tag{C-12}$$

where $I_c = I\phi_{ct}\bar{\sigma}^c$ and $\gamma = 1/\tau_c$. Note that $I_{t,c}$ is the correction term that we have added to generalize Sekkat's theory.[3]

Calculation for angular brownian relaxation

R is rotational operator in spherical coordinates with unit radius given by,

$$\begin{aligned}\mathbf{R} &= \hat{r} \times \nabla \\ &= \hat{r} \times \left(\hat{r}\frac{\partial}{\partial r} + \hat{\theta}\frac{1}{r}\frac{\partial}{\partial \theta} + \hat{\phi}\frac{1}{r\sin\theta}\frac{\partial}{\partial \phi} \right) \Bigg|_{r=1}.\end{aligned} \tag{C-13}$$

Since $n_t(\vec{\Omega})$ is independent of ϕ due to azimuthal symmetry, we ignore ϕ. Using the chain rule on the last term yields,

$$\begin{aligned}D_t\mathbf{R}\cdot\mathbf{R}n_t(\Omega) &= D_t\frac{\partial^2}{\partial\theta^2}n_t(\Omega) \\ &= D_t\left(-\cos\theta\frac{\partial}{\partial\cos\theta} + \sin^2\theta\frac{\partial^2}{\partial\cos\theta^2}\right)n_t(\Omega),\end{aligned} \tag{C-14}$$

where we have used the chain rule as follows:

$$\frac{\partial}{\partial\theta} = \frac{\cos\theta}{\partial\theta}\frac{\partial}{\partial\cos\theta} = -\sin\theta\frac{\partial}{\partial\cos\theta} \tag{C-15}$$

and thus

$$\begin{aligned}\frac{\partial^2}{\partial\theta^2} &= -\sin\theta\frac{\partial\left(-\sin\theta\right)}{\partial\cos\theta}\frac{\partial}{\partial\cos\theta} + \sin^2\theta\frac{\partial^2}{\left(\partial\cos\theta\right)^2} \\ &= -\cos\theta\frac{\partial}{\partial\cos\theta} + \sin^2\theta\frac{\partial^2}{\left(\partial\cos\theta\right)^2}.\end{aligned} \tag{C-16}$$

The last term of Equation (2.49) requires the recursion relation,

$$\frac{d}{dx}\left[(x^2-1)\frac{dP_n(x)}{dx}\right] = n(n+1)P_n. \tag{C-17}$$

By substituting $\cos\theta$ into x, we get

$$\begin{aligned}\frac{d}{d\cos\theta}\left[-\sin^2\theta\frac{dP_n}{d\cos\theta}\right] &= 2\cos\theta\frac{d}{d\cos\theta}-\sin^2\theta\frac{d^2}{(d\cos\theta)^2}\\ &= n(n+1)P_n. \end{aligned} \tag{C-18}$$

After using Equation (C-18), we can rewrite Equation (C-14) as

$$D_t\mathbf{R}\cdot\mathbf{R}n_t(\vec{\Omega}) = \frac{D_t}{2\pi}\sum_{n=0}^{\infty}\frac{2n+1}{2}\left(\cos\theta\frac{dP_n}{d(\cos\theta)}-n(n+1)P_n\right)T_n. \tag{C-19}$$

As we did with previous terms, integrating Equation (C-19) over $d\Omega$ after multiplying $P_m(\cos\theta)$ yields

$$\begin{aligned}\iint D_t\mathbf{R}\cdot\mathbf{R}n_t(\vec{\Omega})P_m(\cos\theta)d\Omega &= \frac{D_t}{2\pi}\iint\sum_{n=0}^{\infty}\frac{2n+1}{2}\left(\cos\theta\frac{dP_n(\cos\theta)}{d(\cos\theta)}\right.\\ &\quad \left.-n(n+1)P_n(\cos\theta)\right)T_nP_m(\cos\theta)d\Omega\\ &= -m(m+1)D_tT_m. \end{aligned} \tag{C-20}$$

The configuration of cis-isomer is symmetric to that of trans-isomer. Finally, by combining all terms, Equation (C-11), (C-12), and (C-20), we have calculated, we have Equations (2.51) and (2.52).

Estimation of parameters

In this section, we find the DR1 dye parameters by geometric means. As we have considered DR1 molecules to be cigar shaped, use this fact to relate the cross sections to each other. The angle between the principle axis of trans and cis-isomes are measured to 56.7°.[3] By using the assumption that the angle between the principle axes of trans and cis molecules is

defined by the angle that the azo bond makes with the principle axis of trans-isomer, we get

$$\begin{aligned} L_c &= L_t \cos\theta \\ &= 0.55 L_t. \end{aligned} \tag{C-21}$$

To estimate the relationship of widths between trans and cis molecules, we assume that we can divide the width of the trans molecule by three, such as $W_t = 3a$, where a is the half size of the benzene ring. By using a, we can estimate W_c as follow:

$$\begin{aligned} W_c &\simeq 2a + \frac{a}{\cos\theta} \\ &\simeq 3.8a \simeq 1.27 W_t. \end{aligned} \tag{C-22}$$

The isotropic absorption cross section and the molecule anisotropy we have defined in the previous section are given by

$$\bar{\sigma}^{t,c} = \frac{\sigma_{\parallel}^{t,c} + 2\sigma_{\perp}^{t,c}}{3} \tag{C-23}$$

and

$$r^{t,c} = \frac{\sigma_{\parallel}^{t,c} - \sigma_{\perp}^{t,c}}{\sigma_{\parallel}^{t,c} + 2\sigma_{\perp}^{t,c}}. \tag{C-24}$$

By substituting the parameters we have found from Figure 2.23 and using the assumption that the length of the trans molecule is three times larger than its width, that is $L_t = 3W_t$, we get

$$r^t = \frac{2}{5}, \quad r^c = \frac{1}{13}, \quad \text{and} \quad \frac{\bar{\sigma}^c}{\bar{\sigma}^t} = 0.86. \tag{C-25}$$

The Einstein relation for rod-like molecules is given by[7]

$$D = \frac{k_B T}{\zeta} = \frac{4 k_B T}{\pi \eta_s L^3}. \tag{C-26}$$

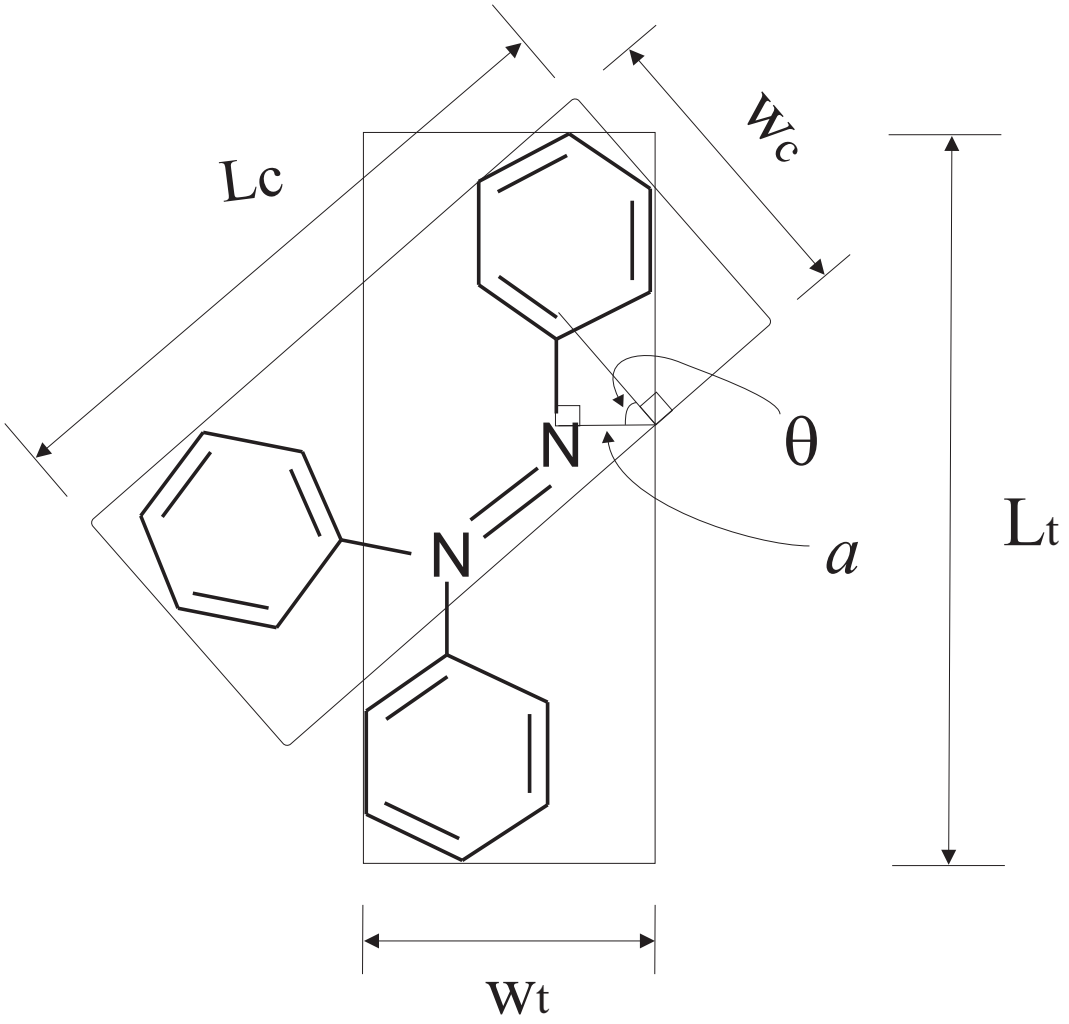

Figure 2.23: Geometric analysis to estimate relative cross section between trans and cis isomer.

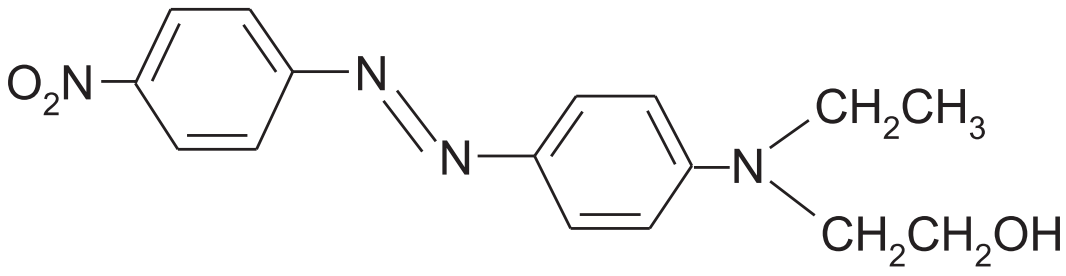

Figure 2.24: The molecular structure of disperse red 1.

By using the ratio between length and width of trans isomers that we have assumed, we get

$$D_c \simeq 6D_t. \tag{C-27}$$

Calculation of the cross section of DR1 trans isomer

We assume that, in the low intensity limit (*i.e.* less than $\mu W/cm^2$), photo-isomerization can be ignored. We have measured the linear absorption coefficient of DR1 in the low intensity region to be $5.63cm^{-1}$. By using the absorption coefficient, we can calculate the cross section of the tran-isomer.

We use a sample of DR1 (2% wt.) doped PMMA. To make the sample at this concentration, we can calculate the weight of DR1 molecules in $1ml$ of MMA to be $0.019g$. The molecular weight of DR1 is $314.34g$. The molecular number density, N, is given by

$$N = \frac{\text{mass of molecule per volume}}{\text{molecular weight}} \times N_A = 3.64 \times 10^{19} cm^{-3}, \tag{C-28}$$

where N_A is Avogadro number, 6.022×10^{23}. The cross section, $\bar{\sigma}^t$, is given by

$$\bar{\sigma}^t = \frac{\alpha}{N}. \tag{C-29}$$

Equation (C-29), with values of $\lambda = 633nm$ and $\alpha = 5.06cm^{-1}$, $\lambda = 647nm$ and $\alpha = 5.63cm^{-1}$, gives $\bar{\sigma}^t = 1.39 \times 10^{-19} cm^2$ and $\bar{\sigma}^t = 1.55 \times 10^{-19} cm^2$, respectively.

Calculation of the parameter I_t and I_c

In this section, we calculate the number of photons absorbed per unit time including the isotropic cross section of the trans isomer, which we have found in the previous section. The number of photons that arrive per unit time per unit area for a peak intensity, I_p (W/cm^2), when $\lambda = 647nm$ is given by

$$I = \frac{I_p}{E_{ph}} = 3.26 I_p \times 10^{18} cm^{-2} s^{-1}, \tag{C-30}$$

where E_{ph} is the energy of one photon. As we have defined I_t in Equation (C-11), $I_t = I\bar{\sigma}^t\phi_{tc}$. By substituting $\bar{\sigma}^t$ in previous section, we get $I_t = 0.51\phi_{tc}I_p$. In a similar manner, we can easily find $I_c = 0.43\phi_{ct}I_p$ by using the relationship between $\bar{\sigma}^t$ and $\bar{\sigma}^c$ in Equation (C-25).

Calculation of the length and width of DR1 molecule

Table 2.1 shows the DR1 molecule's bond lengths. As we see in Figure 2.24, we can find the length of the molecule by adding all the bond lengths along the molecule while considering the pyramid shape of the bonding angle in nitrogen, which is 109° (half of this angle is the angle between the long axis and the $N-C$ bond) and the tilt angle of the azo bond is 56.7°. The length of the trans isomer is given by

$$\begin{aligned} L_t &= L_{O-N}\cos 54.5^\circ + 4L_{C-N} + L_{N=N}\cos 56.7^\circ \\ &\quad +2W_{Benzene} + \cos 54.5^\circ \left(L_{N-C} + L_{C-O} + L_{O-H}\right) + L_{C-C} \\ &= 22.38\mathring{A}. \end{aligned} \tag{C-31}$$

We assume that the benzene hexagone is the main part of the width of trans isomer of DR1, which give us $W_t = 5.6\mathring{A} \simeq 1/5L_t$.

Bonding type	O – N	N = N	C – N	C – C	C – H	Benzene hexagone
Bonding length (pm)	145	124	147	154	109	560

Table 2.1: Bond lengths for DR1 molecules.

2.8.4 Appendix D: Mathmatica code

```
en:=1(*1 for linear -1/2 for circular*)
alp:=0.000237 (*alp the absorption is calculated from n_DR1 value set to be \
0.001*)
n0:=1.49
rt:=2/5
rc:=1/13
a:=2/5 it kt(*at in equation T2*)
b:=2/5 ic kc (*ac in equation C2*)
c:=1+4/7 en rt (*where en is e in equation T2*)
f:= 1+4/7 en rc (*where en is e in equation C2*)
ra:=6(*diffusion constant ratio between cis and trans,
  Theoretically length of the long axis of cis and trans are found. dc=
    ra dt, ra=6*)
it:=0.011(*I_t in equation T2,
  This intensity change is critical so we should use low intensity*)
ic:=0.00946(*I_c in equation C2, same here low intensity,
  and when ic is larger than it, (*it looks same trendy in very low \
temperature. Q: high temperature cis is sensitive?*)*)
kt:=en rt (*in equation T2*)
kc:=en rc  (*in equation C2*)
l0:=it  (1 + 4/5 (en rt)^2 + 4/7 en rt +
          6 d/it)/(2  (1 + 2/7 en rt +
              3 d/it)) (*lambda_0 in equation T0 and C0*)
lt:=it c + 6 d (*lambda_t in equation T2*)
lc:=ic f +
    6 ra d (*lambda_c in equation C2,
        diffusion constant is controlled by a ratio, ra, to D_t*)
p2:=0.98 (*P_2^{tc}*)
T0:=Exp[-l0 x]
C0:=1-T0

d:=0.0001(*D_t in equation T2*)

T2:=a / (lt-l0) ( Exp[-lt x]-Exp[-l0 x])
C2:=a p2  (6 d - lt)/((lt-l0) (lt-lc))(
        Exp[-lt x] -
          Exp[-lc x]) + (b(lt-l0)-
            a p2 (l0 - 6 d))/((lt- l0) (lc-l0)) (Exp[-l0 x] - Exp[-lc x])

n33:=2 Pi alp/n0  (T0 (0.14-2/5 T2 +0.86/13 C2) +0.86 (1-1/13 C2))
n11:=2 Pi alp/n0 (T0 (0.14 +4/5 T2 -2 0.86/13 C2) +0.86 (1+2 0.86/13 C2))

deln33:=n33- 2 Pi alp/n0
deln11:=n11-2 Pi alp/n0

(*At time t=3, plotting refractive indices in function of intensities*)
x:=3
Plot[{deln33,deln11}, {it,0,2}, PlotStyle\[Rule]{Hue[0.7],Hue[1]},
  Frame\[Rule]True,
  TextStyle\[Rule]{FontFamily\[Rule]"Times New Roman",FontSize\[Rule]18}]
Plot[{deln33,deln11}, {it,0,0.05}, PlotStyle\[Rule]{Hue[0.7],Hue[1]},
  Frame\[Rule]True,
  TextStyle\[Rule]{FontFamily\[Rule]"Times New Roman",FontSize\[Rule]18}]
```

```
Plot[{T0,C0},{x,0,50}, PlotStyle\[Rule]{Hue[0.7],Hue[1]},Frame\[Rule]True,
  TextStyle\[Rule]{FontFamily\[Rule]"Times New Roman",FontSize\[Rule]18}]
Plot[{T2,C2},{x,0,50}, PlotStyle\[Rule]{Hue[0.7],Hue[1]},Frame\[Rule]True,
  TextStyle\[Rule]{FontFamily\[Rule]"Times New Roman",FontSize\[Rule]18}]
Plot3D[deln11,{d,0,0.003}, {x,0,50},
  TextStyle\[Rule]{FontFamily\[Rule]"Times New Roman",FontSize\[Rule]18}]
Plot3D[deln33,{d,0,0.003}, {x,0,50},
  TextStyle\[Rule]{FontFamily\[Rule]"Times New Roman",FontSize\[Rule]18}]
Plot[{deln33,deln11}, {x,0,50}, PlotStyle\[Rule]{Hue[0.7],Hue[1]},
  Frame\[Rule]True,
  TextStyle\[Rule]{FontFamily\[Rule]"Times New Roman",FontSize\[Rule]18}]
Plot[n33-n11, {x,0,50}, PlotStyle\[Rule]{Hue[0.7],Hue[1]},Frame\[Rule]True,
  TextStyle\[Rule]{FontFamily\[Rule]"Times New Roman",FontSize\[Rule]18}]
Plot3D[n33-n11, {d,0,0.003},{x,0,50},
  TextStyle\[Rule]{FontFamily\[Rule]"Times New Roman",FontSize\[Rule]18}]
```

Bibliography

[1] S. A. Akhmanov, A. P. Sukhorukov, and R. V. Khokhlov, "Self-focusing and diffraction of light in a nonlinear medium," Uspekhi **93**, 609 (1968).

[2] S. A. Akhmanov, A. P. Sukhorukov, and R. V. Khokhlov, "Self-focusing and self-trapping of intense light beams in a nonlinear medium," Sov. Phys.–JETP **23**, 1025 (1966).

[3] Z. Sekkat, J. Wood, and W. Knoll, "Creation of second-order nonlinear optical effects by photoisomerization of polar azo dyes in polymeric films: theoretical study of steady-state and trasient properties," J. Opt. Soc. Am. B **95**, 1855 (1995).

[4] S. A. Akhmanov, D. Krindach, A. V. Migulin, A. Sukhorukov, and R. V. Khokhlov, "Thermal self-actions of laser beams," IEEE J. Quantum Electron. **4**, 568 (1968).

[5] H. S. Carslaw and J. C. Jaeger, *Operational methods in applied mathematics* (Dover Publication, Inc., New York, 1963).

[6] Z. Sekkat, J. Wood, and W. Knoll, "Reorientation mechanism of azobenzenes within the Trans ⇒ Cis photoisomerization," J. Phys. Chem. **99**, 17 226 (1995).

[7] M. Doi and S. F. Edwards, *The theory of polymer dynamics* (Oxford University Press, New York, 1986).

[8] M. G. Kuzyk, K. D. Singer, H. E. Zahn, and L. A. King, "Second-order nonlinear-optical tensor properties of poled films under stress," J. Opt. Soc. Am. B **6**, 742 (1989).

Chapter 3

Experiment

3.1 Introduction

In this chapter, we begin by introducing the procedure of making dye doped poly-methyl methacrylate (PMMA) bulk samples of high optical quality. We use a recipe developed in our lab for making a preform (which is a cylinder form which a fiber is drawn), which is amenable to squeezing at high temperature to form the polymer into desired shape. Because the length of nonlinear material determines the magnitude of the change of the beam diameter, we make samples of about 1 mm.

To characterize the materials; we extend the well-known Z-scan technique to time-resolved Z-scan using a continuous wave light source instead of the traditionally-used pulse laser. We reduce the amount of hysterises in the dye-doped polymer sample in the closed-aperture transmittance experiments by only exposing a particular point in the sample for a limited amount of time, we can, thus, determine the relative contribution of the slow mechanisms, such as the intensity-dependent refractive index due to photothermal heating and molecular reorientation due to photo-isomerization. To isolate the thermal mechanism, we discuss a temperature-dependent optical Kerr gate experiment that is performed to measure thermal agitation independently of the photothermal heating.

3.2 Sample fabrication

3.2.1 Preform preparation

We make our preform with mixture of MMA(Methyl Methacrylate) which turns into polymer after polymerization, Chain Transfer Agent(CTA;1-Butanethiol) which limits the chain length of the polymer, and initiator(tert-Butyl peroxide) which is a catalyst that starts the polymerization reaction. MMA needs to be filtered by an alumina packed column so that we eliminate the inhibitor that is added to commercial MMA to prevent polymerization during shipment and storage. After extracting the inhibitor, MMA can be polymerized by room light. To prevent filtered MMA from polymerization, the container needs to be wrapped with aluminium foil. We use the optimized ratio of $2.2\mu l$ of CTA and initiator per $1ml$ of MMA, which provides a balance between short chain length and brittleness.

The amount of CTA is adjusted to compensate for the added dyes, which also act as a CTA. We have found that some dyes can make the polymer lengths so short that the polymer becomes too brittle for further processions. When initiator is added to MMA, polymerization starts by the addition of heat and/or light. Therefore, the dye must be added to the MMA prior to the initiator.

Placing the MMA and dye into an ultrasonic bath is the most efficient means for ensuring that the dye dissolves in the liquid monomer. However, a magnetic stir bar works well to help PMMA polymer to dissolve in a solvent. Since the ultra-sonic bath adds energy to the solution in the form of heat, cause must be exercised to ensure that polymerization does not result. After the dye molecules are dissolved in MMA, we add $2.2\mu l$ of CTA and initiator by using a micro-pipet. To prevent inhomogeneity in the liquid sample, we place the sample bottle in the ultra-sonic bath for about 5 minutes. This process is critical to eliminate small-sized bubbles in the liquid monomer.

After preparation of the dye/MMA solution, we transfer the liquid to a clean test tube that is placed in an oven for polymerization. To reduce any possible pre-polymerized clusters

or any undissolved residue of dye molecules or dust, we pass the solution through a disk syringe filter (0.2 μm GHP ACRODISC). The capacity of the syringe can be varied by the concentration of dye molecules. For 2 wt % DR1 (Disperse Red 1), one disk filter can be used to fill one and 2/3 test tubes, a volume of amount $30ml$.

The liquid solution in the test tube is placed in an oven. We set the oven temperature to 85°C and keep the sample in the oven until it is fully polymerized. When large volumes of MMA are polymerized, the temperature of the oven is lowered to avoid explosion of the monomer. Typical polymerization times are about 2-3 days, but we can offer add an extra day to complete sure full polymerization.

When polymerization is complete, the test tube is transferred to a freezer so that the polymer separates from the test tube by differential expansion. After 3-4 hours of cooling, we take the test tube out of the freezer and break the glass tube to remove the rod-shaped sample.

3.2.2 Sample polishing

The rod sample, made as described in Section 3.2.1, is too large in volume to squeeze down to a thickness of 1 mm. Therefore, we cut the rod sample into short-length cylinders. Among the cutting methods, lathing makes the cut surface clean compared to sawing. Since we are squeezing the rod shape into a flat shape, all sides need to be as smooth to the level of optical quality.

For the first polishing process, we use various kinds of sandpapers including P150, P320, and P600. For the finest one, P600, we apply water to the sandpaper. Once we get a flat opaque surface, we use lapping film as the second process with water to get optical quality. To do so use a polishing pad, CTG913, from Thorlabs. After cleaning the glass plate, we apply water to secure the contact between the lapping paper ($5\mu m$) and the glass plate. The interface between the glass plate and the lapping paper is critical to avoid fine scratches in the process of polishing. We polish the sample using a figure 8 pattern. The last process

of polishing is done with an optical cloth by applying alumina polishing suspension diluted in water. Both cut sides of the sample need of optical quality. This polishing process often takes for several hours.

3.2.3 Squeezed bulk sample

Once we have a sample with an optical quality surfaced, we squeeze it by using a squeezer as shown in Figure 3.1. We prepare the surfaces of glass plates by cleaning them with ethanol as an usual method to clean lenses. It is important to center the rod between the glass plates. Before the temperature is ramped up, the rod sample is squeezed by the screw enough to hold it in place at the center.

We set the temperature of the oven to 115 to 120°C. When the sample is heated for about 30 minutes, it is soft enough that the thickness of the sample decreases without further tightening of the screw. We tighten the screw again enough to hold the sample flat and place it in the oven. The sample is squeezed every 10 to 15 minutes by the screw, while keeping the glass plates parallel to each other, a thickness of $1mm$ is reached. Subsequently, the sample is kept in the oven for about 20 to 30 minutes at a lower temperature around 95°C so that the polymer can relax. The relaxation time and temperature are critical because it avoids bubbles, that normally form at the squeezing temperature. The sample is separated from the glass plates after allowing the squeezer to cool to ambient over night. Figure 3.2 shows the initial and final shapes of the sample. The spacers are to keep the gap between the glass plates constant through out the sample.

3.3 Z-scan

3.3.1 Z-scan theory

In 1990, Sheik-Bahae et al.[1] developed a sensitive self-(de)focusing measurement technique, Z-scan, that involves focusing a laser beam through a thin sample and detecting the light

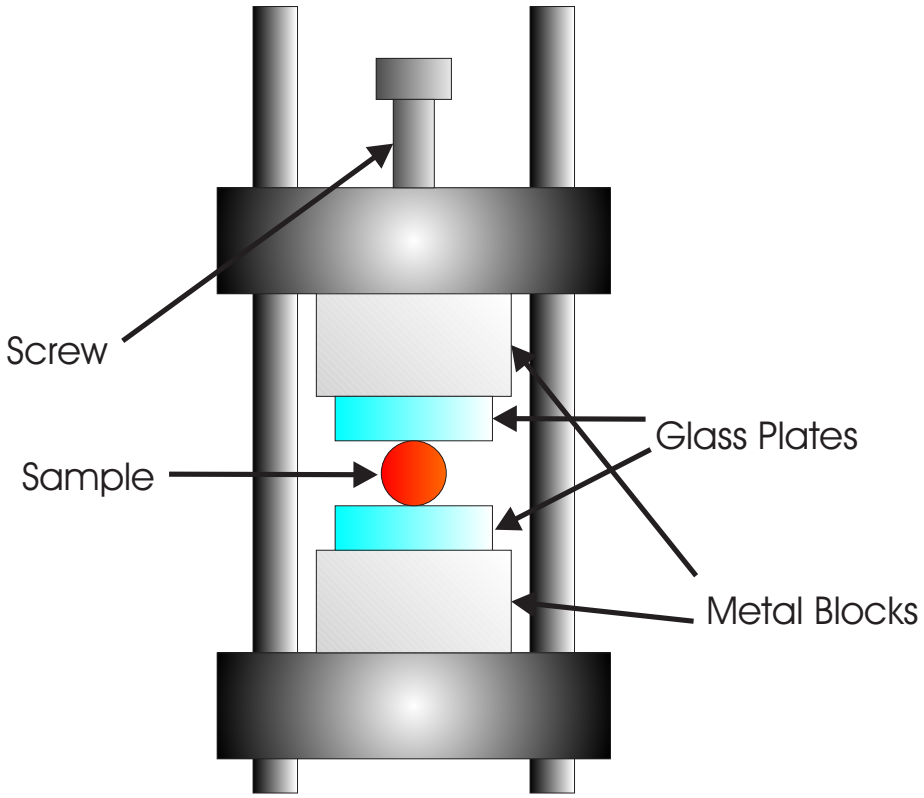

Figure 3.1: Squeezer used to compress a the sample.

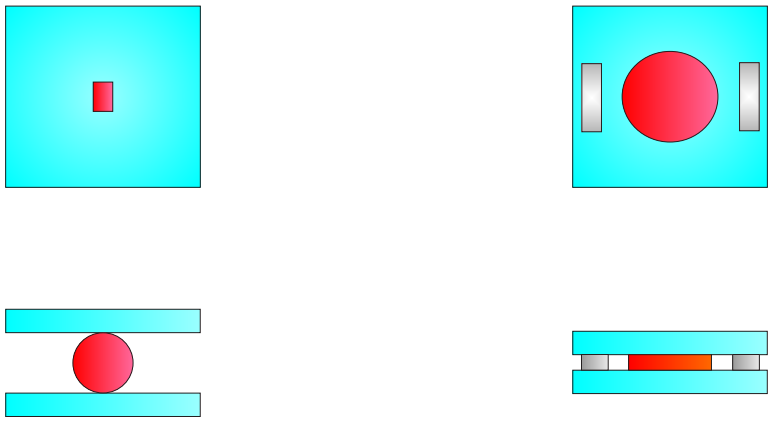

Figure 3.2: The procedure of squeezing the sample as observed from the top and side views. (a) The initial shape and size of the sample, (b) The final shape and size of the squeezed sample. The spacers are placed between the glass plates to keep them parallel.

transmitted by a small aperture in the far field to measure the nonlinear refractive index.

The theory is developed assuming a TEM_{00} Gaussian beam propagating in the z-direction with a beam waist, w_0, such that

$$E(z,r,t) = E_0(t)\frac{w_0}{w(z)}\exp\left[-\frac{r^2}{w^2(z)} - \frac{ikr^2}{2R(z)}\right]e^{-i\phi(z,t)}, \tag{3.1}$$

where $w^2(z) = w_0^2(1 + z^2/z_0^2)$ is the beam radius, $R(z) = z(1 + z_0^2/z^2)$ is the radius of curvature of the wave front at z, $z_0 = kw_0^2/2$ is the Rayleigh length, $k = 2\pi/\lambda$ is the wave number, and λ is the wavelength. Under the condition that the sample length is small enough, changes in the beam diameter within the sample due to diffraction or nonlinear refraction can be neglected. Note that in our experiment the thickness of the sample is not thin enough to neglect changes in beam diameter due to self-(de)focusing. Therefore, we need to consider the beam diameter as a separate parameter. The thickness of our sample, however, is small compared to the Rayleigh length ($L < z_0$), but not small compared to the nonlinear refraction length.

Using the Gaussian decomposition method,[2] the electric field at the aperture is given by[1]

$$E(r,t) = E(z, r=0, t)e^{-\alpha L/2} \sum_{m=0}^{\infty} \frac{[i\Delta\phi_0(z,t)]^m}{m!} \frac{w_{m0}}{w_m} \exp\left[-\frac{r^2}{w_m^2} - \frac{ikr^2}{2R_m} + i\theta_m\right], \tag{3.2}$$

where

$$\begin{aligned} w_{m0}^2 &= \frac{w^2(z)}{2m+1} \\ d_m &= \frac{kw_{m0}^2}{2} \\ w_m^2 &= w_{m0}^2\left[g^2 + \frac{d^2}{d_m^2}\right] \\ R_m &= d\left[1 - \frac{g}{g^2 + d^2/d_m^2}\right]^{-1} \end{aligned}$$

and

$$\theta_m = \tan^{-1}\left[\frac{d/d_m}{g}\right]. \tag{3.3}$$

The transmitted power through aperture is given by

$$P_T(\Delta\Phi_0(t)) = c\epsilon_0 n_0 \pi \int_0^{r_a} |E_a(r,t)|^2 r dr, \tag{3.4}$$

where r_a is the radius of the aperture. The time-averaged normalized transmittance over a laser pulse is

$$T(z) = \frac{\int_{-\infty}^{\infty} P_T(\Delta\Phi_0(t))dt}{S\int_{-\infty}^{\infty} P_i(t)dt}, \tag{3.5}$$

where $P_i(t) = \pi w_0^2 I_0(t)/2$, the instantaneous input power within the sample and $S = 1 - \exp(-2r_a^2/w_a^2)$, the linear transmittance through the aperture.

For a CW laser, the input power is constant in time. The normalized transmittance can be obtained by taking the ratio of the transmitted power with nonlinear refraction to the

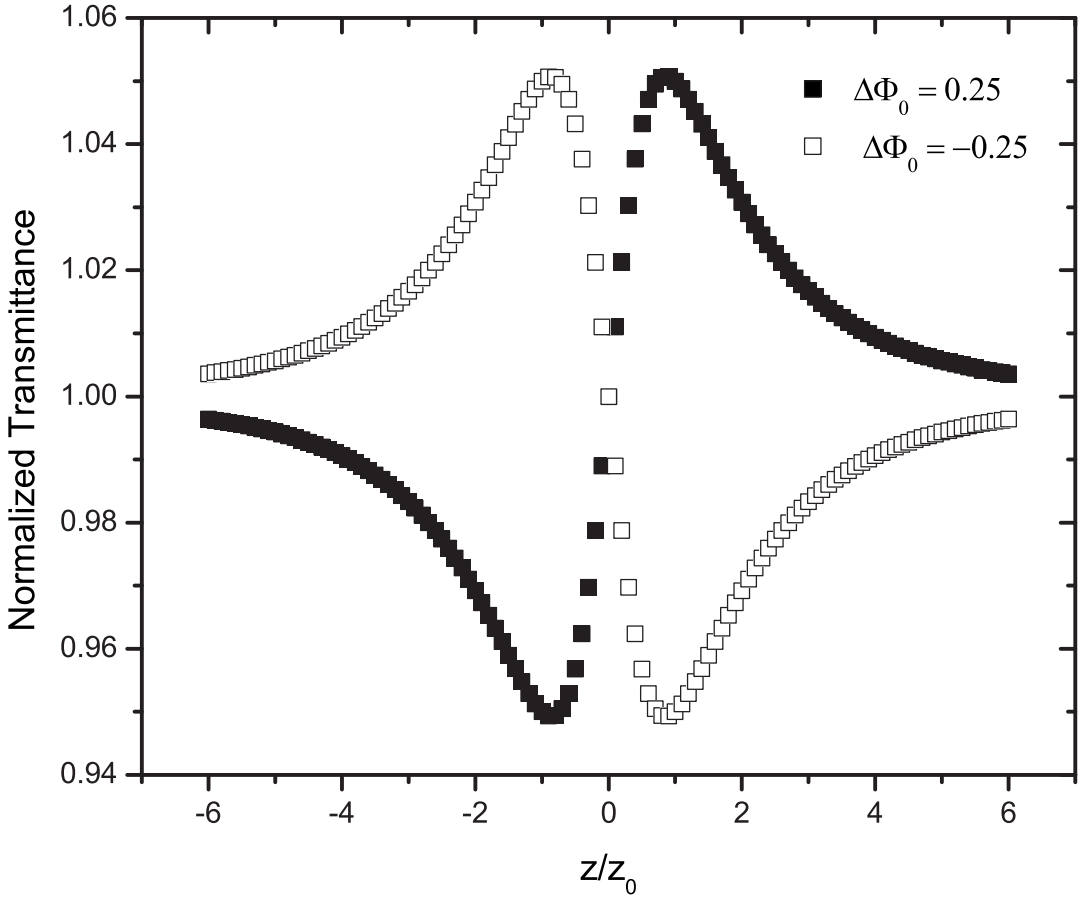

Figure 3.3: Normalized transmittance when $\Delta\Phi_0 = \pm 0.25$ and $S = 0$, which is an ideal case for on-axis. It is easy to judge whether the refractive index is positive or negative from the shape of the curve.

initial transmitted power:

$$\begin{aligned} T(z,t) &= \frac{P_T(\Delta\Phi_0(t))}{P_i S} \\ &= \frac{P_T(\Delta\Phi_0(t))}{P_T(\Delta\Phi_0(0))}, \end{aligned} \tag{3.6}$$

where $P_T(\Delta\Phi_0(0))$ is the initial transmitted power when the beam is on ($t = 0$) or when $\Delta\Phi_0 = 0$. Equation (3.6) gives us the instantaneous normalized transmittance.

For the on-axis beam ($r = 0$) in the far-field condition ($d \gg z_0$), and in the small nonlinear phase change condition ($|\Delta\Phi_0| \ll 1$), Equation (3.5) can be written as

$$T(z, \Delta\Phi_0) \simeq 1 + \frac{4\Delta\Phi_0 x}{(x^2+9)(x^2+1)}, \tag{3.7}$$

where $x = z/z_0$ and $\Delta\Phi_0 = k\Delta n_0 \frac{[1-\exp(-\alpha L)]}{\alpha}$. Figure 3.3 shows the normalized transmittance as a function of z/z_0. The negative sign of $\Delta\Phi_0$ represents the negative refractive index that leads change to de-focusing. Due to the de-focusing effect, where $z/z_0 < 0$, the converging beam will converge less, and where $z/z_0 > 0$, the diverging beam will diverge more. Therefore, when the sample is placed before the focal point, the normalized transmittance will increase. On the other hand, when the sample is placed after the focal point, the transmittance will be decrease. In our experiment, the sample length is thicker than in the films typically used for Z-scan. Therefore, we need to consider nonlinear refraction in the sample, which leads us to use the beam waist, w_0, as a parameter.

Because we use our laser source in its "light mode", drift in power is small compared to the changes observed due to signal. We must detect the open and closed aperture signal at the same time since sequential measurements suffer from the notorious history effect in DR1-doped polymers. To be able to maintain high correlation between nonlinear absorption and refraction, we must take both data sets simultaneously. The beam splitter downstream from the sample allows both to be measured. A calibration of the detectors need to be

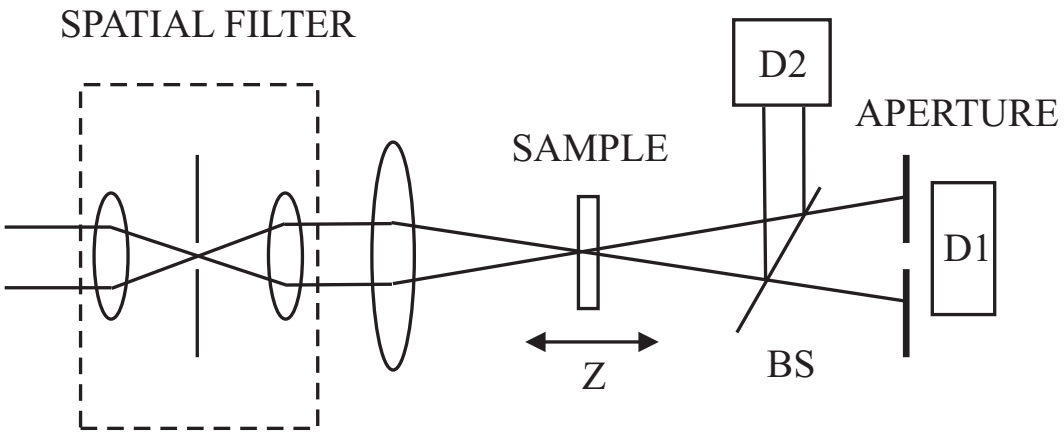

Figure 3.4: Schematic diagram of a Z-scan experiment. BS is beam splitter and D1, D2 are detectors.

performed prior to the data acquisition so that signals can be compared on the same scale. The sensitivity of the two detectors is calibrated by measuring the ratio of their measured voltage as power with the sample removed. After calibrating the detectors, we measure the detected signal ratio, D1/D2 with the sample in place. The initial transmitted power, $P_T(\Delta\Phi_0(0))$, is the ratio (D1/D2) at $t = 0$.

3.3.2 Gaussian beam profile measurement

To be able to use the Z-scan technique, it is important for the beam profile to be gaussian. As we see in Figure 3.4, by using two confocal lenses and a pinhole, we can spatially filter other modes or noise and pass only the TEM_{00} mode. The position of the pinhole is critical to produce a gaussian beam. The pinhole is mounted on a 3-Dimensional translation stage for precise control of the position. By monitoring the quality of the beam profile on a screen, as shown in Figure 3.5, the pinhole can be placed at the focal point. By scanning in the x and y directions, we can find a position where the transmitted power is maximum. For positioning in the z-direction, where the beam intensity varies slowly with position a set of airy fringes is observed for a beam whose diameter is larger than the pinhole. As the beam approaches the center of the pinhole and the center of the focal point, the edge of the beam

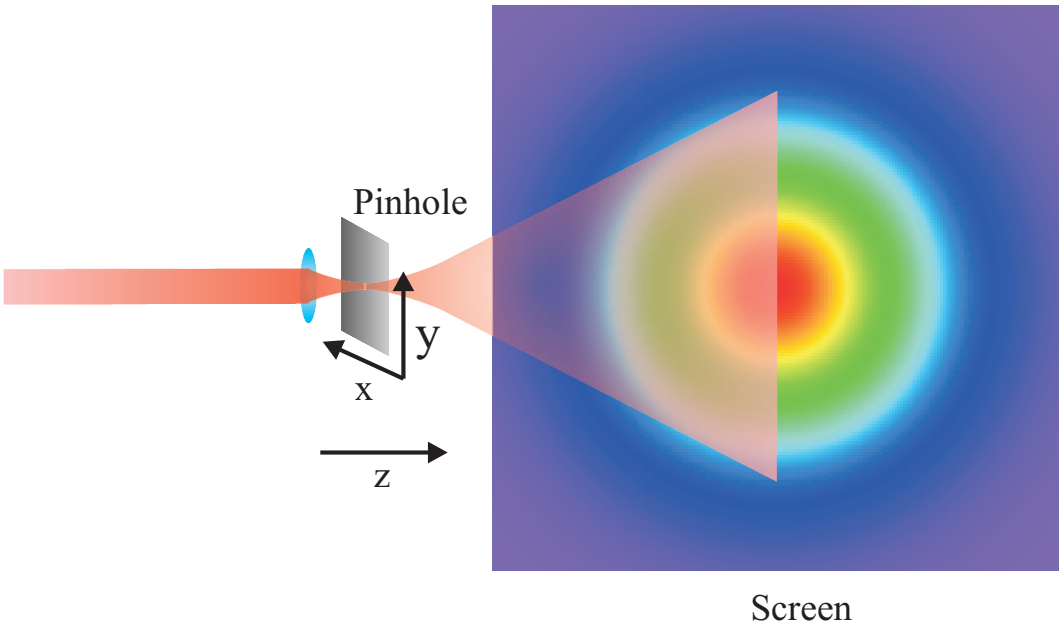

Figure 3.5: Positioning the pinhole to get a gaussian beam.

shape gets smoother. To ensure the best placement of the pinhole, we iteratively scan in $x-y$ and z directions until we get a high quality gaussian beam. Figure 3.5 shows the setup for beam filtering.

For a focused beam, we use the knife edge method to measure the beam profile, as shown in Figure 3.6. We mount a knife on 2-dimensional translation stage controlling x and z variables. At a fixed z position, we measure the transmitted power as a function of x. The transmitted power is normalized to the incident power when the knife edge is not blocking the beam as follows:

$$\begin{aligned} T(x,z) &= \frac{\int_{-\infty}^{\infty}\int_{-\infty}^{x}\exp\left(-\frac{2x'^2}{a^2}\right)\exp\left(-\frac{2y'^2}{a^2}\right)dx'dy'}{\int_{-\infty}^{\infty}\int_{-\infty}^{\infty}\exp\left(-\frac{2x'^2}{a^2}\right)\exp\left(-\frac{2y'^2}{a^2}\right)dx'dy'} \\ &= \frac{1}{2}\left[1+Erf\left(\frac{\sqrt{2}x}{w(z)}\right)\right], \end{aligned} \tag{3.8}$$

where x is the position of the knife edge as shown in Figure 3.7. For example, Figure 3.7

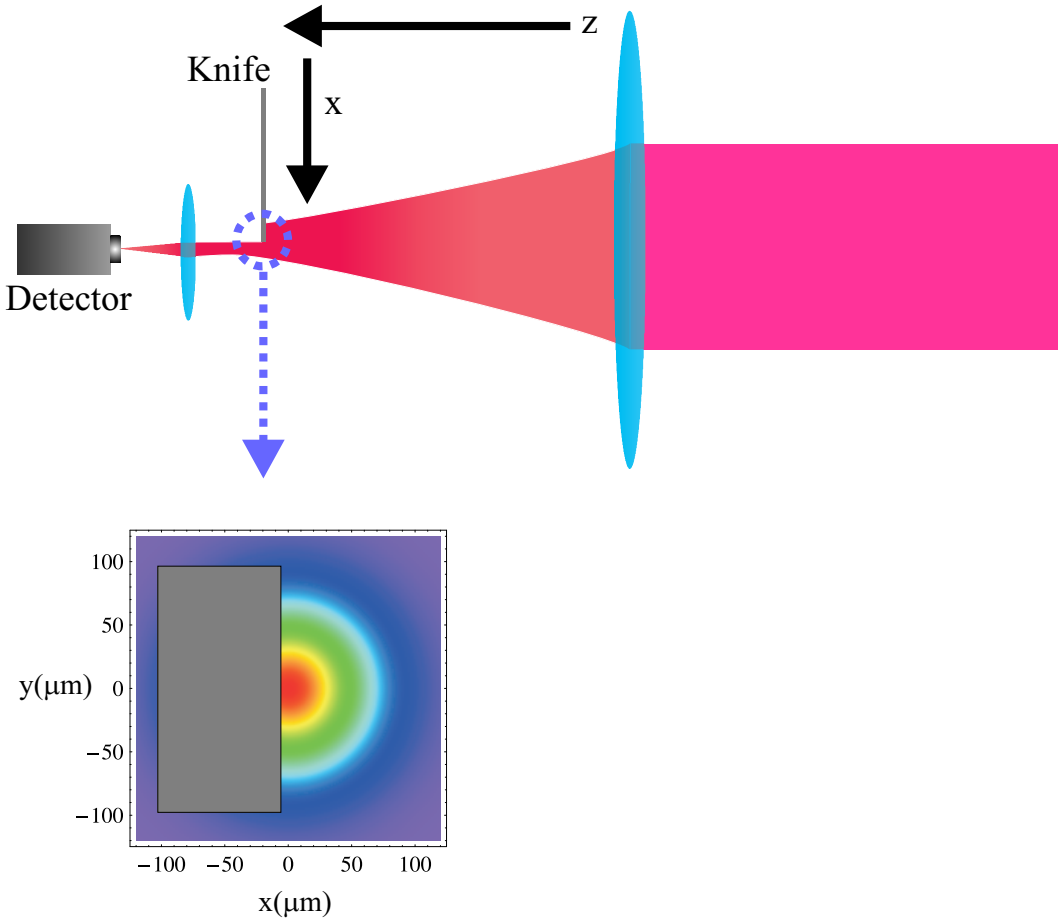

Figure 3.6: Transmittance measured as a function of knife edge position.

shows the normalized transmittance fits to Equation (3.8) for the selected z positions. From this fitting process, we determin $w(z)$.

The uncertainty in $w(z)$ is determined from the uncertainties in the fit parameters that come from a least square fit which is used to determine the error bars in Figure 3.8. Gaussian wave propagation leads to a beam waist of the form:

$$w(z) = w_0 \sqrt{1 + \left(\frac{\lambda z}{\pi w_0^2} \right)^2}. \tag{3.9}$$

Using Equation (3.9) a fit of the data to $w(z)$ leads us to find beam waist, w_0, as shown in Figure 3.8.

3.4 Time-resolved Z-scan by continuous wave

3.4.1 Motivation

Z-scan technique is easy to use for measurement of the nonlinear properties, such as nonlinear absorption and refraction. For time-dependent Z-scan, time delay technique is considered with pulse laser.[3] In CW laser, time-resolved Z-scan is also developed by using various chopper frequencies and Fourier transform.[4][5][6]

For materials that have history effect that lasts for a long time like DR1 in our research, we found there is a problem to scan along z-direction by using pulse laser or chopped beam, due to requirement of a fresh sample area to be a target. To be able to use a fresh part of the sample, it is convenient to measure the transmittance as a function of time in virtue of continuous wave as the light source at various z-positions at a time. By recombining the data as a function of z at a fixed time series, we can find the nonlinear refractive index as a function of time without affecting initial conditions of the sample.

As such, by time-dependent Z-scan technique in CW laser which we will show in this section, we can analyze what the mechanisms are involved and how they are related.

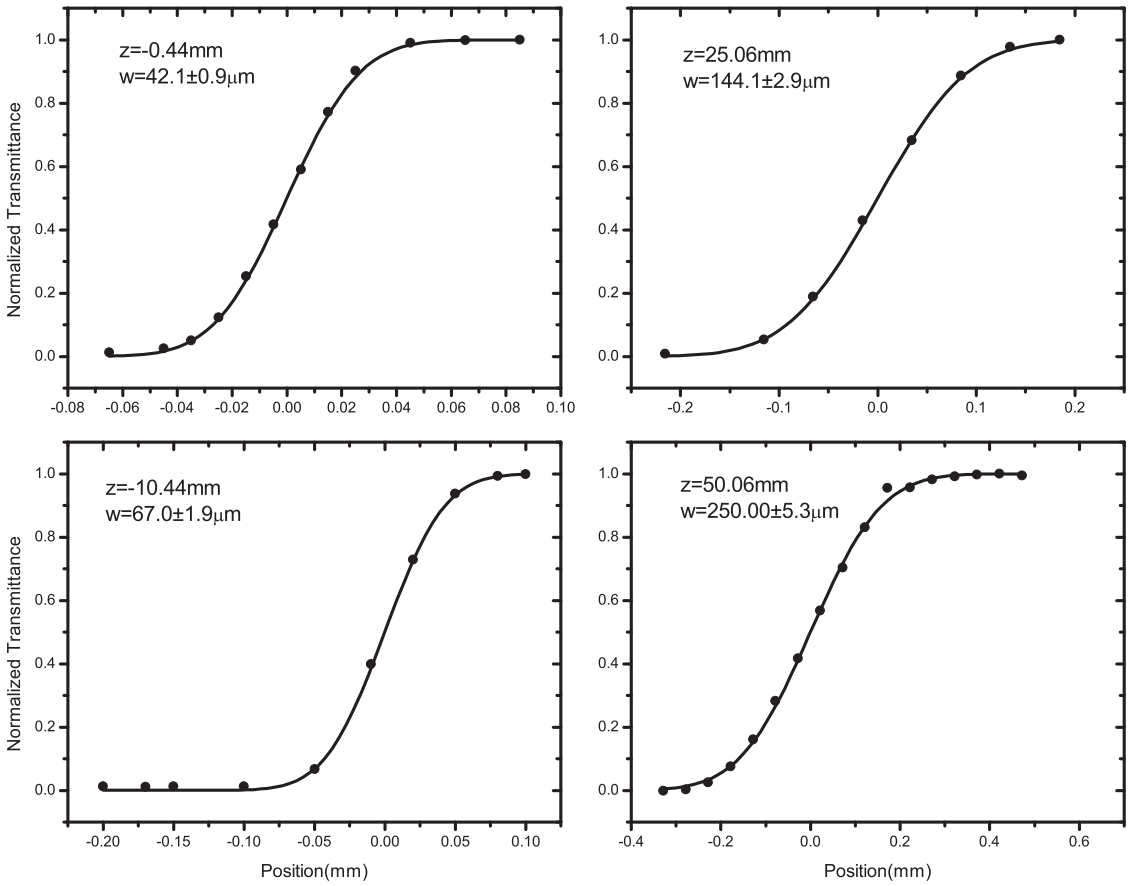

Figure 3.7: Normalized transmittance. Dots (•) are the measured data points. The line (−) is a fit to Equation (3.8). z is the laboratory coordinate, which should be distinguished from the variable "z", which is zero at the focal point.

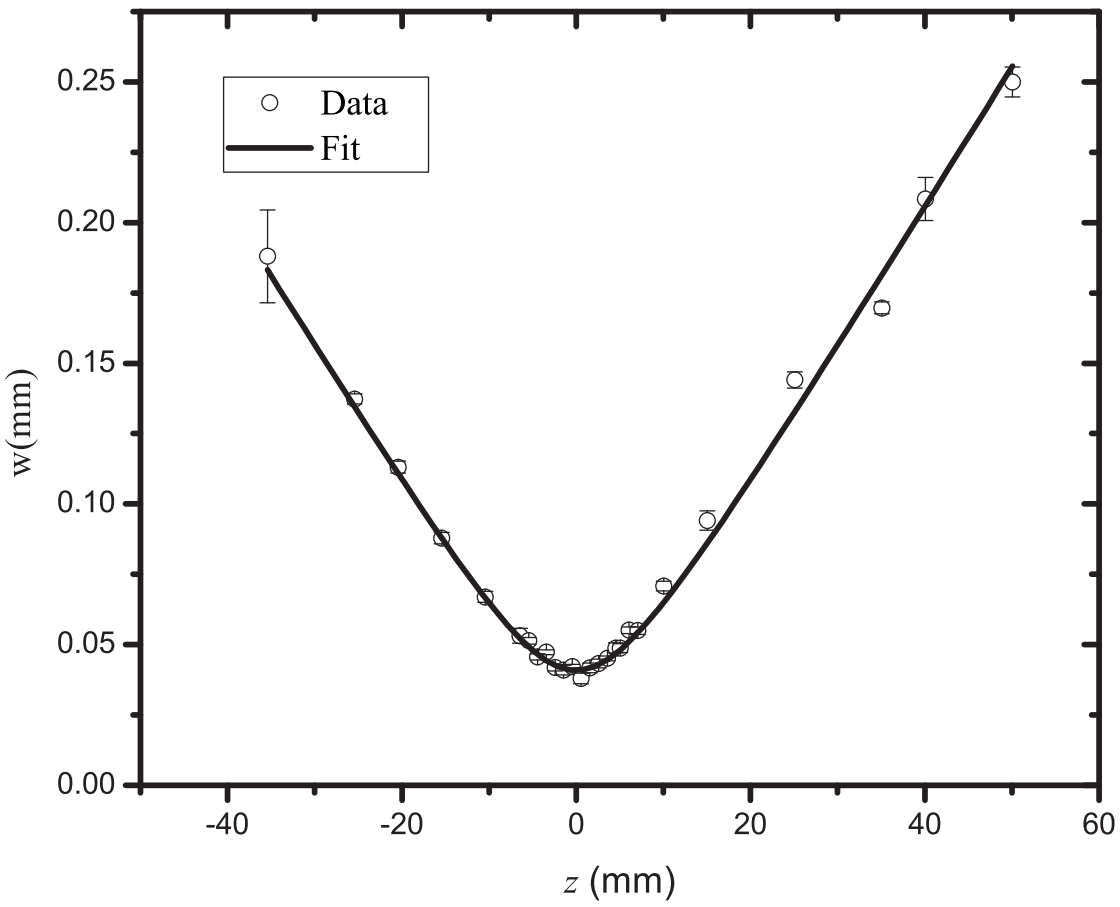

Figure 3.8: The beam waist as a function of z near the focal point. The beam waist, w_0, is determined to be $w_0 = 40.87 \pm 0.43 \mu m$. The circles ($\circ$) are the data and the line (-) is the theory in Equation (3.9). The error bars are obtained from the fitting parameters in Figure 3.7.

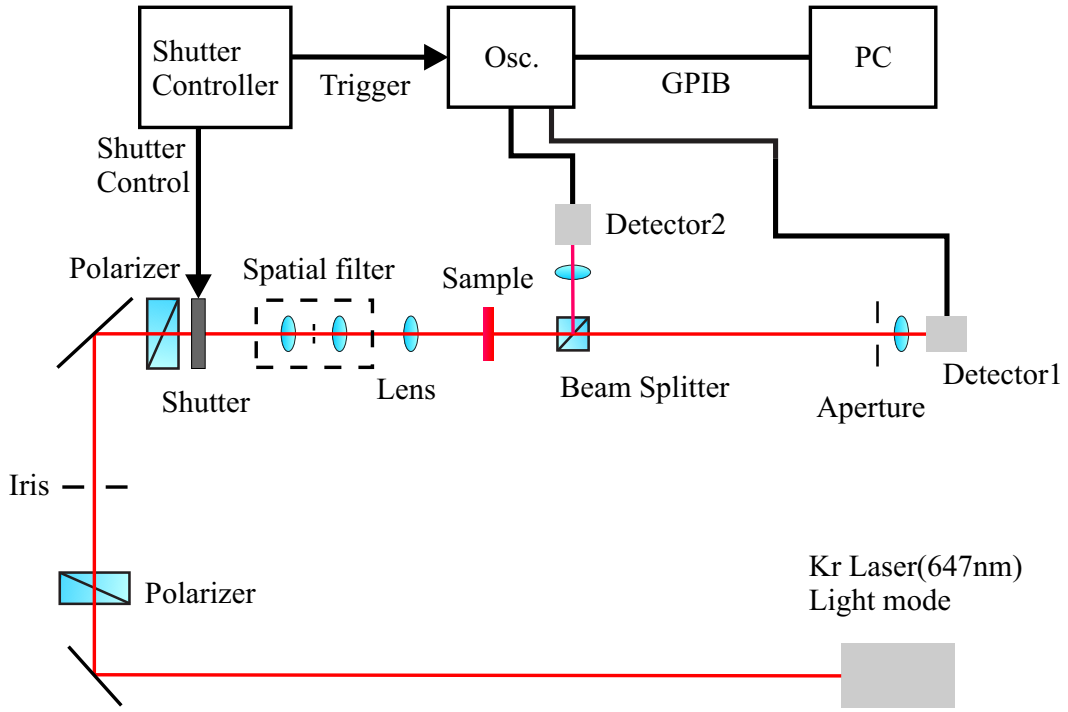

Figure 3.9: Setup for time-resolved single beam Z-scan experiment

3.4.2 Experimental setup

We use a Kr laser (coherent Innova 70C spectrum) at $\lambda = 647nm$ and $\lambda = 457nm$, which are far from the absorption peaks of the DR1 dye (absorption coefficient $\alpha = 5.63cm^{-1}$) and Disperse Blue 14 (DB14; absorption coefficient $\alpha = 1.72cm^{-1}$) samples, respectively. We set the mode of the laser in "light mode" which keeps the power of the laser stable. Figure 3.9 shows the experimental setup for time-dependent Z-scan using a CW laser. The iris is placed well before the sample to block multi-reflected beam spots from the various optical components. The first polarizer passes the dominant laser polarization. The second polarizer selects the desired polarization direction. The shutter is controlled by a VMM-T1 shutter driver/timer, can be set to an arbitrary exposure time and can be triggered by computer. The shutter trigger signal is synchronized for enabling to the external channel of the oscilloscope(LeCroy LT372) in auto mode, signals to be recorded from detector 1 and 2 in real time. As such, the trigger sets the time t = 0 when the shutter is opened. The PC

downloads the data in ASCII format from the oscilloscope through a GPIB cable through Scope Explorer provided by LeCroy. We place the spacial filter near the sample to ensure a gaussian beam profile in the sample, which is mounted on a 2-Dimensional translation stage (x-z directions).

The transmittance is recorded as a function of time after the beam is turned on. Subsequently, the position of the sample is incremented and the sample is moved in the $x-y$ plane to a fresh spot to avoid hystereses. The shutter is opened and the measurement repeated until the sample has been moved from a point well in front and well behind the focal point.

Because we use the "light mode" setting on our laser, the power drift is small compared to the range of measured signal. We measure the open and closed aperture signal simultaneously to avoid hystereses (an effect well documented in DR1-doped PMMA) To be able to maintain high correlation between nonlinear absorption and refraction, we need to take both data sets at the same time.

The calibration of detectors is performed prior to the data acquisition as previously described. After calibration, we measure the linear transmittance ($t = 0$ or $\epsilon_2 = 0$), D1/D2, which is the aperture ratio $S = 1 - \exp(-2r_a^2/w_a^2)$, where r_a is the radius of the aperture and w_a is the beam radius at the aperture.

3.4.3 Time-scanned transmittance at z positions

Before measuring the transmittance as a function of sample position in the z-direction, we need to determine the range of travel of the translation stage to exceed the Rayleigh length. The Rayleigh length z_0 is determined from the beam waist, w_0, which is is given by

$$z_0 = \pi w_0^2/\lambda. \tag{3.10}$$

Once we determine the diffraction length, we set the scan distance to a value of about $\pm 6z_0$. Note that it is important to measure w_0 (as described in Chapter 2). Since it is

required as an input to determining the relationship between power, intensity, and beam waist which in turn is related to thermal de-focusing. At each z position, the transmitted power through the aperture is measured. When fresh site of the sample is selected by moving the sample in x or y direction, it is important that the incident beam is kept perpendicular to the surface of the sample so that the center of the transmitted beam is not shifted at the aperture.

When mechanisms with two different response times contribute to $\Delta\Phi_0(t)$ in a time-dependent Z-scan experiment, $\Delta\Phi_0$ can be expresses as

$$\Delta\Phi_0(t) = a_1\left[1 - \exp\left(\frac{t}{\tau_1}\right)\right] + a_2\left[1 - \exp\left(\frac{t}{\tau_2}\right)\right], \tag{3.11}$$

where the parameters are selected as $a_1 = -0.05$, $\tau_1 = 0.5s$ and $a_2 = -0.5$, $\tau_2 = 2s$. The data from the time-dependent Z-scan technique can be used to reconstruct Equation (3.11).

The normalized transmittance for several selected positions are shown in Figure 3.10 using Equation (3.11). The initial transmittance through the aperture is the normalization factor when there is no nonlinear refraction, which is set to unity. We observe that when z is negative, the normalized transmittance is larger than unity because de-focusing shifts the focal point downstream of the sample. For the same reason, the normalized transmittance is less than unity for positive z positions. Figure 3.10 shows the normalized transmittance for the case $\Delta\Phi_0 < 0$ whose magnitude decreases as a function of time.

3.4.4 Time-resolved Z-scan

In the previous section, we analyzed the normalized transmittance data for various z positions. From the data in Figure 3.10, we can determine the normalized transmittance at a fixed time t_i for different values of z (see Figure 3.11):

$$T(t, z_i/z_0) \rightarrow T(t_i, z/z_0) \tag{3.12}$$

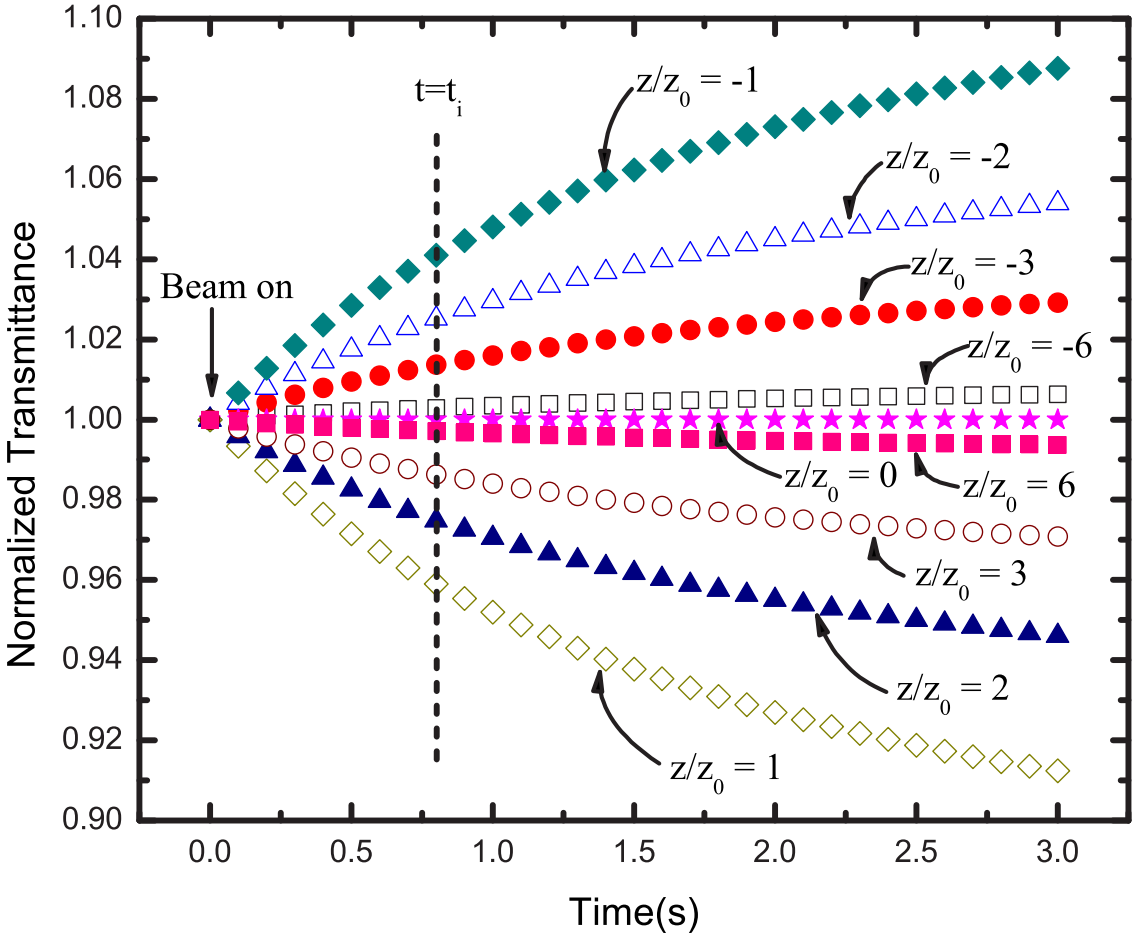

Figure 3.10: Normalized transmittance as a function of time at selected positions z/z_0. The normalized transmittance can be determined for a given time, $t = t_i$, from the intersection of $t = t_i$ with the time-dependent transmittance.

As was shown in Section (3.3.1), the normalized transmittance from a Z-scan experiment using a CW light source is given by

$$T(z, \Delta\Phi_0(t_i)) \simeq 1 + \frac{4\Delta\Phi_0(t_i)\ x}{(x^2+9)\,(x^2+1)}, \tag{3.13}$$

where $x = z/z_0$ and $\Delta\Phi_0(t_i) = k\Delta n_0(t_i)\frac{[1-\exp(-\alpha L)]}{\alpha}$. In contrast with a Z-scan measurement using a pulsed laser, which requires a time average of the ratio of the transmitted power to the input power, the on-axis phase shift for a CW laser is time-dependent only if the third-order susceptibility depends on time. For our samples, we can assume that the transmitted power depends on $\Delta\Phi_0$ instantaneously with the intensity at time t_i.

One of the assumptions of most Z-scan experiment is that the sample is "thin" in which refraction is ignorable; but, the thickness of our sample is not "thin" as a thin film. Therefore, we introduce an effective beam waist due to the effects of nonlocal mechanisms. We stress that this is not a change in the real physical beam waist but this is a mathematical construct to take into account the nonlocal mechanisms. Section 3.7 describes the justification for doing so. This affects the Rayleigh length, z_0 and the peak intensity at focus, $I_0(t)$ as:

$$z_0 = \frac{\pi w_0^2(t_i)}{\lambda} \tag{3.14}$$

and

$$I_0 = \frac{2P}{\pi w_0^2(t_i)}, \tag{3.15}$$

where $w_0(t_i)$ is the effective minimum beam waist at $t = t_i$.

The analysis of the data in Figure 3.11 needs to take into account the modification in Equations (3.14) and (3.15) if changes in beam waist are appreciable. If the beam waist additionally increases the peak width in the Z-scan is broadened and the valley. Additionally, $\Delta\Phi_0$ will yield an increase of the beam size at the aperture. From data fits to the Z-scan theory, we can get $\Delta\Phi_0(t_i)$ for a series of t_i values. Since we are interested in short time

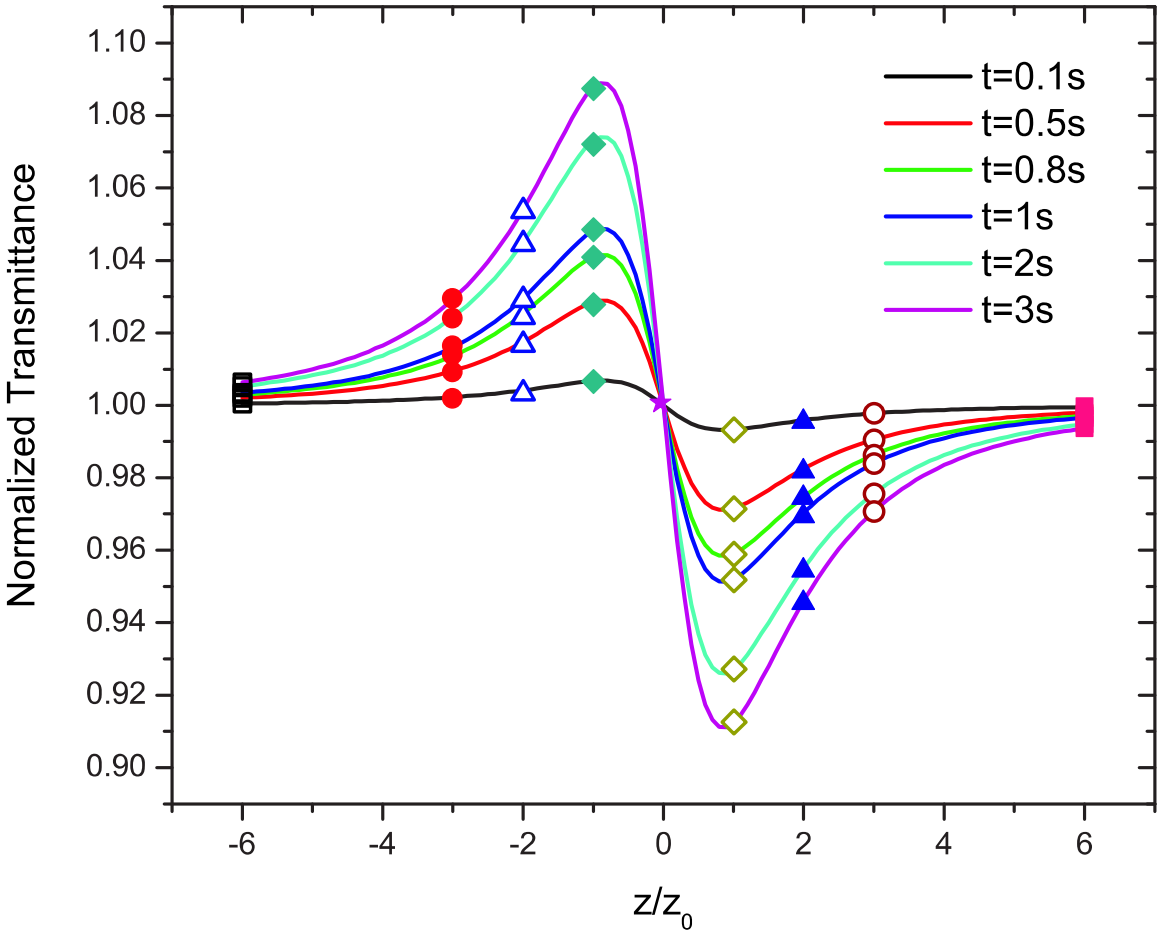

Figure 3.11: Normalized Z-scan transmittance as a function of position z/z_0 at selected times, t. The points are determined from Figure 3.10 at constant time slices and the curves connect the points using the Z-scan theoretical model. $\Delta\Phi_0$ becomes more negative as time increases (see Equations (3.11) and (3.13)).

scales, we use logarithmic sampling, which yields more data pints at early times ($\sim ms$) and less at longer times ($\sim s$).

3.4.5 The time-resolved refractive index

We can determine $\Delta\Phi_0(t_i)$ at time t_i by fitting the data to Equation (3.13). Figure 3.12, shows the result of a fit of the data to Z-scan theory. As shown by Figure 3.12, the fact that the bi-exponential function given by Equation (3.11) fits so well validates our model.

As such from each data points of $\Delta\Phi_0(t_i)$, we can determine the nonlinear refractive index $n_2(t_i)$ as a function of time by using the relationship:

$$n_2(t_i) = \frac{\Delta\Phi_0(t_i)}{kI_0(t_i)} \frac{\alpha}{1 - \exp(-\alpha L)}, \tag{3.16}$$

where $I_0(t_i)$ is the intensity in the sample at t_i. Since the power of the laser is stable in its "light mode" the only intensity changes in the sample will be due to changes of the beam waist as a function of time. In cases when beam waist changes are large the intensity needs to be corrected accordingly. To summarize, a fit of the measured value of $n_2(t)$ to our theory will shed light on the mechanisms contributing to nonlinear refraction.

3.5 Temperature dependent birefringence experiment (OKE)

3.5.1 Phase retardation by optical birefringence

As discussed in Chapter 2 for the DR1 molecule, an anisotropic molecular shape change and orientation of the molecules leads to anisotropic phase retardation. In this section, we derive the power (intensity) transmission for the OKE experiment using Jones matrices. The normalized incident field of the probe beam is linearly polarized with an angle of 45° to the

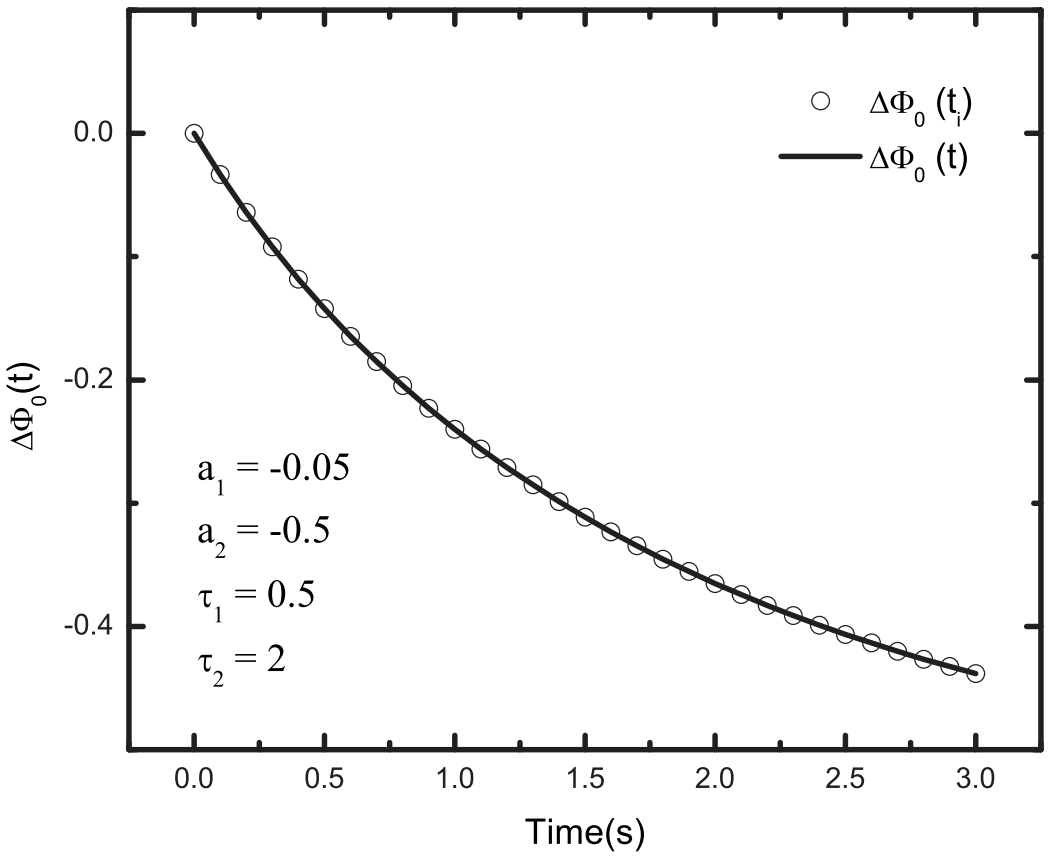

Figure 3.12: $\Delta\Phi_0(t)$ as determined from Figure 3.11. The circles ($\circ$) are the data points, which are determined by fitting the Z-scan theory to the normalized transmittance. The line ($-$) is a fit to the bi-exponential function given by Equation (3.11).

polarization direction of the pump beam which is in the x-direction:

$$E_i = \frac{1}{\sqrt{2}} \begin{bmatrix} 1 \\ 1 \end{bmatrix}. \tag{3.17}$$

In general, the phase retardation matrix for the x and y directions is given by

$$\begin{bmatrix} e^{i\phi_x} & 0 \\ 0 & e^{i\phi_y} \end{bmatrix}, \tag{3.18}$$

where ϕ_x and ϕ_y are phase retardations for the x and y directions due to the pump beam. Also, for a transmission axis at $-45°$ the Jones matrix is given by

$$\frac{1}{2} \begin{bmatrix} 1 & -1 \\ -1 & 1 \end{bmatrix}, \tag{3.19}$$

which represents the analyzer (crossed polarizer) for the probe beam. Therefore, the transmitted field, E_t, can be computed as:

$$\begin{aligned} E_t &= \frac{1}{2\sqrt{2}} \begin{bmatrix} 1 & -1 \\ -1 & 1 \end{bmatrix} \begin{bmatrix} e^{i\phi_x} & 0 \\ 0 & e^{i\phi_y} \end{bmatrix} \begin{bmatrix} 1 \\ 1 \end{bmatrix} \\ &= \frac{1}{2\sqrt{2}} \begin{bmatrix} e^{i\phi_x} - e^{i\phi_y} \\ -\left(e^{i\phi_x} - e^{i\phi_y}\right) \end{bmatrix}. \end{aligned} \tag{3.20}$$

The corresponding normalized transmitted intensity of the probe beam is then:

$$\begin{aligned} |E_t|^2 &= E_t^* E_t \\ &= \sin^2\left(\frac{\Delta\phi}{2}\right) \\ &= \mathcal{T}, \end{aligned} \tag{3.21}$$

where $\Delta\phi = \phi_x - \phi_y$. Equation (3.21) represents the transmitted probe intensity when the pump is off, where $\mathcal{T} = 0$ when $\Delta\phi = 0$.

3.5.2 Motivation of temperature-dependent OKE experiment

The purpose of this dissertation is to study the mechanism of photothermal heating and photoisomerization in dye-doped polymers, and how these mechanisms are coupled.

We do this by analyzing the photothermal effect and its role in agitating in molecular orientational order, which reduces the order induced by photoisomerization/reorientation, as we derived in Chapter 2. By controlling the temperature of the sample when the optical intensity is low, the photothermal contribution can be made negligible. As such, we can isolate the sole effect of the temperature.

3.5.3 Experimental setup

Two separate HeNe(632.8nm) lasers are used for pump (20 mW) and probe (5mW) beams. Separate lasers are used to prevent gratings in the sample due to coherence between the beams. Figure 3.13 shows the experimental setup for the temperature-dependent OKE measurements. The pump is controlled by a shutter that is connected to a controller/timer, similar to the time-resolved Z-scan experiment that used a CW light source. The pump power is controlled by adjusting the angle of a half wave plate that is placed between two polarizers. The second polarizer sets the polarization direction of the pump, which is at 45° related to the probe. A piece of black cardboard is used to absorb the pump beam after it passes through the sample.

The sample is placed in the heat bath, which is connected to a temperature controller and an oil bath. The temperature controller controls the temperature and circulation of the oil in the bath. The internal temperature of the oil bath is set by a panel on the controller. The temperature controller also monitors the temperature of the oil tank, which is not necessarily at the same temperature as the sample; so, we monitor the temperature of

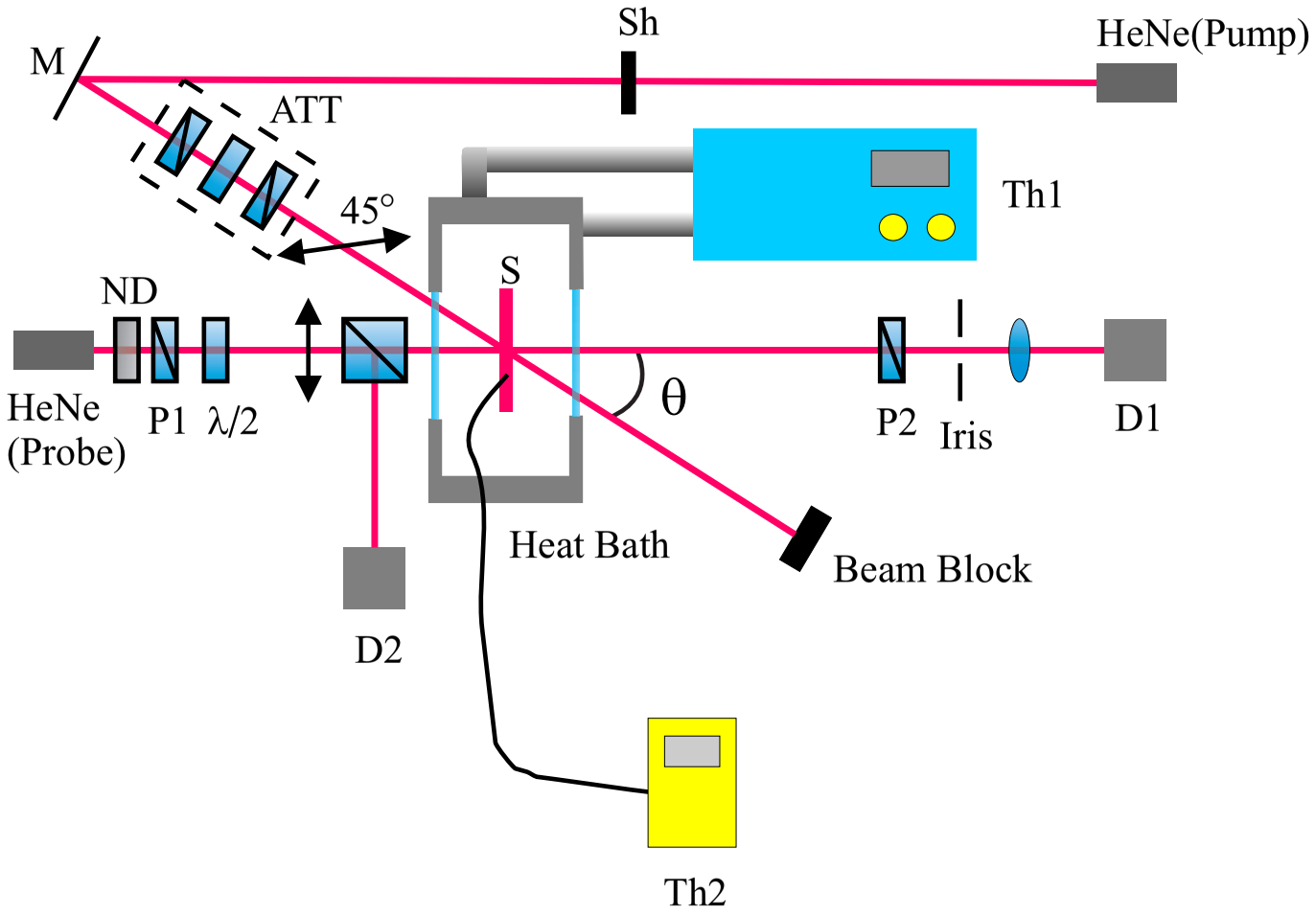

Figure 3.13: Temperature dependent optical kerr gate setup. Sh:Shutter, S:Sample(DR1), M:Mirror, ATT:Attenuator made of a half wave plate sandwiched between two polarizers, P1:Polarizer, P2:Analyzer, $\lambda/2$:half-wave plate, D1:Signal detector, D2:Reference detector, Th1:Temperature controller of the heat bath, and Th2: Thermometer connected with thermocouple in the sample. The pump beam is polarized at 45° to the probe beam polarization. The angle θ between the axes of the pump and probe beams is 5°.

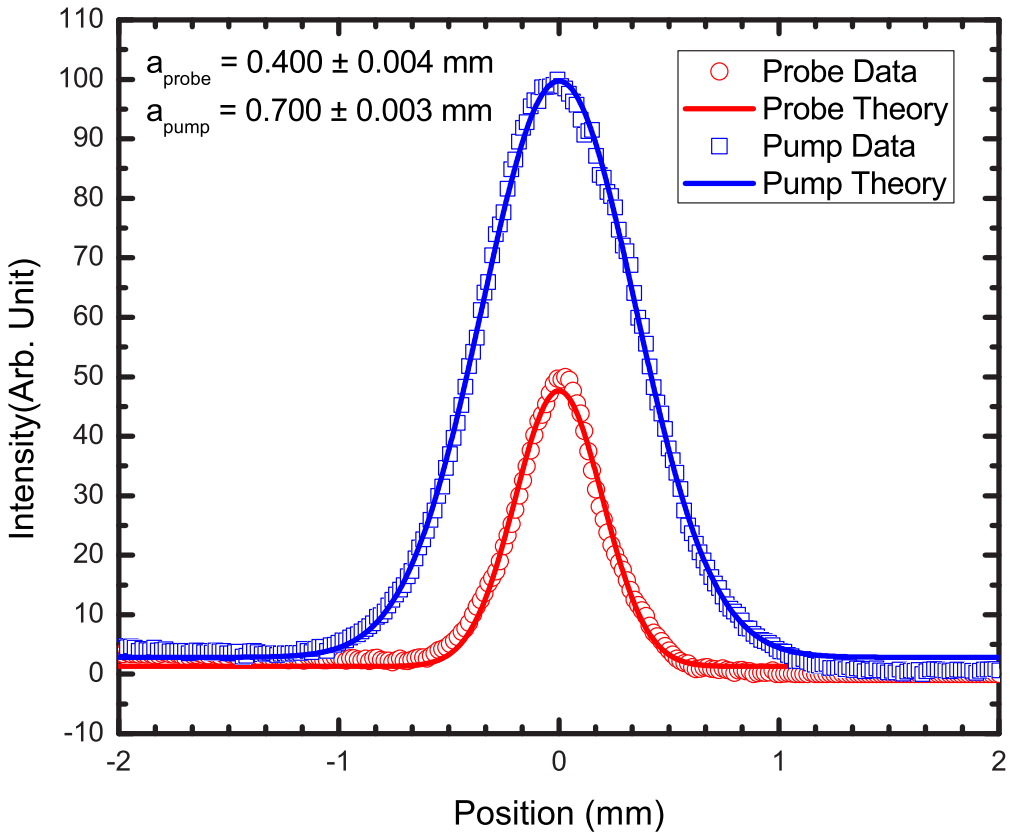

Figure 3.14: Pump and probe beam profiles. Both beams fit a gaussian intensity profile.

the sample directly. The tip of a thermalcouple is embedded in a hole that is drilled in the sample to monitor its temperature directly. Thermal conducting paste is added to this hole to assure good thermal contact.

We have found that the polarization of the probe varies radially. As such, we use only the center part of the beam, which is transmitted through polarizer P1 as a linear polarized beam. The neutral density filter is used to reduce the power of the probe beam to 0.2 % of the pump beam power. P1 and P2 are set with their polarization axes perpendicular to each other. The iris after P2 is used to block any scattered light from the windows of the heat bath and the sample. The beam profiles and the beam radii are shown in Figure 3.14.

In this experiment, since we are not interested in beam size change, the spatial filter is not used to spatially filter the beam shape.

As in the time-resolved Z-scan experiment, the detectors need to be calibrated with each other. When the pump is off, the transmitted probe power is zero. The pump beam causes phase retardation due to birefringence that originates from molecular reorientation which results in probe light passing to the detector. The birefringence, Δn is the determined as showed in Section 3.5.1.

Due to fluctuations of the probe power, a small amount of power is directed to Detector 2 while the rest passes through the sample and to Detector 1. With the pump turned off, the transmission ratio obtained from the ratio of D1/D2 is proportional to $P(L)/P(0)$, and is constant as a function of time. Therefore, the transmission due to the birefringence of the pump beam is obtained by subtracting the transmission at $t = 0$ from the values obtained after the pump is turned on at $t > 0$:

$$\mathcal{T}(t) = \frac{P(L,t)}{P(L=0,t)} - \frac{P(L,0)}{P(L=0,0)}. \tag{3.22}$$

By using Equation (3.21), we calculate the phase change after the sample as a function of time as:

$$\begin{aligned} \Delta\phi(t) &= 2\sin^{-1}\left(\sqrt{\mathcal{T}(t)}\right) \\ &= \frac{2\pi}{\lambda_{probe}}\Delta n\frac{1-\exp(-\alpha L)}{\alpha}, \end{aligned} \tag{3.23}$$

where α is the linear absorption coefficient of DR1 ($5cm^{-1}$). Finally, the birefringence, $\Delta n(t) = n_{\parallel}(t) - n_{\perp}(t)$, is obtained as:

$$\boxed{\Delta n(t) = \frac{\alpha\lambda_{probe}}{\pi\left[1-\exp\left(-\alpha L\right)\right]}\sin^{-1}\left(\sqrt{\mathcal{T}(t)}\right).} \tag{3.24}$$

3.6 Summary

In this chapter, we have shown how the transmittance of a probe beam as a function of time at different z position of the sample can be used to determine the Kerr coefficient as a function of time. Furthermore, we have shown how simulated data for a bi-exponential material response function yields Z-scan data which can be used to separate mechanisms with two time responses. As such, this experimental technique is appropriate for studying photothermal and photoisomerization mechanisms of n_2.

3.7 Appendix: The effective minimum beam waist

In this section, we analyze the effect of a nonlocal response, such as thermal lensing on Z-scan measurements. We find that the intensity depends on the position of the sample in a way that appears as a change in the Rayleigh length. We show that this effect can be taken into account in the standard Z-scan analysis by allowing the minimum beam waist to evolve in time. We stress that the true beam waist is not affected. Rather, our method is the simplest way to generalize the Z-scan analysis for a nonlocal response.

We assume that the heat source is absorbed light so the energy absorbed at any point in the material is proportional to the input beam profile as given by Equation (2.31):

$$Q(r,z) = I_p \exp\left(-\frac{2r^2}{a^2 f^2}\right) \frac{\alpha \exp(-\alpha z)}{f^2}, \tag{3.25}$$

where $Q(r,z)$ is the heat absorbed per unit length per unit time.

The temperature profile can be calculated from the thermal diffusion equation as a function of time in cylindrical coordinates, which are we saw in Section 2.3.1 yields

$$\Delta T(r,z,t) = \frac{I_p \alpha \exp(-\alpha z)}{8\kappa} \left[Ei\left(-\frac{2r^2}{a^2 f^2}\right) - Ei\left(-\frac{2r^2}{a^2 f^2 \left(1+\frac{8Dt}{a^2 f^2}\right)}\right)\right]. \tag{3.26}$$

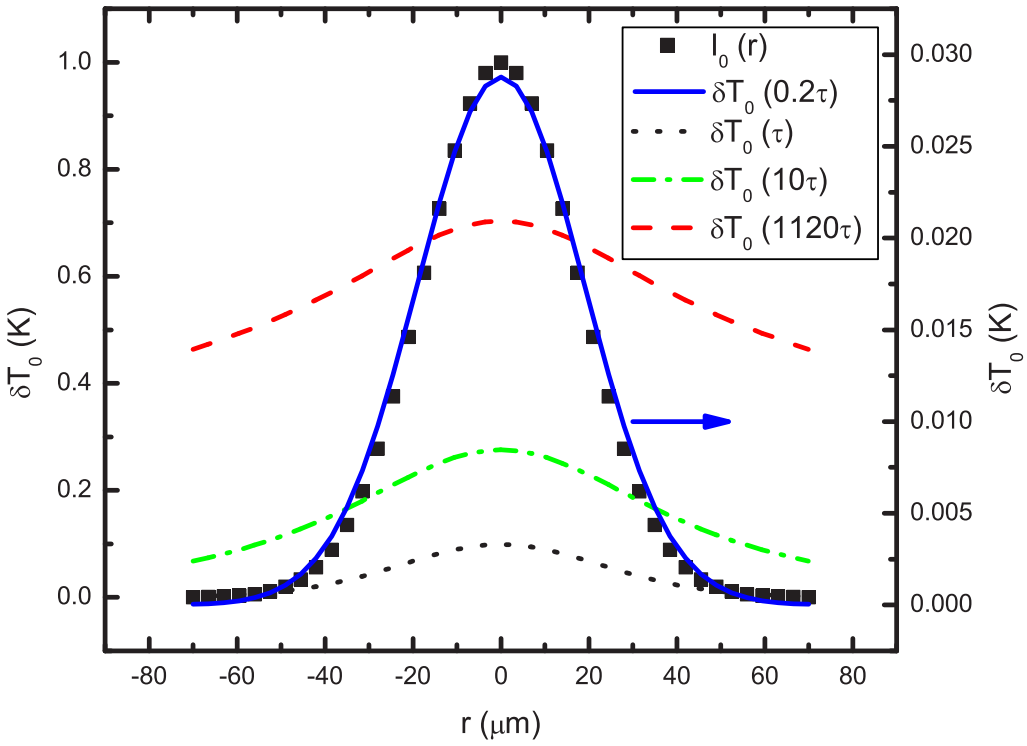

Figure 3.15: Time evolution of the temperature profile and the input beam profile as an input power of $P = 1mW$ and a beam waist of $w_0 = 35\mu m$. All times are expressed in units of the thermal time constant.

The temperature profile evolves as a function of time via thermal diffusion of the heat through the sample from the source to cooler parts of the sample. Figure 3.15 shows the temperature profile at several times. For an infinitesimally small time such as $t = 0.5ms$ - which is much shorter than the thermal time constant τ, the temperature profile is the same as the intensity profile. As a function of time, the temperature profile broadens due to spatial thermal diffusion. Figure 3.16 shows how Δn saturates by subtracting temperature at $t = 3s$ of two other times. For example, at the larger time ($t > 10\tau$), the temperature gradient is saturated.

The Z-scan experiment measures the transmittance as a function of sample position. Figure 3.17 shows the position of the sample and the beam waist as a function of z. Since

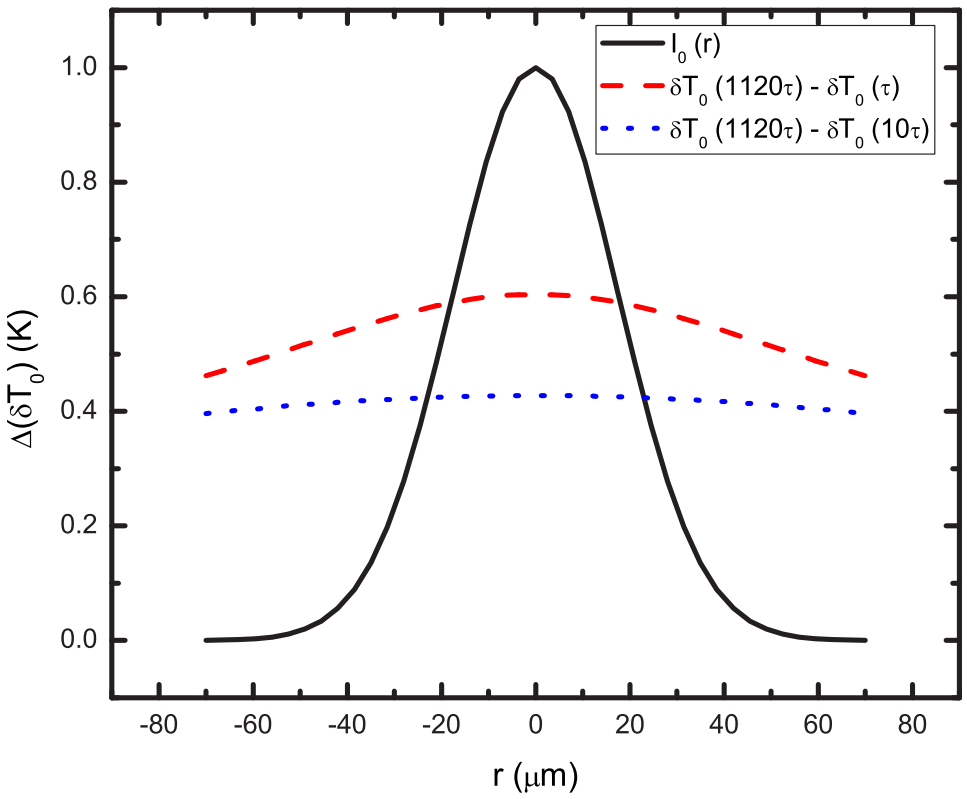

Figure 3.16: Temperature difference between $t = 10\tau$ and $t = 1120\tau$, and $t = \tau$ and $t = 1120\tau$.

our aperture size is small, we need only to consider the on-axis phase shift, $\Delta\phi_0$. As we saw in Section 2.3.1, the thermal lens time constant is given by

$$\tau = \frac{a^2}{4D}, \tag{3.27}$$

where a is the beam width at the input to the sample and D is the diffusivity, $\kappa/\rho c$. Since we are using a focused gaussian beam, the beam width as a function of z is given by, $w(z) = w_0\left(1 + z^2/z_0^2\right)^{1/2}$. The time constant depends on $w(z)$ at the sample, which governs the dynamics of the on-axis temperature increase. As such, the dynamics will depend on z because $w(z)$ is a function of z. Figure 3.18 shows the on-axis temperature increase, δT_0, as a function of lab coordinate, z. Since the on-axis Δn is given by

$$\Delta n(t) = -\frac{\alpha P}{4\pi\kappa\left(1 + \tau/2t\right)}\frac{\partial n}{\partial T}, \tag{3.28}$$

for fixed power and for $t = \tau$, Δn is independent of the beam waist. Figure 3.18 shows that δT_0 is the same for two beam waists, $35\mu m$ and $70\mu m$, at $z = 0$. Note that on-axis, Δn is linearly proportional to δT_0. Because the Rayleigh length, z_0, is determined by the minimum beam waist and uniquely determines propagation of a gaussian beam in free space, the normalized coordinate, z/z_0, is more appropriate for comparing beams. Figure 3.19 shows $\delta T_0(z/z_0)$ for $w_0 = 35\mu m$ and $w_0 = 70\mu m$. The behavior is identical so that Δn is the same as expected.

The on-axis phase shift due to the sample, $\Delta\phi_0$, is proportional to δT_0. $\Delta\phi_0(z)$ of an equivalent local effect is plotted as the blue dotted line. The on-axis phase change for the local effect, $\Delta\phi_0(z,t)$, obeys

$$\Delta\phi_0(z,t) = \frac{\Delta\Phi_0(t)}{1 + z^2/z_0^2}, \tag{3.29}$$

where $\Delta\Phi_0(t)$ is the on-axis phase shift at the focal point. Comparing the local and nonlocal on-axis phase change as shown in Figure 3.19, the nonlocal effect is broader, as a function

of z/z_0, than local one.

If we rescale the nonlocal thermal response so that the Rayleigh length, z_0, is bigger, all of the plots in Figure 3.19 can be made identical. Mathematically, this is equivalent to increasing the minimum beam waist, w_0. Since the Z-scan experiment is usually analyzed under the assumption of a local response, we propose that increasing the beam waist by an appropriate amount allows the standard Z-scan analysis to apply. We stress that the physical beam waist is not affected; but rather, that this is a mathematical trick for allowing the Z-scan data to be analyzed.

When using the standard Z-scan experiment on a material with a nonlocal response, the transmitted intensity through the aperture will behave in a qualitatively different way from the local response. To take into account nonlocal mechanisms, we will allow the effective minimum beam waist act as an adjustable parameter. Thus, the deviation between the actual beam waist and the effective one will be a measure of the strength of the nonlocal response.

Motivated by the on-axis refractive index change as given by Equation (4.4), we propose that the effective beam area obeys the same function, so that the change in the beam waist is given by

$$(\Delta w_0)^2 (t) \rightarrow \frac{(\Delta w_0)^2}{1 + \tau/2t}, \tag{3.30}$$

where Δw_0 is the change of the beam waist at $t \rightarrow \infty$.

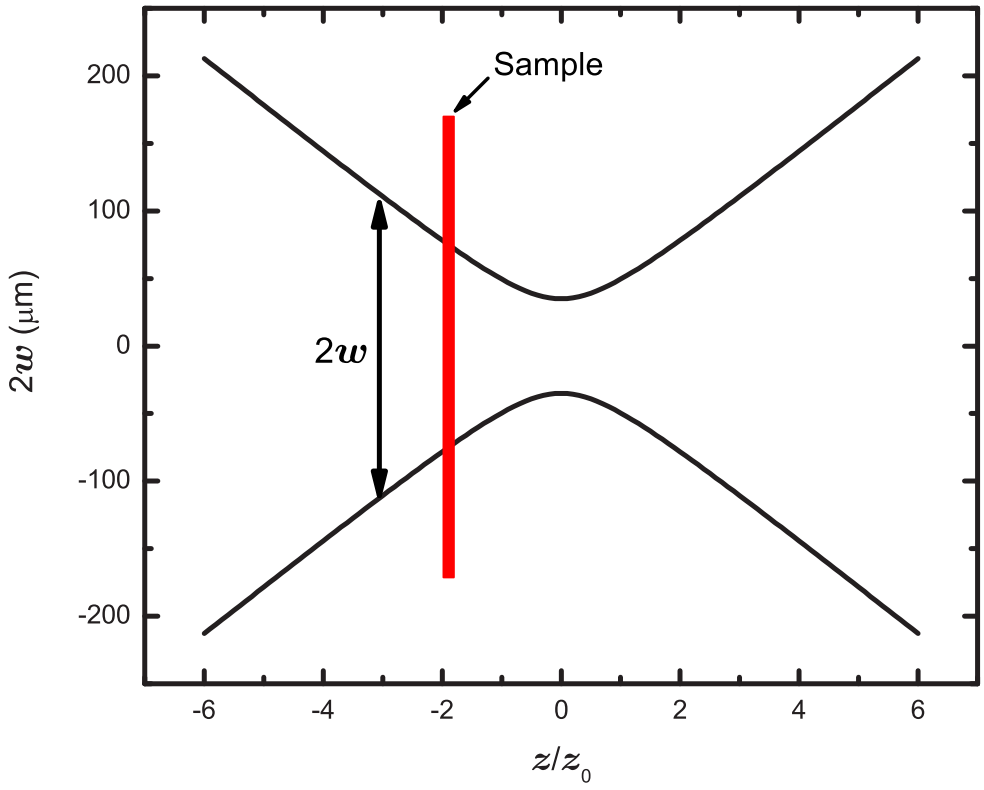

Figure 3.17: The beam waist as a function of z/z_0 with $w_0 = 35\mu m$. The on-axis phase shift due to the sample is proportional to on-axis temperature increase, δT_0, at the beam center.

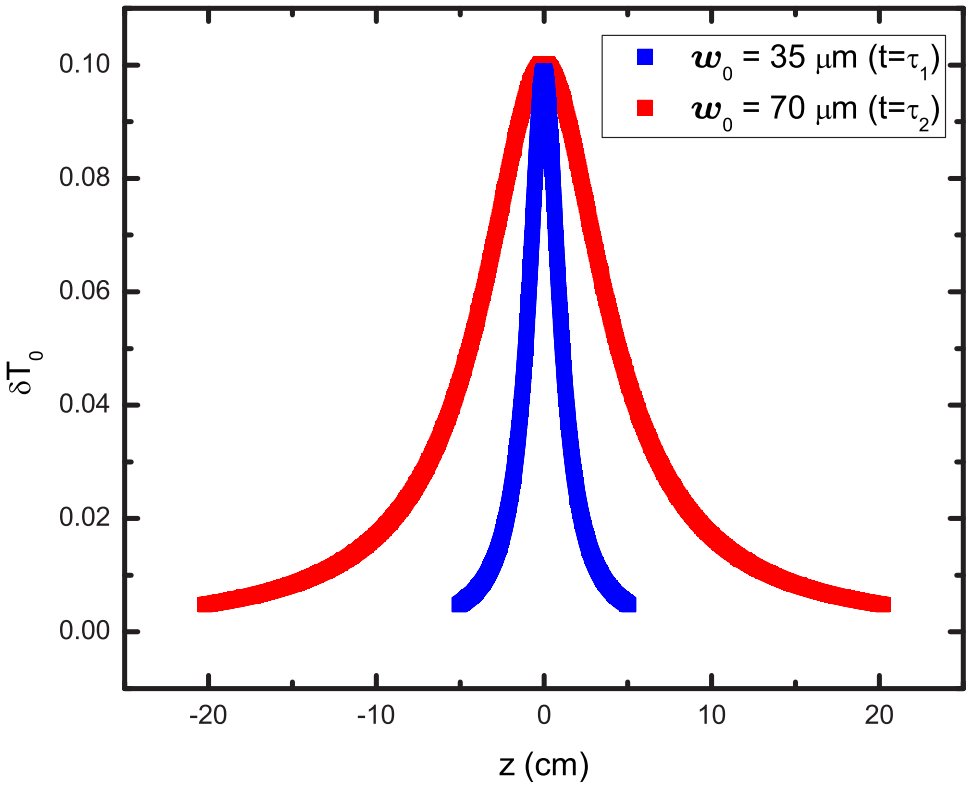

Figure 3.18: On-axis temperature increase of the sample, δT_0, at $t = \tau$ and $P = 1mW$ for $w_0 = 35$ and $70\mu m$ as function of position of the sample.

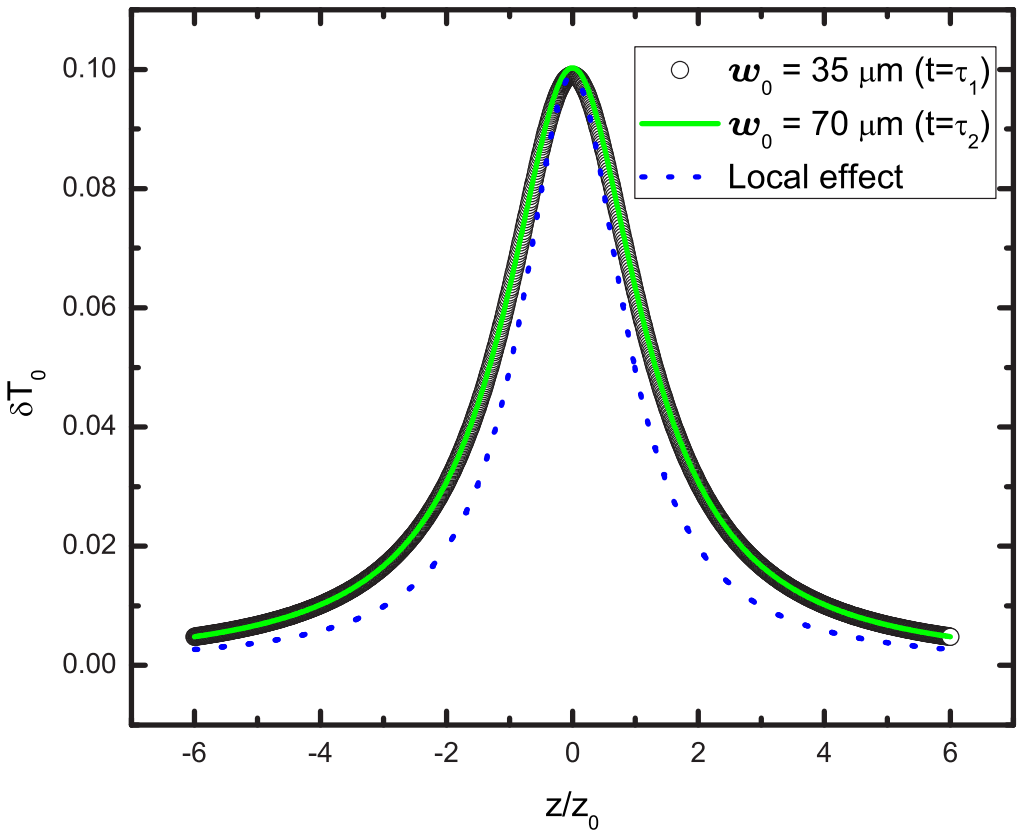

Figure 3.19: Plots of δT_0 as a function of z/z_0 for $w_0 = 35$ and $70\mu m$ show that the nonlocal thermal lens effect for both yield the same on-axis temperature profile as a function of z/z_0. The dotted blue line is the phase change due to the sample if the effect were local, for comparison.

Bibliography

[1] M. Sheik-Bahae, A. A. Said, T. Wei, D. J. Hagan, and E. W. van Stryland, "Sensitive measurement of optical nonlinearities using a single beam," IEEE J. Quantum Electron. **26**, 760 (1990).

[2] D. Weaire, B. S. Wherrett, D. A. B. Miller, and S. D. Smith, "Effect of low-power nonlinear refraction on laser-beam propagation in InSb," Opt. Lett. **4**, 331 (1979).

[3] J. Wang, M. Sheik-Bahae, A. A. Said, D. J. Hagan, and E. W. van Stryland, "Time-resolved Z-scan measurements of optical nonlinearities," J. Opt. Soc. Am. B **11**, 1009 (1994).

[4] C. R. Mendonca, L. Misoguti, and S. C. Zilo, "Z-scan measurements with Fourier analysis in ion-doped solids," Appl. Phys. Lett. **71**, 2094 (1997).

[5] C. R. Mendonca, M. M. Costa, J. A. Giacometti, F. D. Nunes, and S. C. Zilio, "Nonlinear refractive indices of polystyrene films doped with azobenzene dye Disperse Red 1," **34**, 116 (1998).

[6] L. C. Oliveira and S. C. Zilio, "Single-beam time-resolved Z-scan measurements of slow absorbers," Appl. Phys. Lett. **65**, 2121 (1994).

Chapter 4

Results and Discussion

In this chapter, we study two dye-doped systems: DB14 dye doped in PMMA, which should exhibit only a photothermal contribution to Z-scan data; and DR1 dye doped in PMMA, which responds to light with both photothermal and photoisomerization. By using a combination of TZ-scan measurements on these two samples, as a function of time and polarization, the slow third-order nonlinear optical mechanisms in DR1 can be decoupled and our theories tested.

4.1 Thermal lens effect in Disperse Blue 14/PMMA

In this section, we study the photothermal effect due to linear absorbance in DB14 at a concentration of 0.022 wt. % in PMMA (DB14/PMMA) in the off-resonant regime at $\lambda = 457nm$. Since DB14 has no means for photoisomerization, the heating mechanism can be measured directly. Furthermore the concentration of DB14 dye used yields about the same amount of light absorption as in the DR1 experiments so we anticipate that the parameters of the photothermal properties of the two samples will be similar. Given the low dye concentrations used, the bulk properties of the dye-doped polymer should be similar to that of PMMA. Thus, the physical constants for PMMA polymer obtained from the literature can be used to apply the theory, with no adjustable parameters, to the experimental

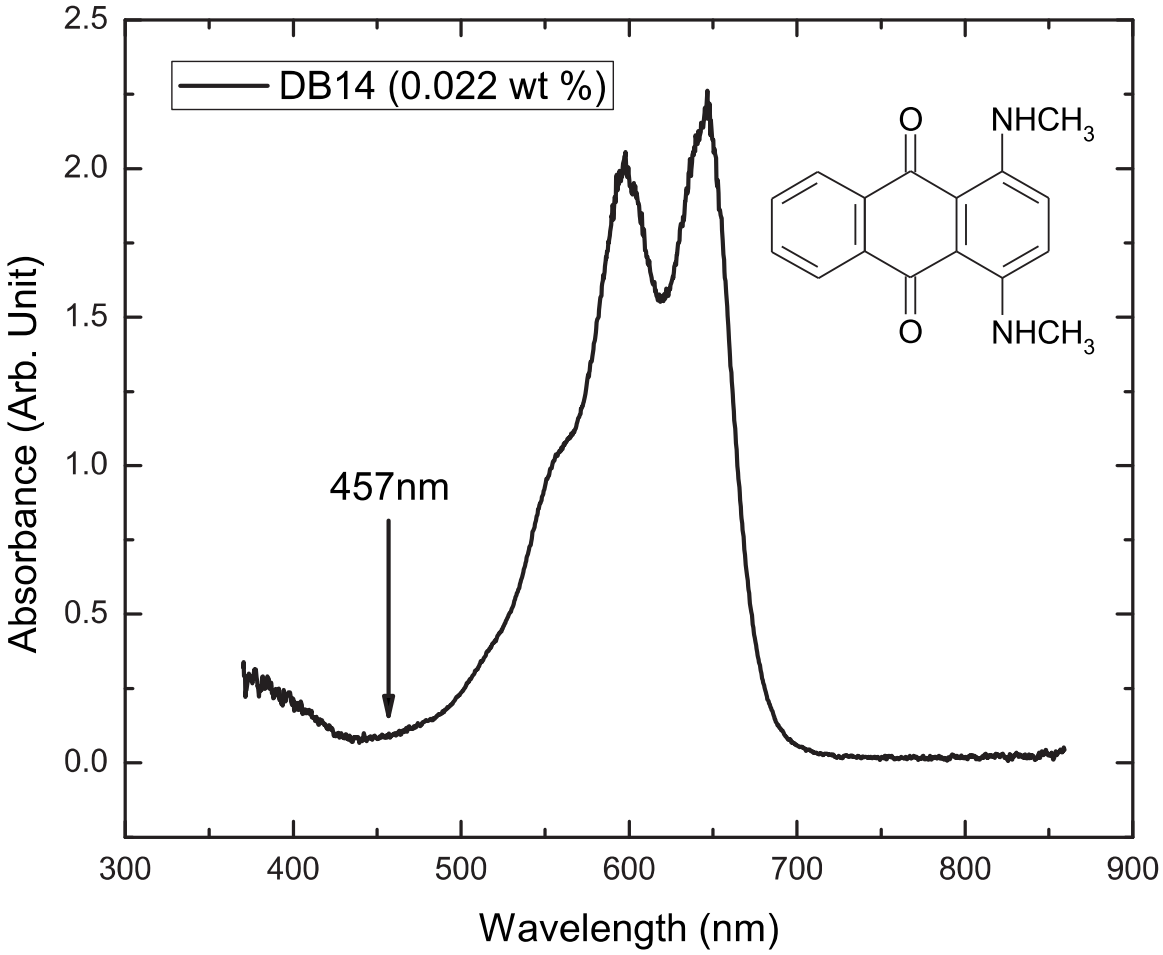

Figure 4.1: Absorption spectrum of DB14 (0.022 wt.%). The inset is the molecular structure of DB14. $\lambda = 457nm$ is the wavelength used in the TZ-scan experiment.

results.

4.1.1 Linear absorbance DB14/PMMA

The thermal lens effect originates from the linear absorption of energy from the light source by dye molecules in PMMA and the theory of the response is derived in Section 2.3.2. DB14 dye is used as a baseline material with only thermal effect without other mechanisms such as photo-isomerization. DB14 doped in a nematic liquid crystal can lead to molecular reorientation;[1][2] but, the effect is due to interaction between DB14 and a highly ordered liquid crystal system. Such an effect should not take place in an isotropic polymer, nor

do we observe any evidence of such an effect. To minimize other potential mechanisms, an off-resonance frequency light source is chosen. Figure 4.1 shows the absorption spectrum and the molecular structure of DB14. It is obvious that 457 nm is in the off-resonance regime. To more accurately measure the linear absorption coefficient at 457 nm we use, the transmittance of a Kr. laser at 457 nm through a length of sample whose thickness is measured with a micrometer. The absorption coefficient is obtained by the relationship:

$$\alpha = -\frac{\ln Tr}{L}, \tag{4.1}$$

where Tr is the transmittance and L is the length of the sample. The absorption coefficient at 457 nm is determined experimentally to be 1.72 cm^{-1}.

4.1.2 TZ-scan for DB14

Since the photothermal response is nonlocal, the beam and temperature profile are of different widths so the change of beam waist in the sample is a parameter that needs to be monitored. To center the z coordinate, the center parameter, z_c, is introduced. As such, the normalized transmittance is modified as follows: (See Section 3.4.4)

$$\begin{aligned} T(z, \Delta\Phi_0(t_i)) &\simeq 1 + \frac{4\Delta\Phi_0(t_i)\ z/z_0}{((z/z_0)^2+9)\left((z/z_0)^2+1\right)} \\ &= 1 + \frac{4\Delta\Phi_0(t_i)\left(\frac{(z-z_c)\lambda}{\pi w_0(t_i)}\right)}{\left[\left(\frac{(z-z_c)\lambda}{\pi w_0(t_i)}\right)^2+9\right]\left[\left(\frac{(z-z_c)\lambda}{\pi w_0(t_i)}\right)^2+1\right]}. \end{aligned} \tag{4.2}$$

The measured normalized transmittance is plotted in Figure 4.2 at four selected times, with best fits to Equation (4.2). The method used to transform the normalized transmittance as a function of time to the normalized transmittance as a function of z is described in Section 3.4.4. It is observed that the difference in peak and valley heights are increasing as a function

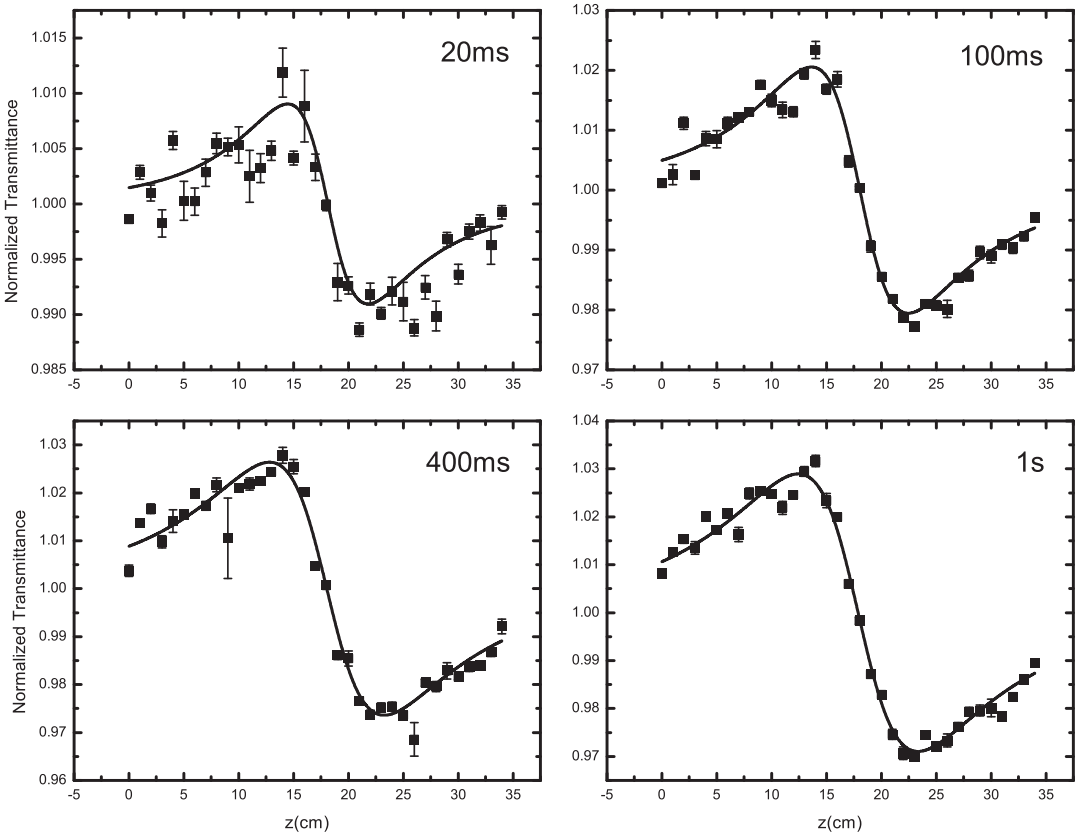

Figure 4.2: A snapshot at four selected times of a TZ-scan of DB14 (points) and a fit to theory (curves). The beam waist measured without the sample is $65.06 \pm 0.44 \mu m$ and the input power is 0.755mW.

of time, which implies that $\Delta n(t_i)$ is increasing in magnitude and becoming more negative. The width of the peak and valley increases as the effective minimum beam waist increase as a function of time. In the fitting process, the so-called TZ-scan technique, $\Delta\Phi_0(t_i)$, $w_0(t_i)$. and $z_c(t_i)$ are obtained at a series of fixed times t_i.

4.1.3 Comparison of TZ-scan with other work

The thermal lens effect has been studied with the Z-scan technique using a two-color pulsed light source in the steady state[3], with a CW pump-probe setup[4], in the steady state associated with calorimetry in response to a CW laser[5], in determination of the Soret coefficients[6], and by using Fourier transform techniques with a CW laser[7].

The uniqueness of our method for analysis is as follows:

- Ability to analyze Z-scan data at discrete times: using a CW single beam.
- Takes into account nonlocal mechanisms by introducing an effective minimum beam waist.

Figure 4.3 shows comparison between theory 1 (solid line), which accounts for the effective minimum beam waist change and theory 2 (dashed line), the standard theory. In this experiment, when $w_0 = 65\mu m$, $z_0 = 2.9cm$ and when $w_0 = 35.1\mu m$, $z_0 = 8.5mm$, where each value of z_0 is larger than the thickness of the sample ($1.4mm$). Our sample is thick enough to cause refraction within the sample and to be able to introduce a time evolution of the effective minimum beam waist under the typically-assumed condition of Z-scan experiments that $z_0 > L$. The standard theory keeps the beam waist constant and is assumed to be the same as beam profile without a sample so that a thin film sample is assumed to not introduced refraction within the sample.

In Figure 4.3, the distance between peak and valley of the data is larger than what is predicted by the standard theory but is well matched to our theory that the effective minimum beam waist changes with time. The dashed arrows indicate the degree of broadening.

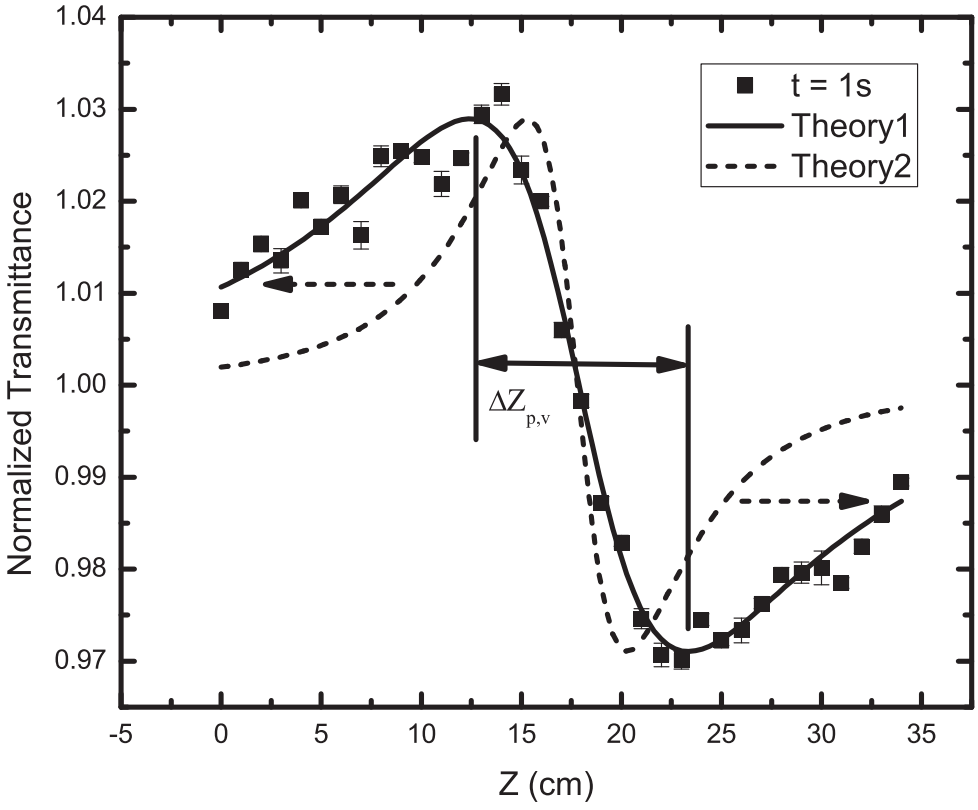

Figure 4.3: The comparison between our theory (solid curve) which accounts for an effective minimum beam waist, $w_0(t)$ and the standard theory (dashed curve) with $w_0 = 65\mu m$ when $t = 1s$. Theory 1 is with time-dependent effective minimum beam waist, $w_0(t)$. The dashed arrow indicates the increase of the Rayleigh length due to the time dependent effective minimum beam waist, $w_0(t)$.

Even with a time dependence of $w_0(t)$ the condition that $\Delta z_{p,v} \simeq 1.7 z_0$ still holds.[8] For example, $\Delta z_{p,v} = 10.99cm \simeq 1.7 z_0 = 10.8cm$ but $\Delta\Phi_0$ is the same ($\Delta\Phi_0 = -0.143 \pm 0.090$) for both cases. Since $\Delta\Phi_0$ is invariant between cases $w_0^2(t)$ in the fitting process does not affect $\Delta n(t)$ but affects for $n_2(t)$ through the intensities. We will discuss more about $w_0^2(t)$ and how it is related to $n_2(t)$ in Sections 4.1.6 and 4.1.7.

$P(mW)$	$w_0(\mu m)$	$\Delta n_{sat}(\times 10^{-5})$	$\tau(ms)$
0.755	65.06 ± 0.44	-0.857 ± 0.051	83.8 ± 2.8
1	65.06 ± 0.44	-1.31 ± 0.01	99.3 ± 2.7
7.19	35.11 ± 0.42	-6.452 ± 0.047	34.3 ± 1.2

Table 4.1: Parameters obtained from fits for Δn of thermal effect for DB14/PMMA in Figure 4.4 –4.6.

4.1.4 The change of refractive index, Δn as a function of time and time constant τ

$\Delta n(t_i)$ is calculated from $\Delta\Phi_0(t_i)$ which is obtained from fitting the Z-scan data at a discrete time t_i as follows:

$$\begin{aligned} \Delta\Phi_0(t_i) &= k\Delta n_0(t_i) L_{eff} \\ &= k\Delta n_0(t_i)\frac{1-\exp(-\alpha L)}{\alpha}, \end{aligned} \tag{4.3}$$

where $\Delta\Phi_0(t_i)$ is the on-axis change of the phase at time t_i, k is the wave number, L_{eff} is the effective length, α is the linear absorption coefficient, and $\Delta n_0(t_i)$ is the on-axis change of refractive index which for continuous time is denoted by $\Delta n(t)$ in Equation (4.4).

Δn at discrete times is plotted as a logarithmic function of time in Figures 4.4 – 4.6. Our theory for the change of refractive index for the thermal lens effect as a function of time by Equation (2.86):

$$\Delta n(t) = -\frac{\alpha P}{4\pi\kappa\,(1+\tau/2t)}\frac{\partial n}{\partial T}, \tag{4.4}$$

is used to fit the data, where the negative sign is for defocusing. Table 4.1 shows the fitting parameters used in Figures 4.4 – 4.6.

The theoretical time constant is given by[9] (See Equations (B-9) and (2.42))

$$\tau^{theory} = \frac{w_0^2}{4D}, \tag{4.5}$$

where D is the diffusivity given by $\kappa/\rho c$. Table 4.3 shows the comparison of τ^{exp} and τ^{theory}.

$\alpha(cm^{-1})$	$\frac{\partial n}{\partial T}(K^{-1})$	$\kappa(W/m \cdot K)$	$\rho(kg/m^3)$	$c(J/kg \cdot K)$
1.72	1.5×10^{-4}	0.193	1.19×10^3	1.42×10^3

Table 4.2: Physical constants of PMMA.[10]

$P(mW)$	$w_0(\mu m)$	$\tau^{exp}(ms)$	$\tau^{theory}(ms)$
0.755	65.01	83.8 ± 2.8	9.25
1	65.01	99.3 ± 2.7	9.25
7.19	35.11	34.3 ± 1.2	2.7

Table 4.3: Comparison between the theoretical and experimental time constants.

When we compare τ theoretically calculated by using parameters in Table 4.2, there are disagreement from τ measured. The experimental values are about 10 times larger than the theoretical values. More details about the time constant will be discussed in Section 4.1.8.

4.1.5 The time dependence of effective minimum beam waist $w_0(t)$ and time constant τ

From TZ-scan fitting process, the time-dependence of w_0 was obtained from the distance between peak and valley and their widths. In this section, our theory is modified based on these experimental results. Heat transfer from a heat source through the sample was described in Chapter 2. The on-axis temperature as a function of time from Equation (2.85) is given by

$$\delta T(t) = \frac{\alpha P}{4\pi\kappa\,(1+\tau/2t)}. \tag{4.6}$$

Since the photothermal heating is a nonlocal effect due to diffusion from the heat source (the input beam shape) and that the change of thermal refractive index is proportional to the temperature increase, the time dependence of effective minimum beam waist would follow $\delta T(t)$ in Equation (4.6). According to the boundary conditions:

$$w_0^2(t=0) = w_0^2 \tag{4.7}$$

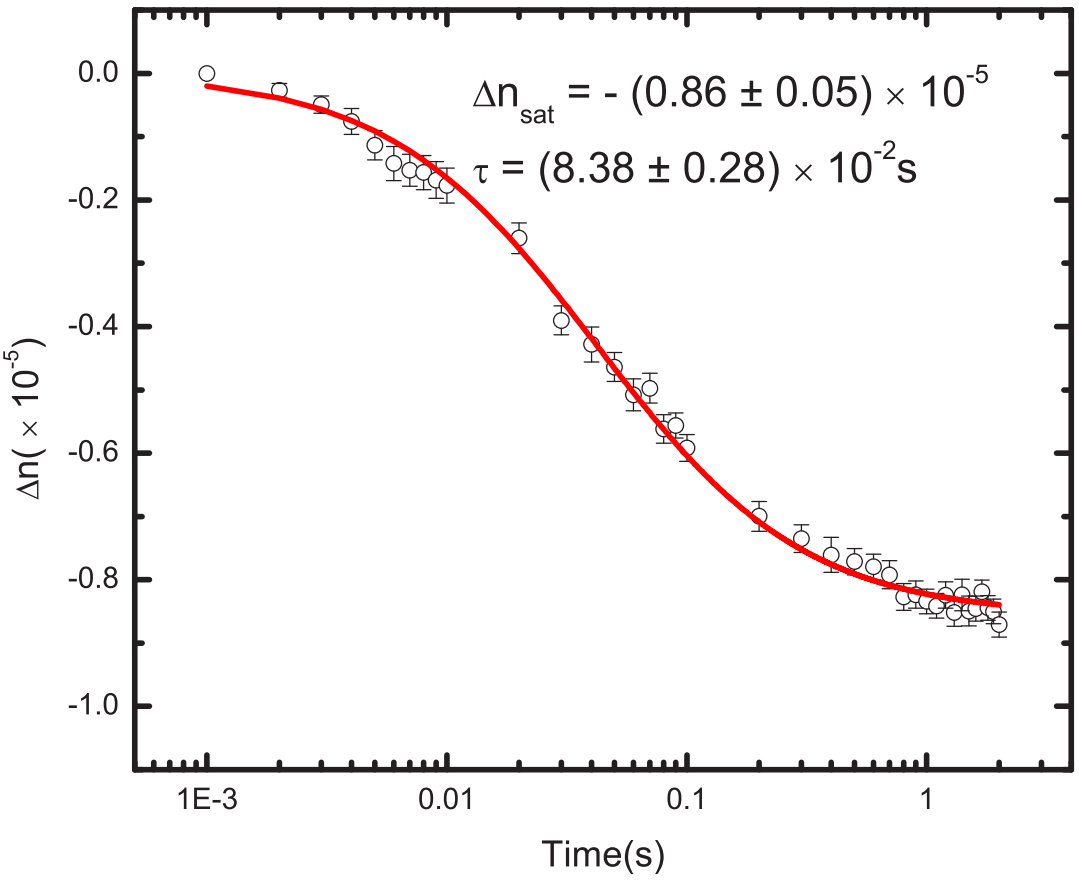

Figure 4.4: The refractive index change, $\Delta n(t)$, due to the photothermal effect. The circles ($\circ$) are the data points and the red line (—) is the theory fit. $\Delta n_{sat} = -\frac{\alpha P}{4\pi\kappa}\frac{\partial n}{\partial T}$ in Equation (4.4). The parameters are shown in Table 4.1. $P = 0.755mW$.

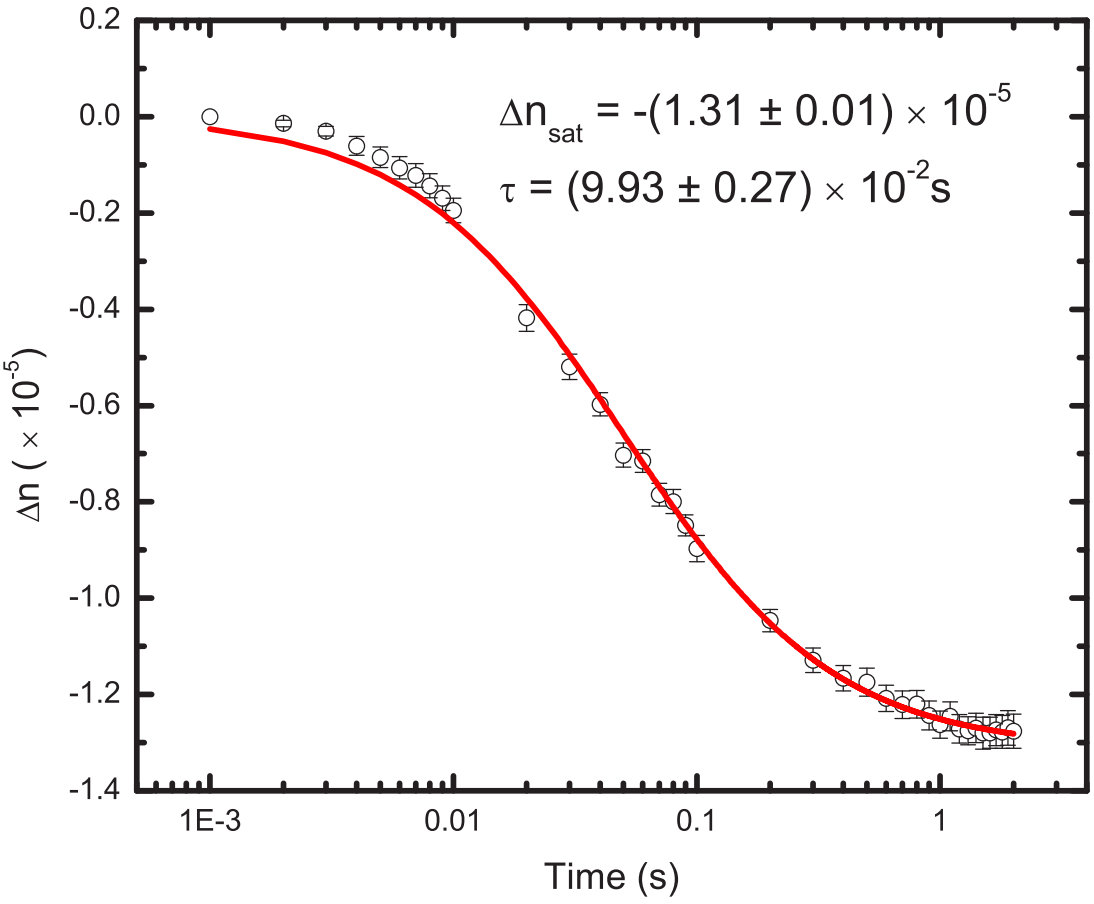

Figure 4.5: The refractive index change, $\Delta n(t)$, due to the photothermal effect. The circles ($\circ$) are the data points and the red line (—) is the theory fit. $\Delta n_{sat} = -\frac{\alpha P}{4\pi\kappa}\frac{\partial n}{\partial T}$ in Equation (4.4). The parameters are shown in Table 4.1. $P = 1mW$.

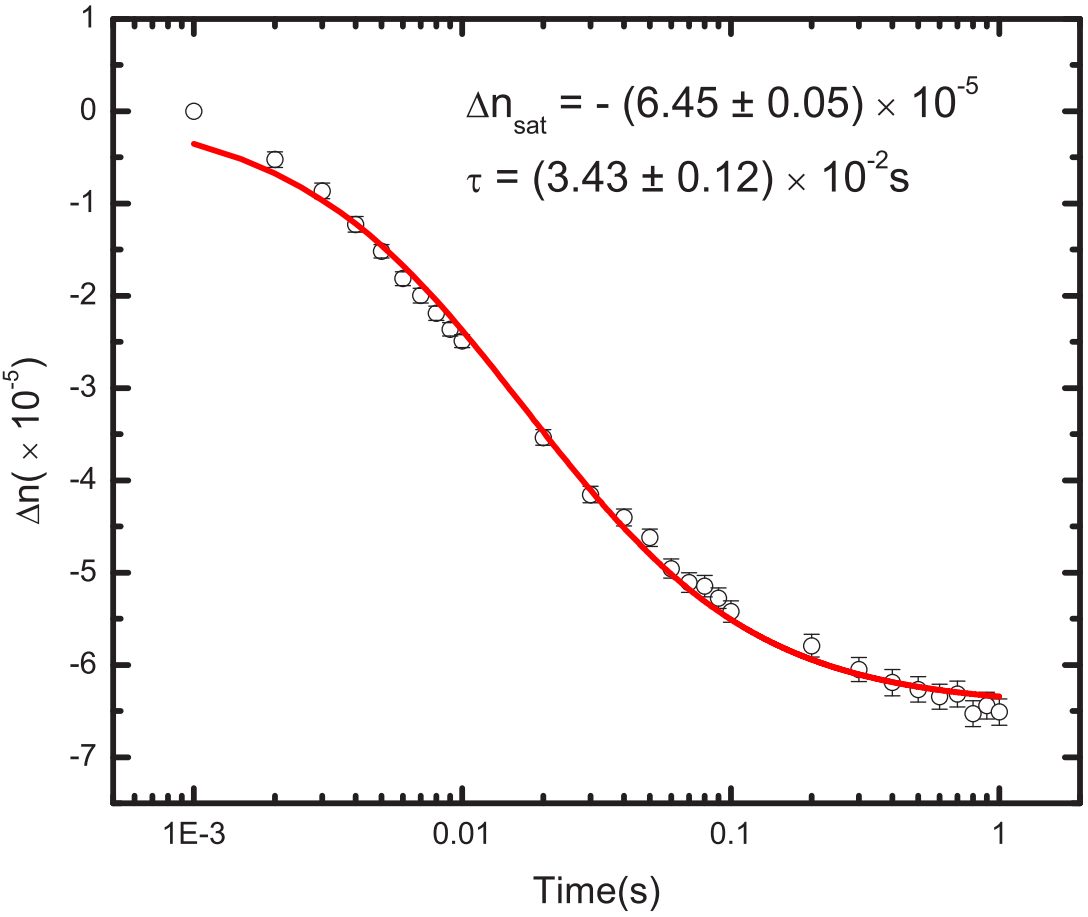

Figure 4.6: The refractive index change, $\Delta n(t)$, due to the photothermal effect. The circles ($\circ$) are the data points and the red line (—) is the theory fit. $\Delta n_{sat} = -\frac{\alpha P}{4\pi\kappa}\frac{\partial n}{\partial T}$ in Equation (4.4). The parameters are shown in Table 4.1. $P = 7.19mW$.

and

$$\lim_{t\to\infty} w_0^2(t) = w_0^2 + \Delta w_0^2, \tag{4.8}$$

we propose that $w_0^2(t)$ as a function of time is:

$$w_0^2(t) = w_0^2 + \Delta w_0^2/(1 + \tau/2t). \tag{4.9}$$

Figures 4.7 – 4.9 show the experimental values of $w_0^2(t)$ as determined using Z-scan and allowing w_0 to be a free parameter at each time and fits to Equation (4.9). At small times, the peaks and valleys of normalized transmittance data are small and difficult to measure. Therefore, the error bars in the short-time regime ($t < 10ms$) are larger than those longer times ($t > 10ms$).

In Figure 4.7, $w_0 = 54.6 \pm 1.9\mu m$ and $\Delta w_0 = 82.9 \pm 1.3\mu m$. w_0 obtained from the knife edge method is $65.06 \pm 0.44\mu m$. In Figure 4.8, $w_0 = 68.5 \pm 0.4\mu m$ and $\Delta w_0 = 71.0 \pm 0.5\mu m$. w_0 obtained from the knife edge method is $65.06 \pm 0.44\mu m$. In Figure 4.9, $w_0 = 40.3 \pm 0.4\mu m$ and $\Delta w_0 = 31.4 \pm 0.5\mu m$. w_0 obtained from the knife edge method is $35.11 \pm 0.42\mu m$. As such, $w_0 \sim \Delta w_0$ and the measured beam waists without a sample are close to w_0 determined from the fits.

4.1.6 The nonlinear refractive index $n_2(t)$ of photothermal heating

Considering time-dependent intensities as a function of time associated with $w_0^2(t)$, $\Delta n(t)$ is modified as follows:

$$\begin{aligned} \Delta n(t) &= n_2(t) I_p(t) \\ &= n_2(t) \frac{2P}{\pi w_0^2(t)}. \end{aligned} \tag{4.10}$$

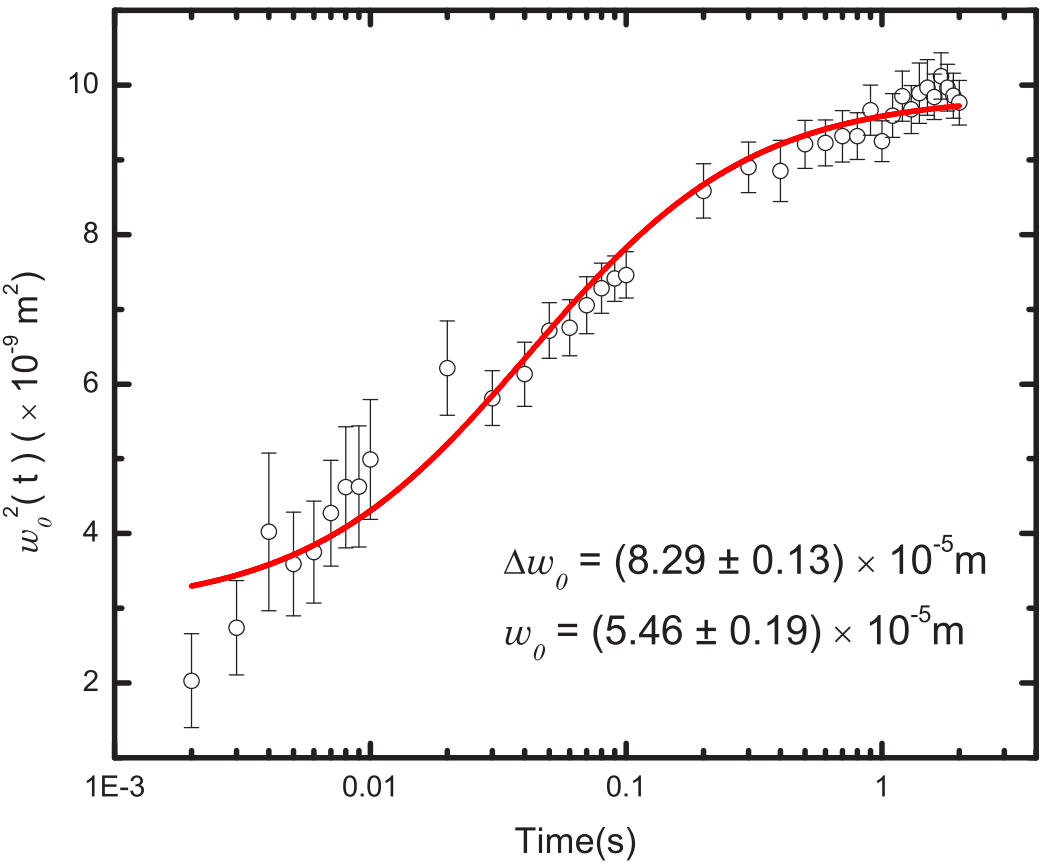

Figure 4.7: The time evolution of $w_0^2(t)$. The circles ($\circ$) are the data points and the red line (—) is the theory fit. $w_0^2(t) = w_0^2 + \Delta w_0^2/(1 + \tau_2/2t)$. $P = 0.755mW$.

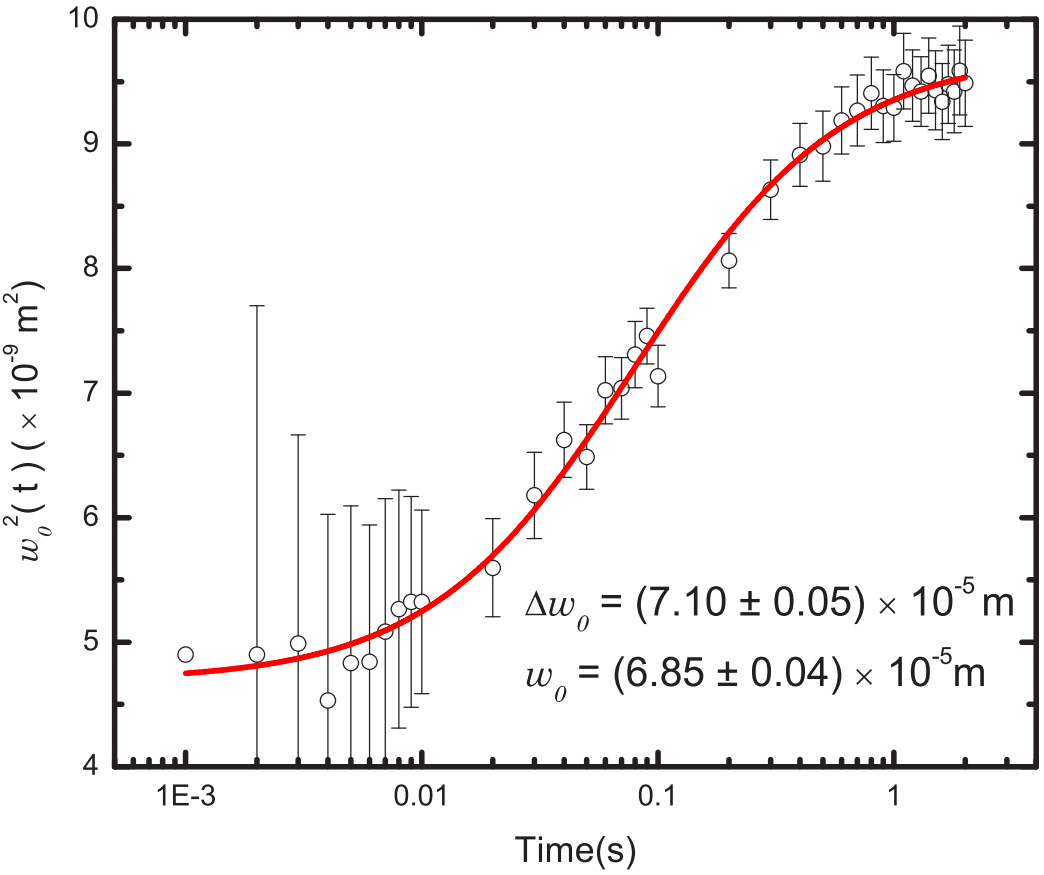

Figure 4.8: The time evolution of $w_0^2(t)$. The circles ($\circ$) are the data points and the red line (—) is the theory fit. $w_0^2(t) = w_0^2 + \Delta w_0^2/(1 + \tau_2/2t)$. $P = 1mW$.

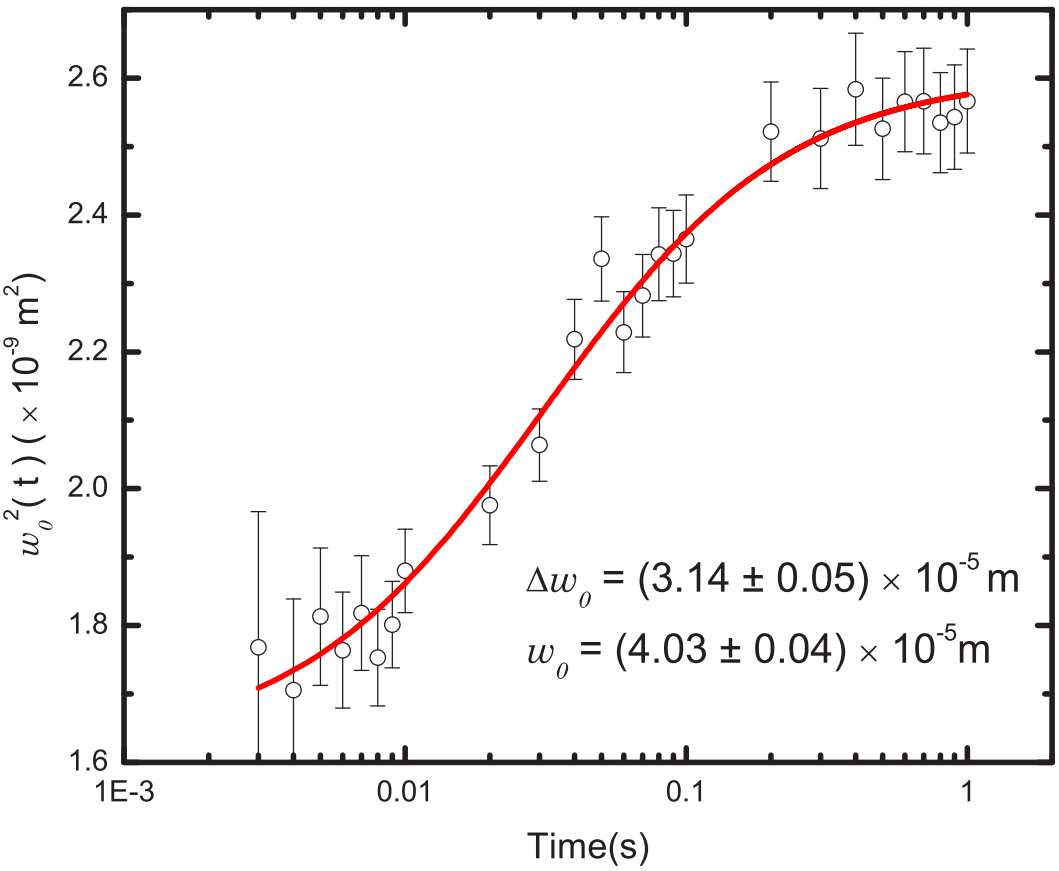

Figure 4.9: The time evolution of $w_0^2(t)$. The circles (∘) are the data points and the red line (—) is the theory fit. $w_0^2(t) = w_0^2 + \Delta w_0^2/(1 + \tau_2/2t)$. $P = 7.19mW$.

By substituting $w_0^2(t)$ of Equation (4.9) into Equation (4.10) and solving for $n_2(t)$, we get

$$\begin{aligned} n_2(t) &= \Delta n(t)\frac{\pi w_0^2(t)}{2P} \\ &= -\frac{\alpha}{8\kappa}\frac{\partial n}{\partial T}\frac{w_0^2(t)}{1+\tau_1/2t} \\ &= -\frac{\alpha}{8\kappa}\frac{\partial n}{\partial T}\left[\frac{w_0^2}{1+\tau_1/2t}+\frac{\Delta w_0^2}{(1+\tau_1/2t)\,(1+\tau_2/2t)}\right], \end{aligned} \tag{4.11}$$

where τ_1 and τ_2 are the time constants of $\Delta n(t)$ and $w_0(t)$, respectively. In general, τ_1 and τ_2 are not necessarily the same. To obtain $n_2(t_i)$ from $\Delta n(t_i)$, the peak intensity of a gaussian beam as a function of $w_0^2(t)$ is used in Equation (4.10), namely $I_p(t_i)$. In Figures 4.10 – 4.12, Equation (4.11) is the theory function used to fit the data and a $= -\frac{\alpha}{8\kappa}\frac{\partial n}{\partial T}$. The parameters, w_0 and Δw_0 found in Figures 4.7 – 4.9 fixed and only τ_1 and τ_2 are used as parameters in fitting process of $n_2(t)$.

The two time constants, τ_1 and τ_2 are found to be almost identical. This implies that the time evolution of $w_0^2(t)$ follows the time dependence of $\Delta n(t)$. We assume that $w_0^2(t)$ behaves in the same manner as the on-axis temperature $\delta T(t)$ in Equation (4.6). If $n_2(t)$ is from a pure thermal lens effect, the assumption is consistent with the data for DB14.

Δn is proportional to the input beam power P with a negative constant of proportionality. On the other hand, n_2^{sat} or $n_2(t \to \infty)$ is proportional to $w_0^2 + \Delta w_0^2$, namely

$$n_2^{sat} = -\frac{\alpha}{8\kappa}\frac{\partial n}{\partial T}(w_0^2 + \Delta w_0^2). \tag{4.12}$$

Note that Different combinations of beam waist and power can yield the same intensity. Table 4.4 shows that case 3 has smaller n_2^{sat} than case 1 and 2 even though case 3 has a larger intensity with a smaller beam waist than case 1 and 2, which is corresponding to Equation (4.11) when $t \to \infty$. The relationship between n_2^{sat} and w_0 related to the thermal conductivity will be discussed in Section 4.1.7. When we increase the size of the beam waist from $35.11\mu m$ (case 3) to $65.06\mu m$ (case 1 and 2), the time constant increases from

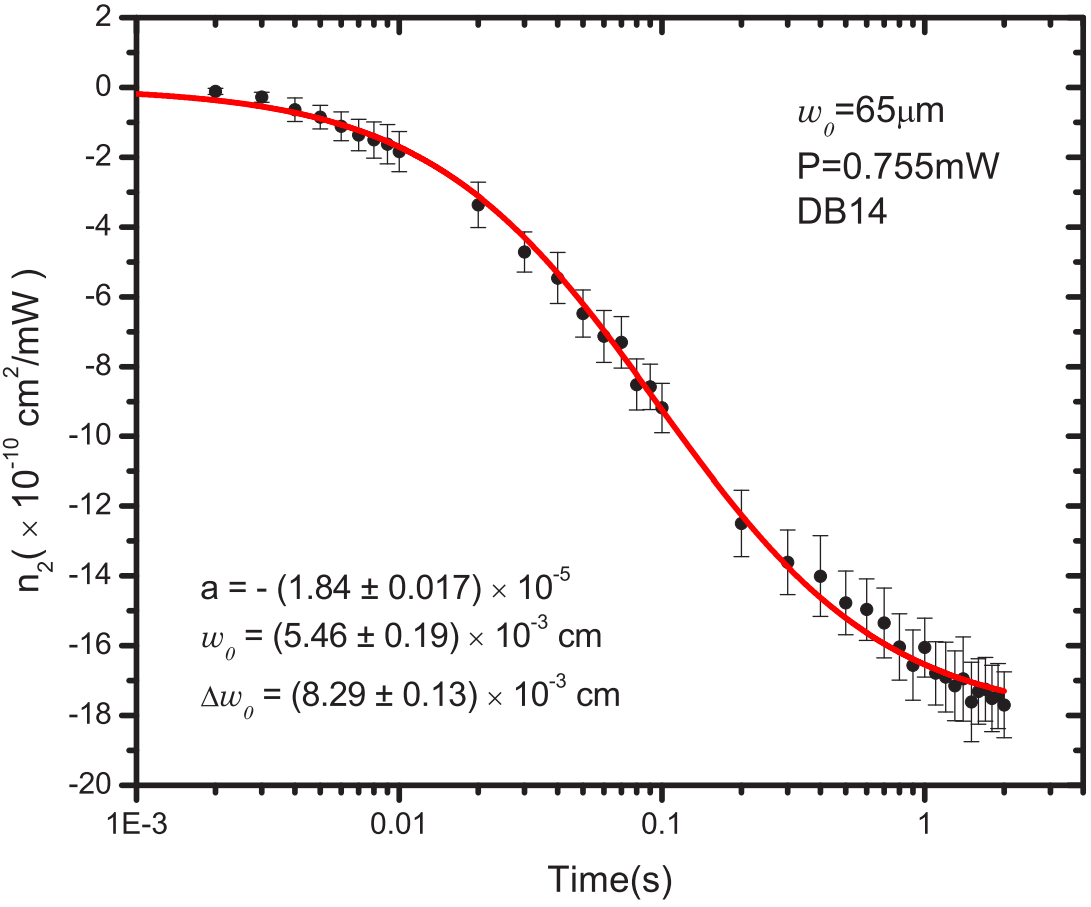

Figure 4.10: Nonlinear refractive index as a function of time for DB14. The measured initial beam waist is 65 μm. Power is 0.755mW. Points (•) are data and line (—) is for our thermal lens model. $n_2^{sat} = -(18.13 \pm 0.12) \times 10^{-10} cm^2/mW$ and $\tau = (19.2 \pm 0.5) \times 10^{-2} s$.

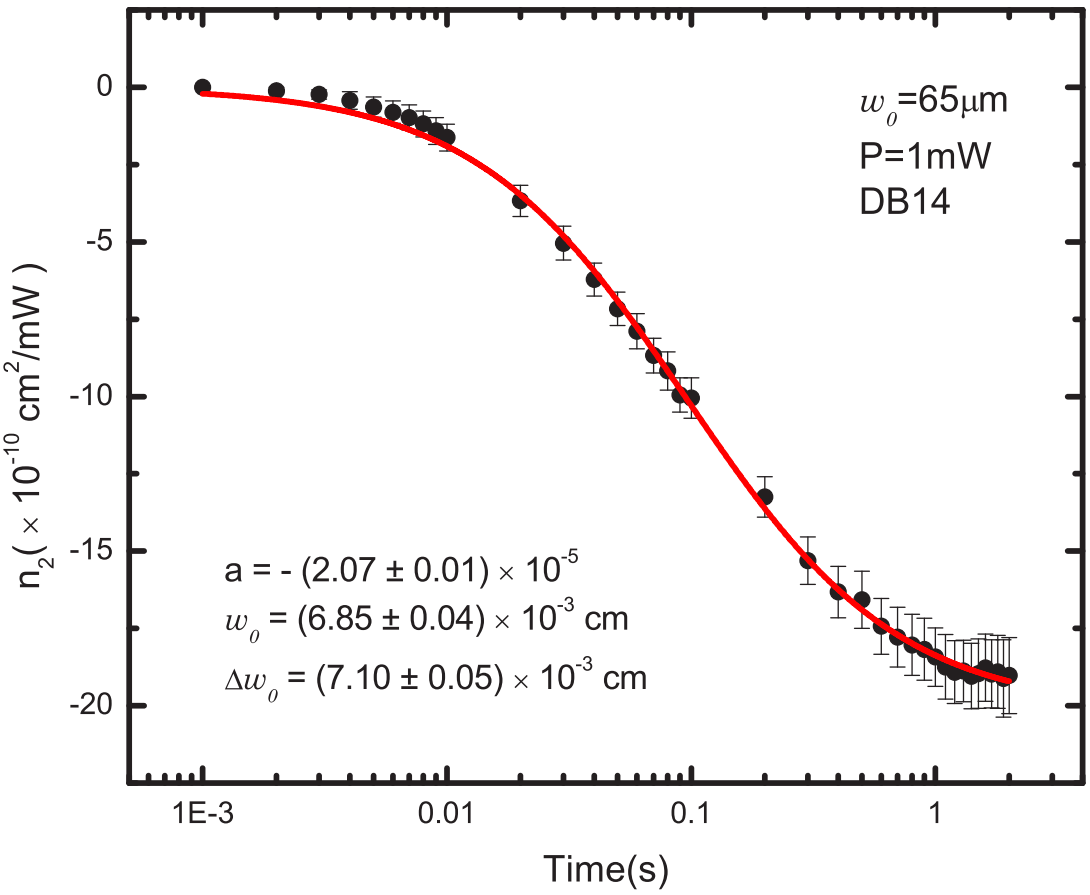

Figure 4.11: Nonlinear refractive index as a function of time for DB14. The measured initial beam waist is 65 μm. Power is 1mW. Points (•) are data and line (—) is for our thermal lens model. $n_2^{sat} = -(20.13 \pm 0.08) \times 10^{-10} cm^2/mW$ and $\tau = (19.1 \pm 0.4) \times 10^{-2} s$.

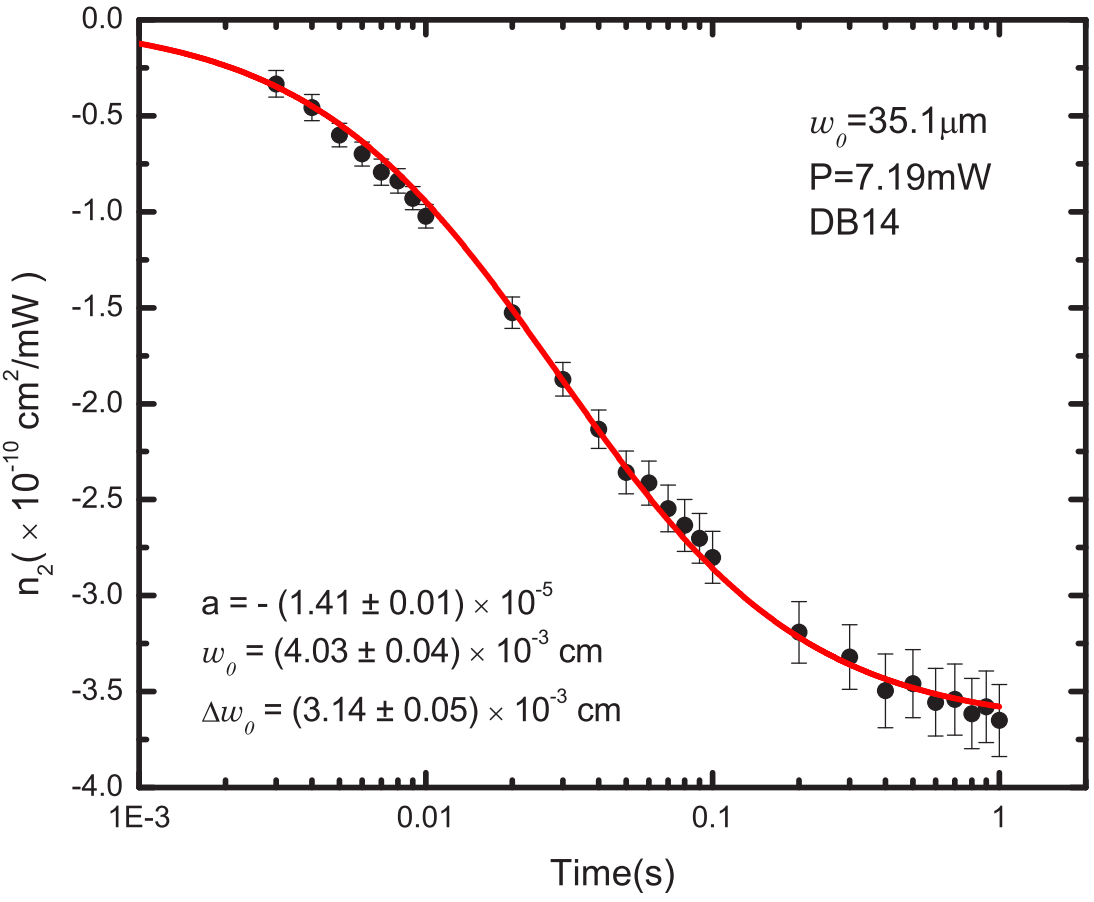

Figure 4.12: Nonlinear refractive index as a function of time for DB14. The measured initial beam waist is 35.1 μm. Power is 7.19mW. Points (•) are data and line (—) is for our thermal lens model. $n_2^{sat} = -(3.68 \pm 0.02) \times 10^{-10} cm^2/mW$ and $\tau = (5.77 \pm 0.14) \times 10^{-2} s$.

$Power(mW)$	$w_0(\mu m)$	$n_2^{sat}(\times 10^{-10} cm^2/mW)$	$\tau(10^{-2}s)$
0.755	65.06	-18.13 ± 0.12	19.2 ± 0.5
1	65.06	-20.13 ± 0.08	19.1 ± 0.4
7.19	35.11	-3.68 ± 0.02	5.77 ± 0.14

Table 4.4: Parameters from fits for the nonlinear refractive index of the thermal lens effect for PMMA/DB14 (0.022 wt. %). The data and fits are shown in Figure 4.10 – 4.12.

$5.97s$ (case 3) to $19.1s$ (case 2) and $19.2s$ (case 1). This still hold the quadratic relationship between the size of the beam waist and the time constant, such that $\tau^{exp} \propto w_0^2 + \Delta w_0^2$.

4.1.7 Thermal conductivity

The on-axis temperature change is obtained in Section 4.1.5 as follows:

$$\delta T = \frac{\alpha P}{4\pi\kappa\,(1 + \tau/2t)}. \tag{4.13}$$

In the limit of $t \to \infty$, the saturated δT is given by

$$\delta T^{max} = \frac{\alpha P}{4\pi\kappa}, \tag{4.14}$$

which is independent of time constant. As such, an analysis using δT^{max} is not affected by discrepancies between experimental and theoretical values of τ.

For data analysis, since the change of refractive index is linearly proportional to the change of temperature, so δT^{max} is obtained from the experimental value of Δn_{sat} by

$$\delta T^{max} = \left(\frac{\partial n}{\partial T}\right)^{-1} \Delta n_{sat}, \tag{4.15}$$

where Δn_{sat} is obtained from Figures 4.4 – 4.6 and $\frac{\partial n}{\partial T}$ is given in Table 4.2. Figure 4.13 shows δT^{max} as a function of power. The thermal conductivity is obtained from a linear fit to Equation (4.14). Figure 4.13 shows a comparison of κ of PMMA [10] and our dye-doped polymer sample. Since the dye concentration is as small (0.022 wt. %), the thermal

Parameter	Literature[10]	Literature[11]	Figure 4.13	Figure 4.14
$\kappa(W/m \cdot K)$	0.193	0.16 ± 0.03	0.226 ± 0.011	0.167 ± 0.007

Table 4.5: The comparison of parameters.

conductivity of dye-doped polymer should be approximately equal to the value for pure PMMA.

Recall that Equation (4.11) includes the effective minimum beam waist as a function of time. In the limit of $t \to \infty$, the maximum value of n_2 is related to $w_0^2 + \Delta w_0^2$ as follows:

$$n_2^{max} = -\frac{\alpha}{8\kappa}\frac{\partial n}{\partial T}\left(w_0^2 + \Delta w_0^2\right). \tag{4.16}$$

Figure 4.14 shows another way to find the thermal conductivity by using the linear relationship between $|n_2^{max}|$ and $w_0^2 + \Delta w_0^2$ with $\frac{\alpha}{8\kappa}\frac{\partial n}{\partial T}$ as the slope. κ is obtained from the slope of the graph by substituting α and $\frac{\partial n}{\partial T}$ from the literature, as summarized in Table 4.2. We get a result that is comparable to the literature value[10]. This result supports our theory which includes the effective minimum beam waist. Table 4.5 shows the value of κ from the literature and from our work.

4.1.8 Discrepancy of the time constants

In Section 4.1.4, a discrepancy between the theoretical and experimental time constants is observed. τ^{exp} is about 10 times larger than τ^{theory}, where from Section 2.3.2,

$$\tau^{theory} = \frac{\rho c}{4\kappa} w_0^2. \tag{4.17}$$

In Sections 4.1.6 and 4.1.7, we proposed that $w_0(t)$ should be modified to include a time dependent effective minimum beam waist. By substituting Equation (4.9) into Equation (4.17), our theory for the time constant can be generalized to

$$\tau = \frac{\rho c}{4\kappa}\left[w_0^2 + \Delta w_0^2/(1 + \tau/2t)\right]. \tag{4.18}$$

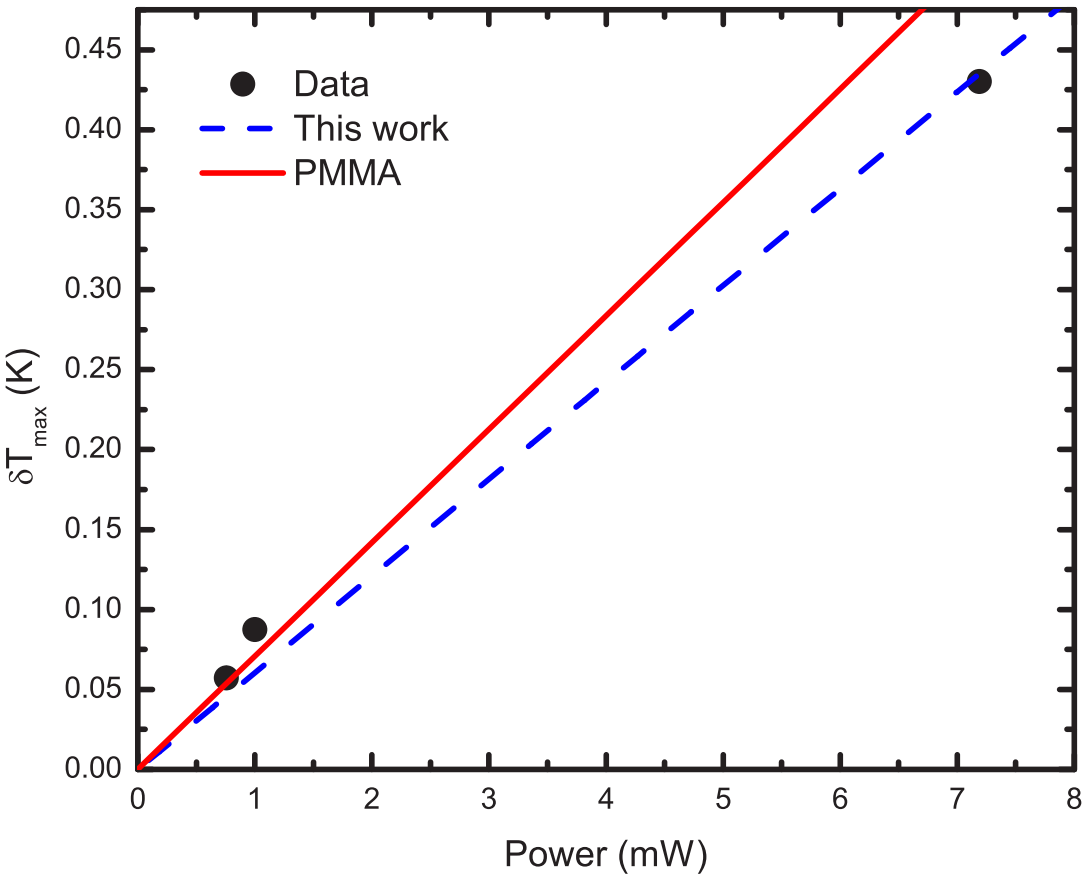

Figure 4.13: The saturated temperature as a function of input power. The points (•) are the data points and the red line (—) is the theory, $\delta T_{max} = \frac{\alpha P}{4\pi\kappa}$ with $\kappa = 0.193 W/m \cdot K$. The blue dashed line(- - -) is for $\kappa = 0.226 \pm 0.011 W/m \cdot K$, which is obtained from a linear fit to Equation (4.14).

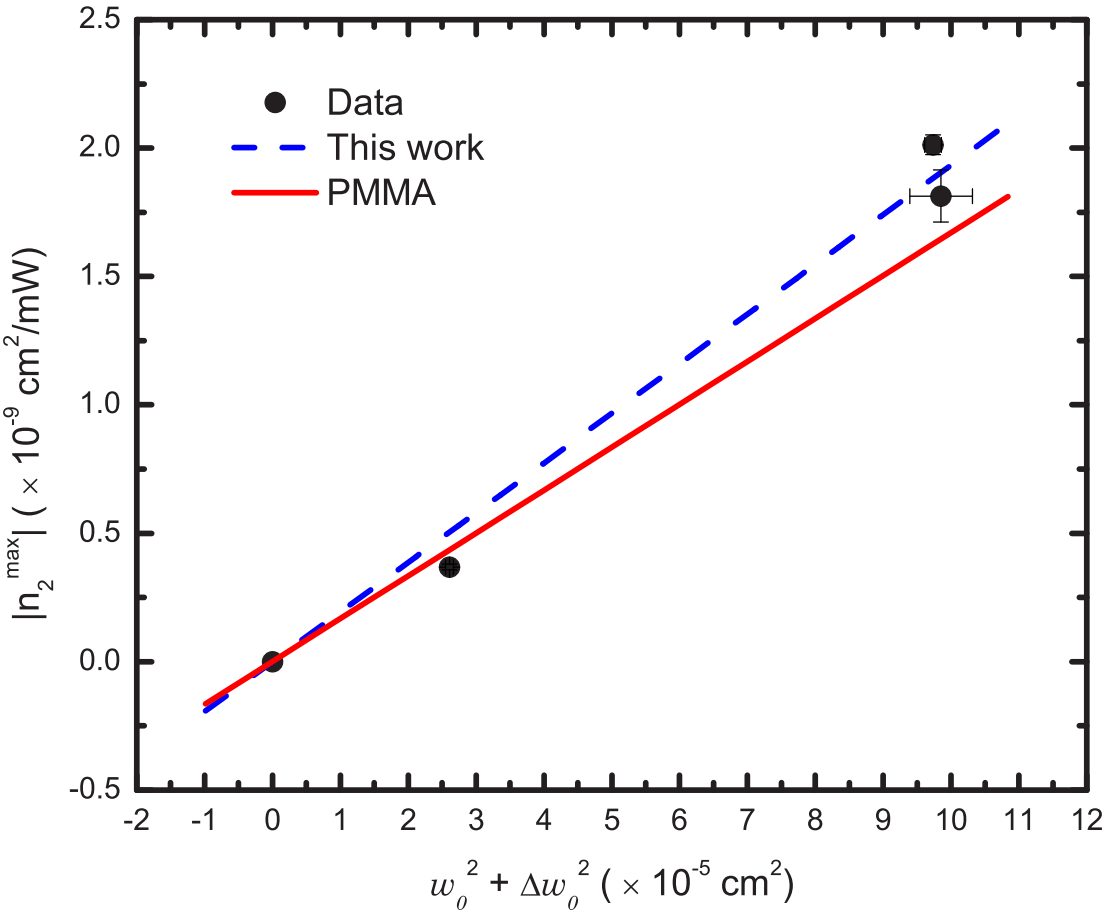

Figure 4.14: The maximum value of n_2 is proportional to the square of effective beam waist, $w_0^2 + \Delta w_0^2$. The points (•) are the data and the red line (—) is for κ from Reference [10]: the slope, $\frac{\alpha}{8\kappa}\frac{\partial n}{\partial T}$ with $\kappa = 0.193 W/m \cdot K$, and the blue dashed line(- - -) is with $\kappa = 0.167 \pm 0.007 W/m \cdot K$, which is from the linear fit to the data.

As a result, the time constant τ is not a constant but a function of time. But, in the limit of $t \to \infty$, the time constant approaches:

$$\tau^{sat} = \frac{\rho c}{4\kappa}\left(w_0^2 + \Delta w_0^2\right). \tag{4.19}$$

In Section 4.1.7, κ is obtained by two different methods independent of the values of ρ and c. The error range of κ is not enough to explain the discrepancy when using Equation (4.17). However, by substituting the condition $w_0 \sim \Delta w_0$ found in Section 4.1.5, a factor of two is obtained in the saturated value of τ:

$$\tau^{sat} = \frac{\rho c}{4\kappa} 2w_0^2 = 2\tau^{theory}. \tag{4.20}$$

As such, the only unknown parameter from the experimental results is the specific heat which must be 4-5 times larger than that in reference[10] to explain the discrepancy between τ^{theory} and τ^{exp}. It is unlikely that the literature value of the specific heat is that inaccurate.

We propose that the discrepancy is due to assumptions about the air-sample interface. In our theory, heat dissipation at the boundary of the sample is not considered. Due to the insulating effect of the air, it would take more time for the sample to reach thermal equilibrium. Figure 4.15 shows a schematic representation of how heat transfers at the boundary. The time delay of the heat transfer would explain the remaining discrepancy of the time constant between theory and experiment.

4.1.9 Summary for DB14/PMMA

From experiments with DB14, our findings are:

1. The effective minimum beam waist increases as a function of time due to the pho-

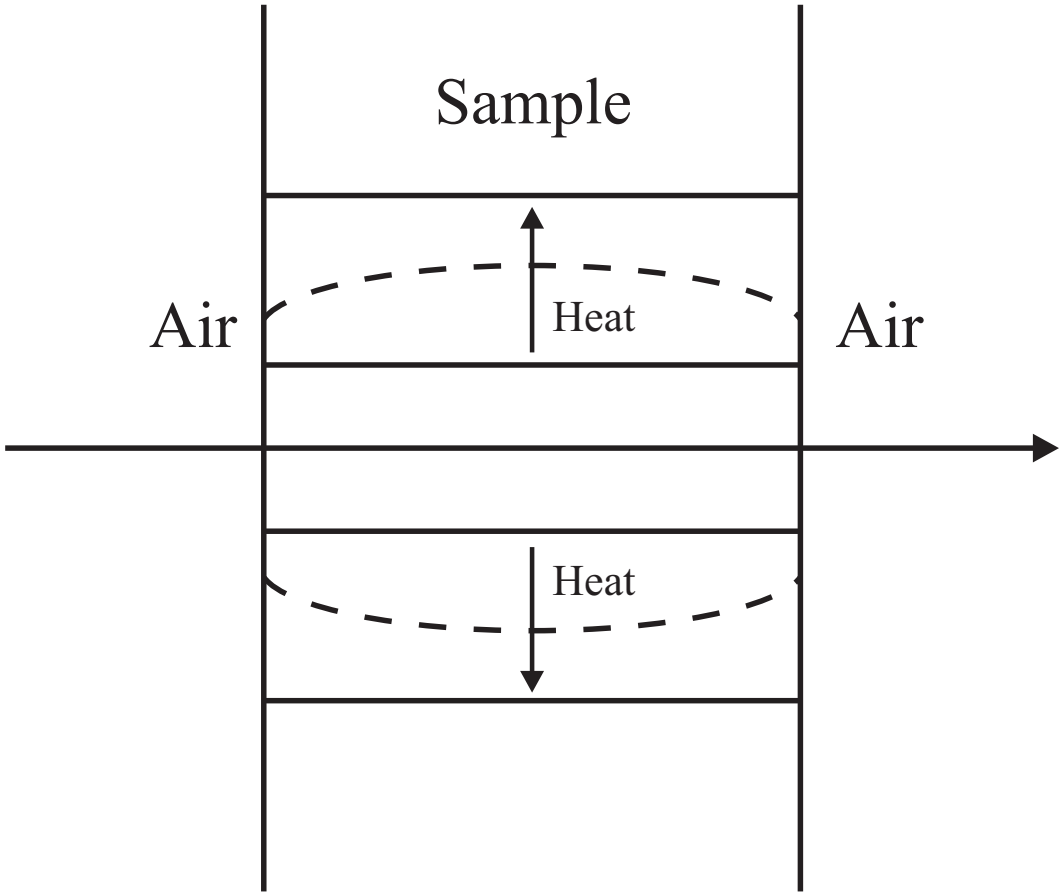

Figure 4.15: Heat transferring delays due to the air contact at the boundary.

tothermal lens effect as follows:

$$w_0^2(t) = w_0^2 + \frac{\Delta w_0^2}{1 + \tau/2t}, \tag{4.21}$$

where the experiment suggests that $w_0 \sim \Delta w_0$. Consequently, the saturated effective beam waist is related to the initial beam waist, namely $w_0^f \sim \sqrt{2} w_0$.

2. The nonlinear refractive index, n_2 is a quadratic function of the beam waist as follows:

$$n_2(t) = -\frac{\alpha}{8\kappa}\frac{\partial n}{\partial T}\left[\frac{w_0^2}{1 + \tau_1/2t} + \frac{\Delta w_0^2}{(1 + \tau_1/2t)(1 + \tau_2/2t)}\right], \tag{4.22}$$

where τ_1 is the time constant of $\Delta n(t)$ and τ_2 is the time constant of $w_0^2(t)$. The condition that $\tau_1 = \tau_2$ is obtained experimentally from a fit of the theory to the data.

3. The thermal conductivity, κ is obtained by using Result 1 (See Figure 4.14). This support that our modification for the second term in $w_0^2(t)$ is correct. Comparison of the thermal conductivity, κ in PMMA[10] [12] and DB14/PMMA was made (See Table 4.5).

4. A discrepancy between the theoretically predicted time constant and the experimental value was observed. We conclude that this effect originates from our theory's neglect of the sample/air interface.

4.2 Thermal effect and photoisomerization in DR1/PMMA

In Section 4.1, it was shown that the photothermal lens effect is the dominant nonlinear optical effect in DB14/PMMA when the excitation wavelength is off-resonance. Although the absorption coefficient of DB14/PMMA is as small as 1.72 cm^{-1}, it is enough to act as a heat source in the sample.

In this section, TZ-scan is performed in DR1/PMMA under similar conditions (beam

waist, intensity, and linear absorption coefficient) used for DB14/PMMA. To understand the photothermal contribution to n_2 in DR1/PMMA, the analytical results determined for DB14/PMMA under similar conditions is used.

4.2.1 TZ-scan fit

Figure 4.16 shows the absorption spectrum of 2 wt. % disperse red 1 doped PMMA (DR1/PMMA). The inset shows the molecular structure of DR1. The off-resonance wavelength of $647nm$ is used for the TZ-scan and as described in Section 4.1.2, the normalized transmittance of the Z-scan run is obtained as shown in Figure 4.17 at 40ms, 100ms, 1s, and 3s as an example. The beam waist measured without the sample using a knife edge is $40.87 \pm 0.41\mu m$.

As expected, the peak to valley amplitude increases as a function of time. At short times, the systematic noise level is large enough to show as error bars. On the other hand, as the amplitude of the transmitted signal gets larger, the noise level becomes small compared to the transmittance making the error bars smaller than the data points. Consequently, the theory fits better as time increases.

We use the effective minimum beam waist as a parameter for the fitting process in Figure 4.17 as described for the DB14 case. An increase of the effective beam waist is associated with broadening of the peak and valley, increase in the distance between peak and valley, and a sign of nonlocal photothermal heating as presented in Section 4.1.5.

One common assumption of Z-scan experiments is that the Rayleigh length is larger than the thickness of the sample. In case of a thick sample ($L > z_0$), the separation of the peak and the valley is observed without broadening of peak and valley.[13] In our work, we used large beam waists so that the Rayleigh length is larger than the thickness of our sample ($L < z_0$) to keep the assumption valid.

In the fitting process, the effective beam waist in the sample ($w_0(t)$), the on-axis phase change at the focal point ($\Delta\Phi_0(t)$), and the center point ($z_c(t)$) are obtained as parameters

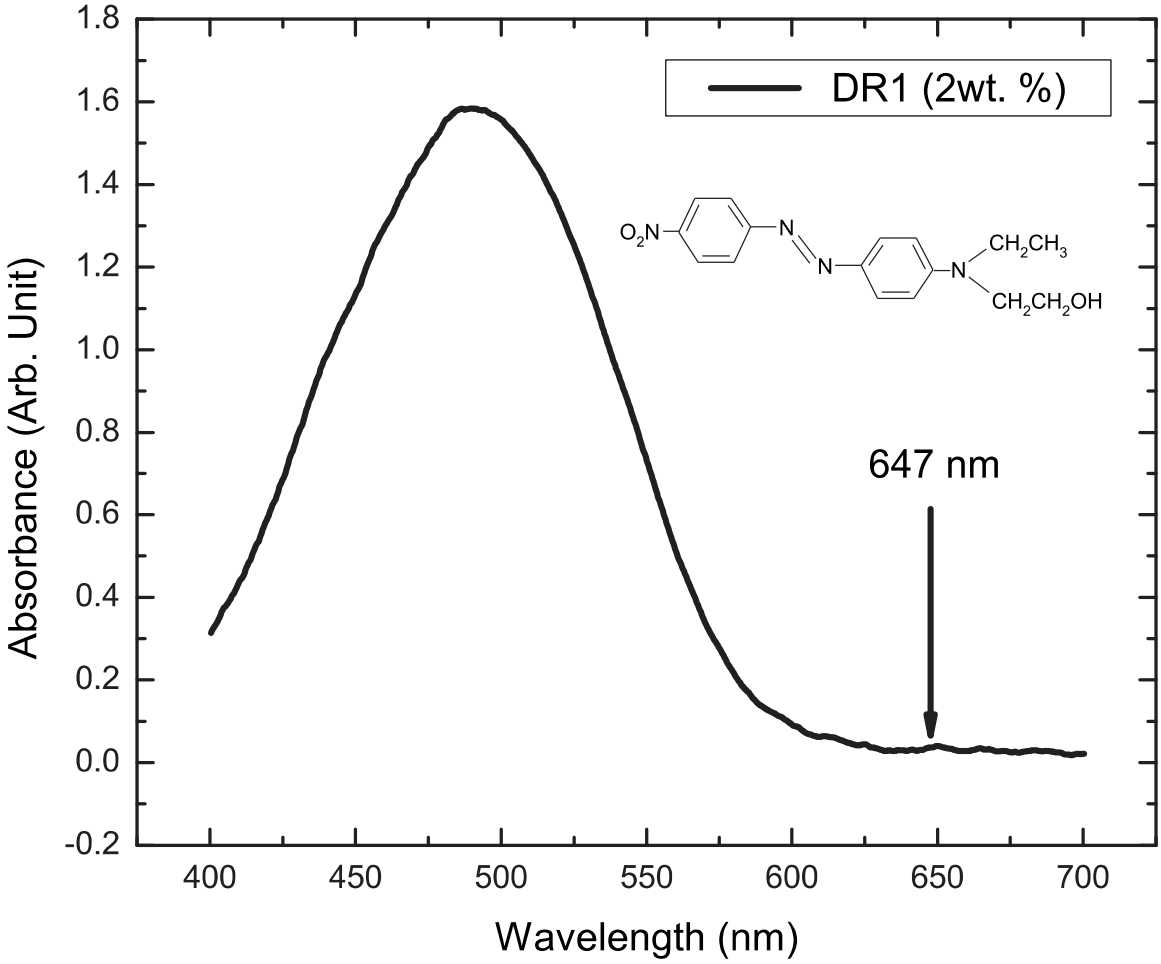

Figure 4.16: Absorption spectrum of DR1 (2 wt.%). The inset is the molecular structure of DR1. $\lambda = 647nm$ is the wavelength used in the TZ-scan experiment.

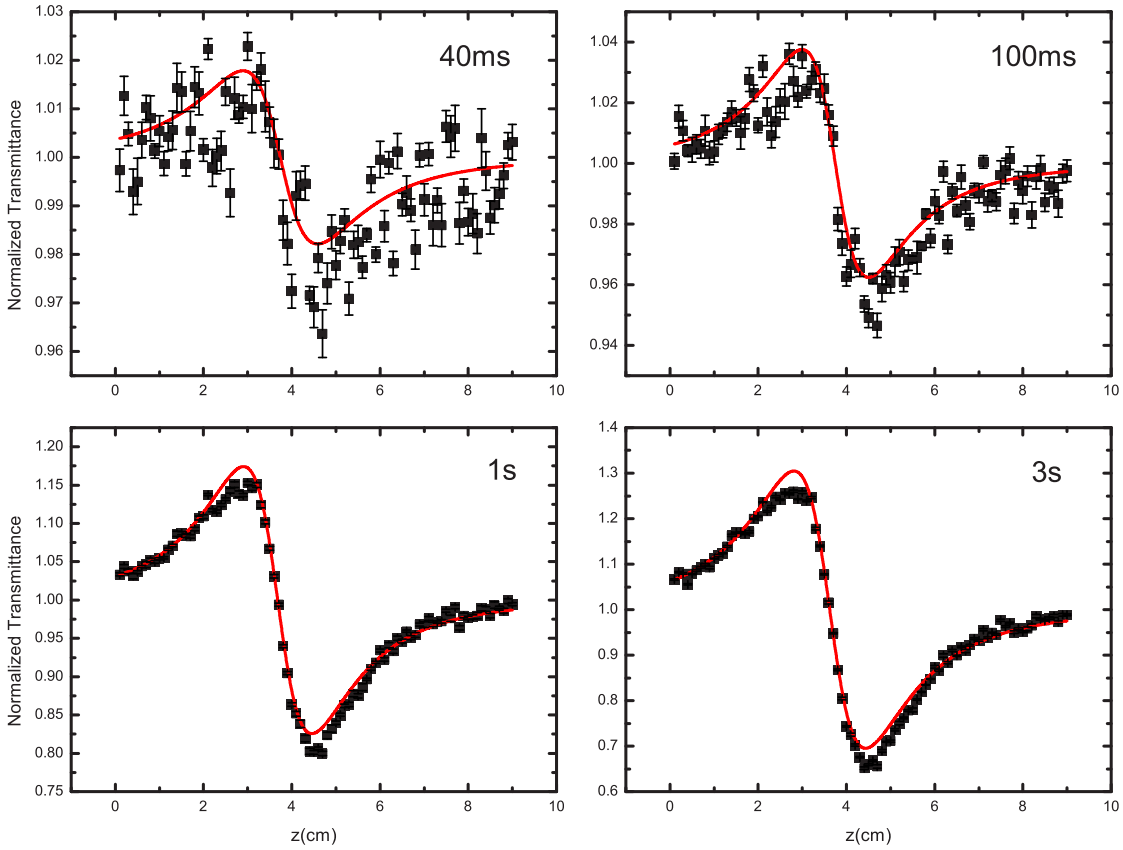

Figure 4.17: TZ-scan for DR1 at different time snapshots. The beam waist measured without the sample is $40.87 \pm 0.41 \mu m$. The input power of the beam is $0.033 mW$.

	DB14/PMMA	DR1/PMMA
$\alpha(cm^{-1})$	1.72 @457 nm	5.63 @647 nm; 5.06 @633nm
$w_0(\mu m)$	35.11; 65.06	40.87; 70.83
P (mW)	0.755; 1; 7.19	0.033; 0.055; 0.11; 0.168; 0.22

Table 4.6: Experimental conditions for DR1/PMMA and DB14/PMMA

in the same manner as for DB14/PMMA.

4.2.2 The effective minimum beam waist

Recalling that the thermal lens effect originates from the heat source through the linear absorption coefficient, a similar behavior of w_0 as a function of time is expected in DR1 so that $w_0^2(t) = w_0^2(0) + \Delta w_0^2/(1 + \tau/2t)$ with the assumption that dye at a concentration of 2 wt. % is not enough to change the thermal properties of the host polymer (PMMA).

Large off-resonant nonlinearity is reported for DR1/PMMA when measured by four wave mixing.[14] Intensities are chosen to be about 10 times lower than used in DB14 to avoid higher order nonlinearities. Since the nonlinear refractive index for the thermal lens effect depends on the beam waist rather than the intensity, it is valid to use lower the intensities to test the nonlinear refractive index of the thermal lens effect in DR1/PMMA. Table 4.6 shows that the parameters are comparable in each sample. Both samples have a small concentration of chromophore so that the thermal properties should be similar.

Figure 4.18 and Figure 4.19 show how $w_0(t)$ changes as a function of time. Figure 4.18 shows $w_0(t)$ with a small initial beam waist of $40.87 \pm 0.41\mu m$ for $P = 0.033, 0.055, 0.11,$ and $0.22\ mW$ with linearly and circularly polarized beam. Figure 4.19 shows $w_0(t)$ with a large initial beam waist of $70.83 \pm 0.49\mu m$ when $P = 0.168mW$ with linearly and circularly polarized beam. For both linearly and circularly polarized light, $w_0(t)$ is the same within experimental uncertainty.

The initial beam waist before nonlinear refraction turns on is an important factor for the thermal nonlinear refractive index since $w_0 \sim \Delta w_0$. The magnitude of the effective minimum beam waists for DR1/PMMA are not as large as those found for DB14/PMMA under similar

conditions. The increase of the effective beam waist is about $5\mu m$ in Figure 4.18 and 4.19, which is smaller the 40% increase found in DB14/PMMA.

This implies that there is no photothermal lensing in DR1/PMMA. Where is the thermal lens effect? Why does the minimum beam waist change so little? Is the photothermal heating mechanism different in some fundamental way from DB14/PMMA? Those questions will be answered in Section 4.3.

4.2.3 Time-dependent of δn for linearly and circularly polarized beam from TZ-scan

According to the theory we developed, the change of the refractive index parallel to the pump beam polarization is given by Equation (2.72),

$$\begin{aligned} \Delta n_{\parallel} &= \frac{2\pi N}{n^0_{PMMA}} \left\{ T_0(t)\bar{\alpha}^t \left(1 + 2r^t T_2(t)\right) \right. \\ &\quad \left. + \left(1 - T_0(t)\right) \bar{\alpha}^c \left(1 + 2r^c C_2(t)\right) - \bar{\alpha}^t \right\}, \end{aligned} \tag{4.23}$$

where T_0 and C_0 are the number of trans and cis isomers normalized to unity, and T_2 and C_2 are the second order parameters for each kind. Since we use a single beam in this TZ-scan, the pump and probe are the same beam so the parallel component is measured.

A TZ-scan is performed with two different beam waists with a linearly and with a circularly polarized beam. Figure 4.20 shows the refractive index changes for a linearly polarized beam with $w_0 = 40.87\mu m$. The parameters obtained from the best fits are shown in Table 4.7. Figure 4.21 shows the refractive index changes as a function time for a circularly polarized beam with $w_0 = 40.87\mu m$. Table 4.8 shows the parameters obtained from the best fits in Figure 4.21.

In the thermal lens effect for DB14, the change of refractive index from the thermal effect is related to the beam waist. Therefore, a TZ-scan for a larger beam waist is also performed to study how the beam waist affects the results. Figure 4.22 shows data of $\Delta n(t)$ and fits

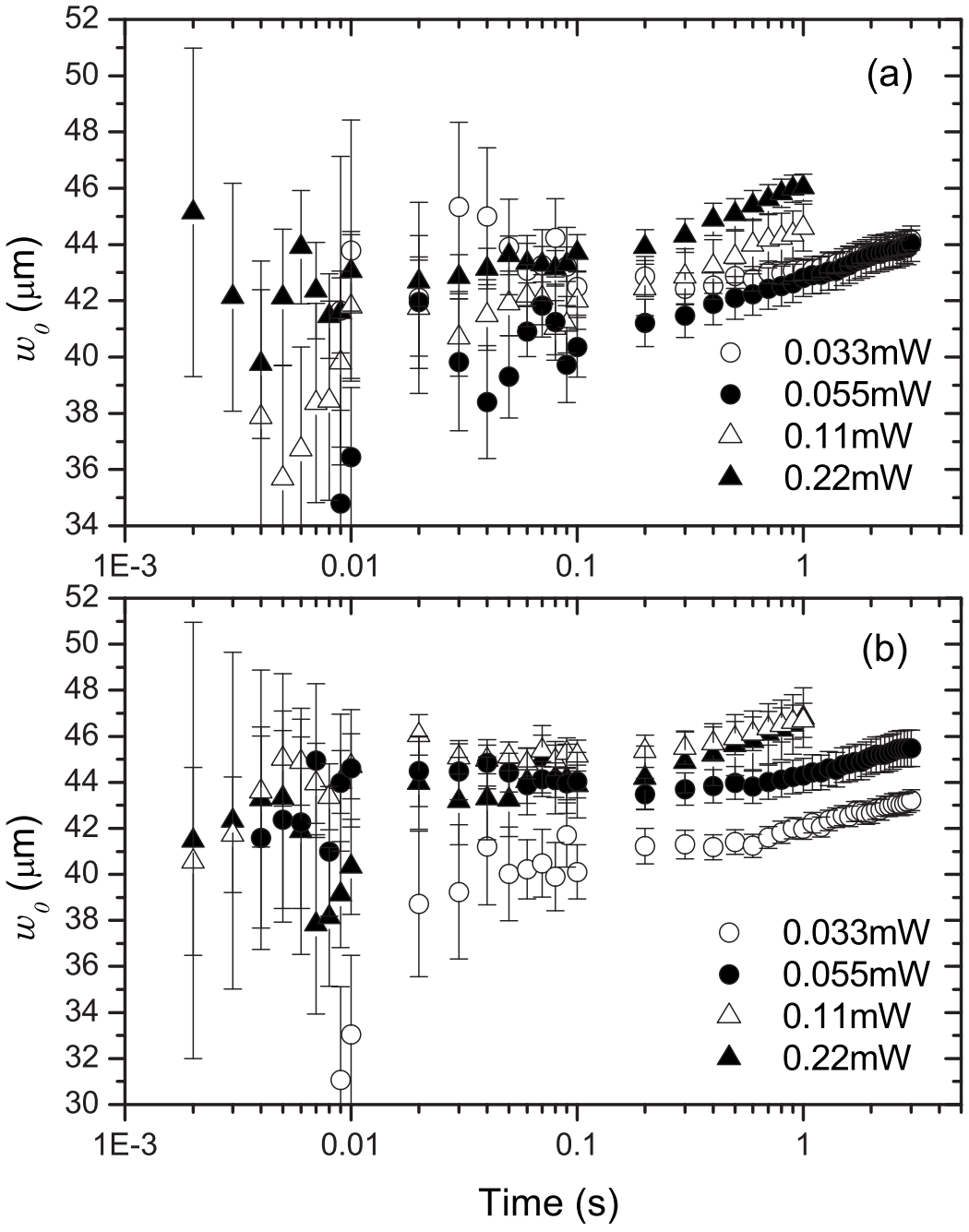

Figure 4.18: Minimum beam waists measured by TZ-scan. (a) Linearly polarized beam and (b) Circularly polarized beam. For both (a) and (b), the measured minimum beam waist without the sample is $40.87 \pm 0.41 \mu m$.

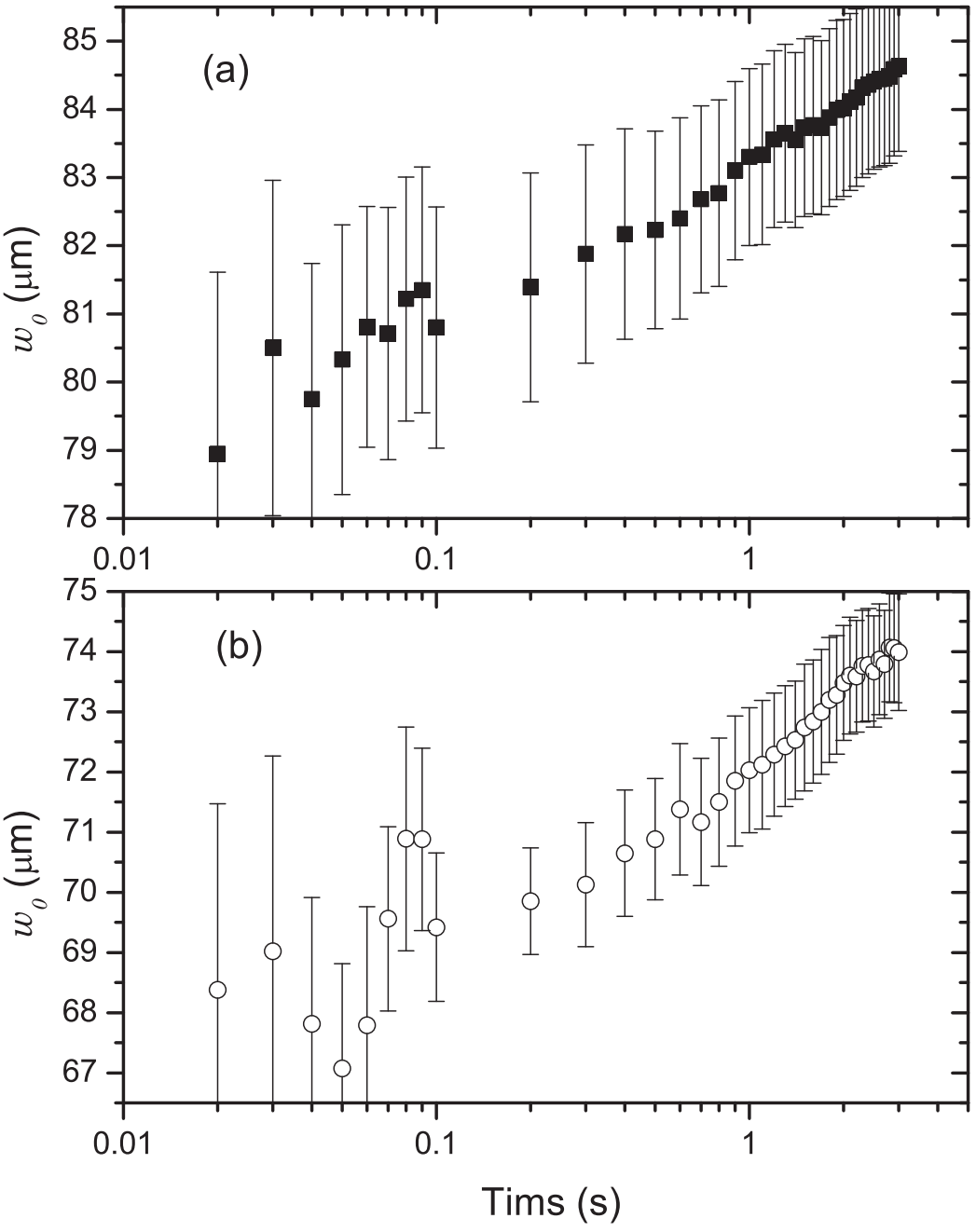

Figure 4.19: Effective minimum beam waists measured by TZ-scan. (a) Linearly polarized beam and (b) Circularly polarized beam. For both (a) and (b), the measured minimum beam waist without the sample is $70.83 \pm 0.49 \mu m$.

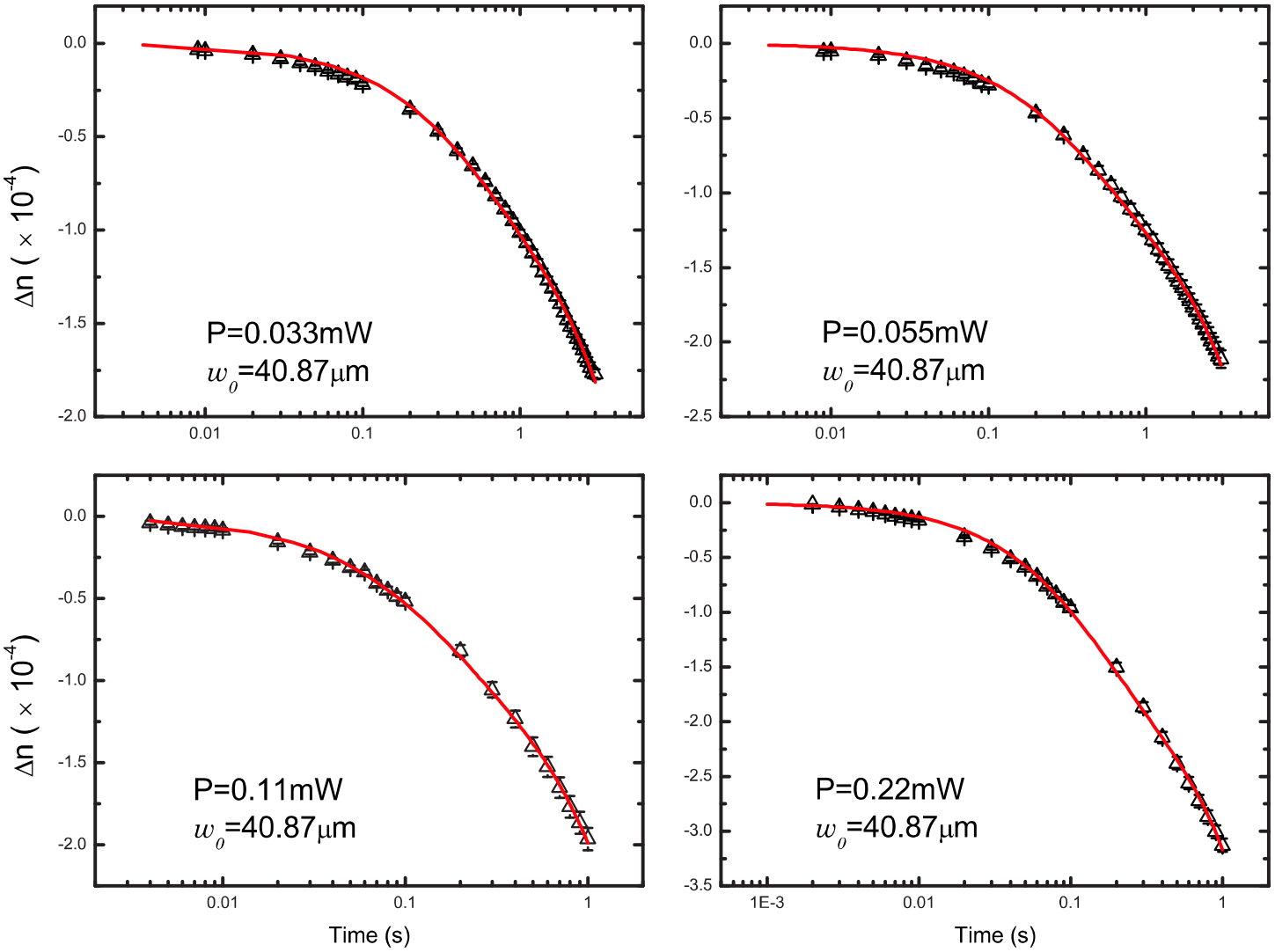

Figure 4.20: Change in refractive index, Δn as a function of time for linearly polarized light in DR1/PMMA for data (△) and theory (—).

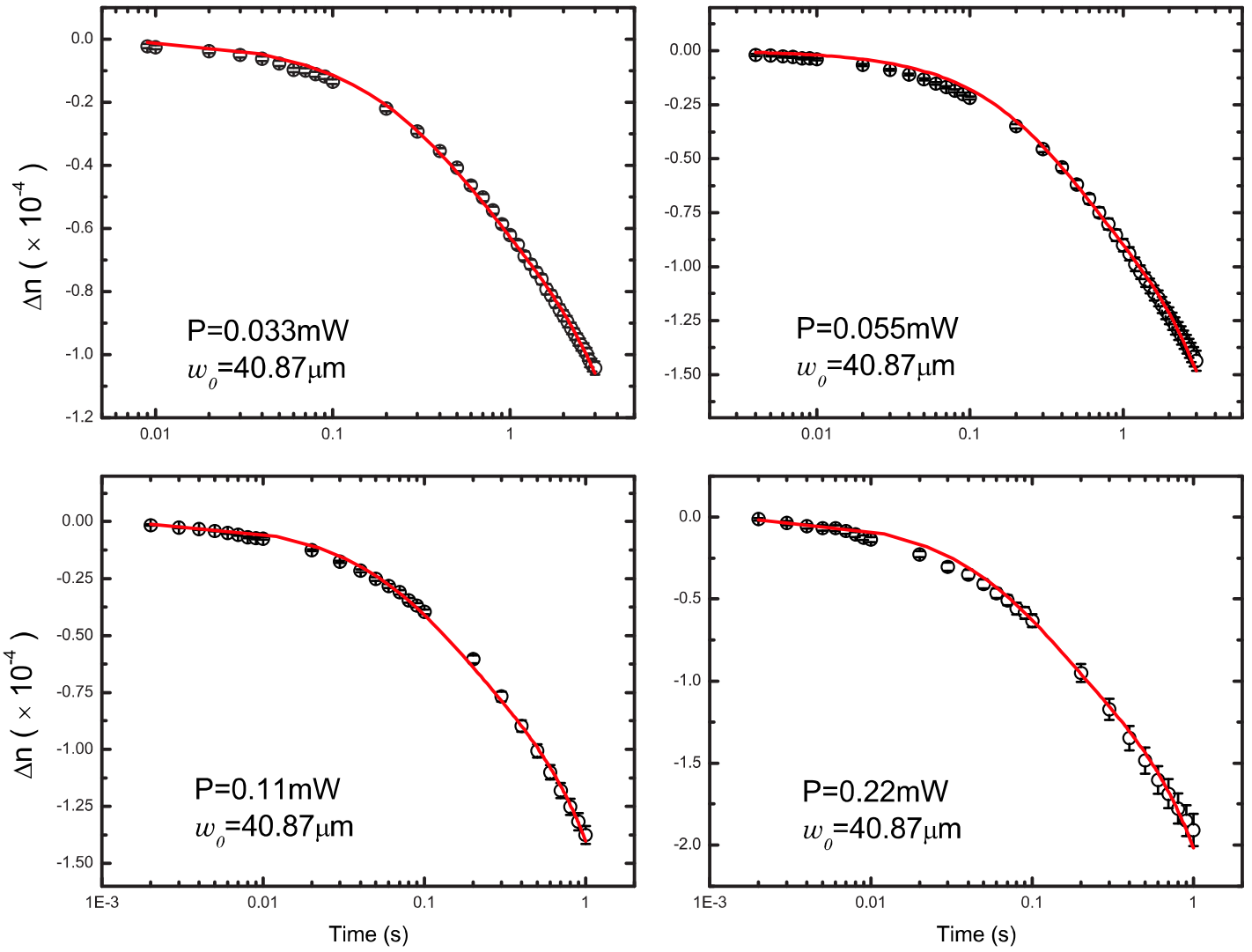

Figure 4.21: Change in refractive index, Δn as a function of time for circularly polarized light in DR1/PMMA for data (◯) and theory (—).

P (mW)	0.033	0.055	0.11	0.22	0.168
$w_0(\mu m)$	40.87	40.87	40.87	40.87	70.83
$\zeta_t(\times 10^{-25} J \cdot s)$	3.04 ± 0.3	4.22 ± 0.4	3.05 ± 0.3	5.81 ± 0.6	11.60 ± 1.2
$\phi_{tc}(\times 10^{-2})$	3.20 ± 0.27	2.39 ± 0.14	3.30 ± 0.26	2.43 ± 0.21	2.39 ± 0.14
r^t	0.84 ± 0.06	0.93 ± 0.05	0.86 ± 0.06	1 ± 0.07	1.00 ± 0.06
$\phi_{tc} r^t(10^{-2})$	2.69 ± 0.42	2.22 ± 0.25	2.84 ± 0.42	2.43 ± 0.38	2.39 ± 0.28

Table 4.7: Parameters used in fitting n_2 for linearly polarized beam.

P (mW)	0.033	0.055	0.11	0.22	0.168
$w_0(\mu m)$	40.87	40.87	40.87	40.87	70.83
$\zeta_t(\times 10^{-25} J \cdot s)$	3.02 ± 0.3	4.30 ± 0.43	2.66 ± 0.27	4.76 ± 0.5	11.61 ± 1.2
$\phi_{tc}(\times 10^{-2})$	1.62 ± 0.15	1.44 ± 0.13	2.15 ± 0.20	1.61 ± 0.20	1.32 ± 0.18
r^t	0.89 ± 0.08	1 ± 0.07	0.93 ± 0.07	1 ± 0.08	1 ± 0.1
$\phi_{tc} r^t(\times 10^{-2})$	1.44 ± 0.26	1.44 ± 0.23	2.00 ± 0.34	1.61 ± 0.33	1.32 ± 0.31

Table 4.8: Parameters used in fitting n_2 for circularly polarized beam.

for a linearly and a circularly polarized beam with $w_0 = 70.83 \mu m$. The parameters obtained for the best fits are shown in Table 4.7 and 4.8.

4.2.4 Physical behavior of the parameters from fit

In Section 4.2.3, the refractive index change, $\Delta n(t)$ as a function of time was found to fit the theory that we developed in Section 2.4.2. In this section, the contribution of each parameter and its physical meaning is presented.

In Equation (4.23), the order parameters are a complicated function of intensity, time, and temperature (from photothermal effect or globally controlled by an oven). Due to the complicated functions we need to analyze, Origin C (version 7.5) used to fit the data. (See Appendix 4.4)

The increase in the refractive index due to the addition of DR1 dye in its trans state into the polymer is given by,

$$n^0_{DR1} = \frac{2\pi N}{n^0_{PMMA}} \bar{\alpha}^t. \tag{4.24}$$

Since isomerization from the trans to the cis state leads to a decrease of the refractive index, the largest possible index change for photoisomerization in $\Delta n < n^0_{DR1}$. For example, if n^0_{DR1}

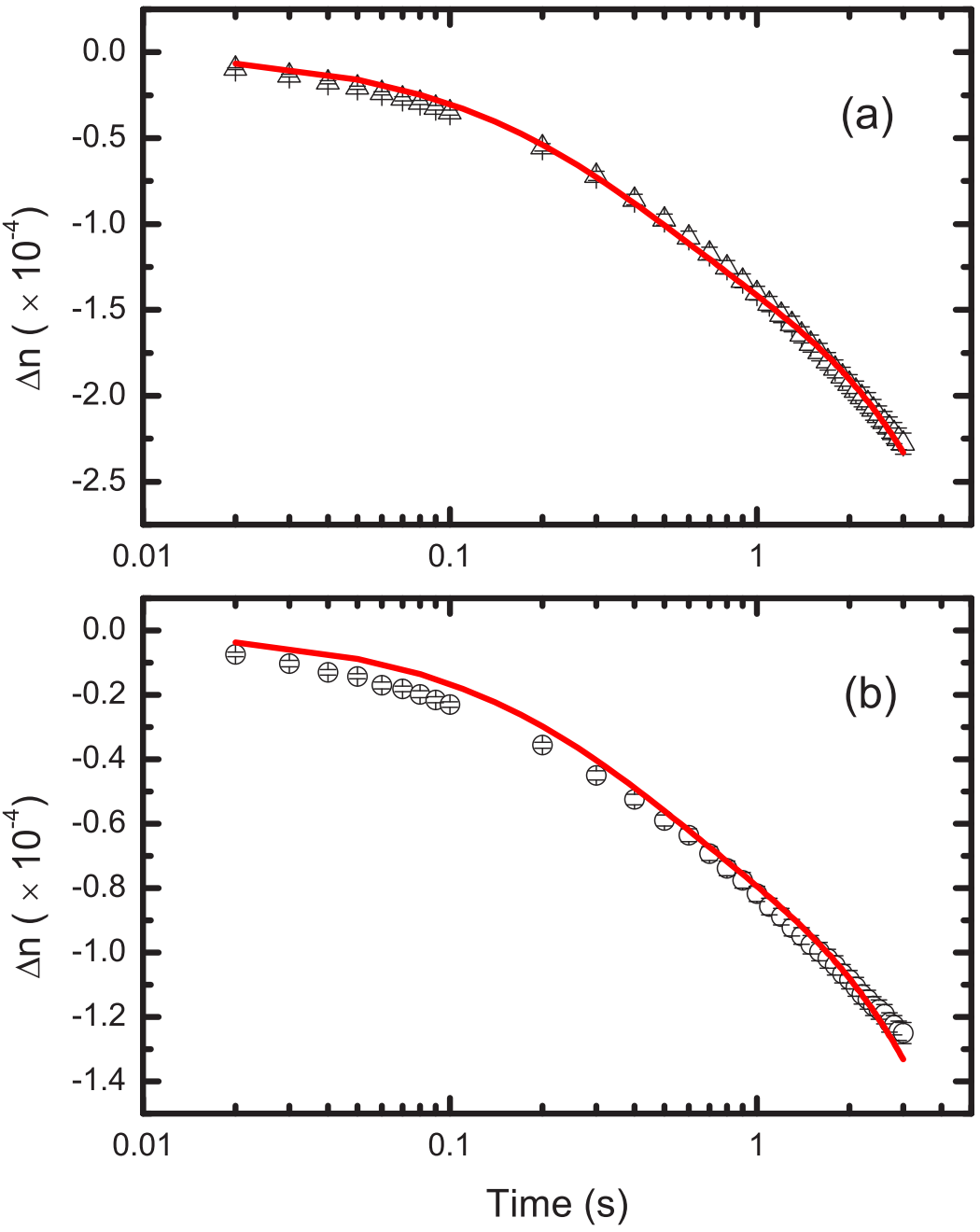

Figure 4.22: The nonlinear refractive index as a function of time after the beam is turned on for DR1. $P = 0.168mW$ and $w_0 = 70.83\mu m$. (a): Linearly polarized beam, (b): Circularly polarized beam. Lines (–) are the theoretical fits.

were on the order of 10^{-3}, our theory for $\Delta n(t)$ would necessarily be consistently below the data even for a perfectly linear molecule ($r^t = 1$) and ideal quantum yield ($\phi = 1$). On the other hand, when n^0_{DR1} is on the order of 10^{-2}, our theory fits observation as presented in the previous section. Since $\Delta n(t)$ is obtained from the change of $\chi^{(1)}$ as a function of time, the limiting condition is self-consistent. The order of magnitude (10^{-2}) agrees with the literature[15]. As such, by controlling the parameter of n^0_{DR1} in Equation (4.24), it is possible to test the validity of our theory.

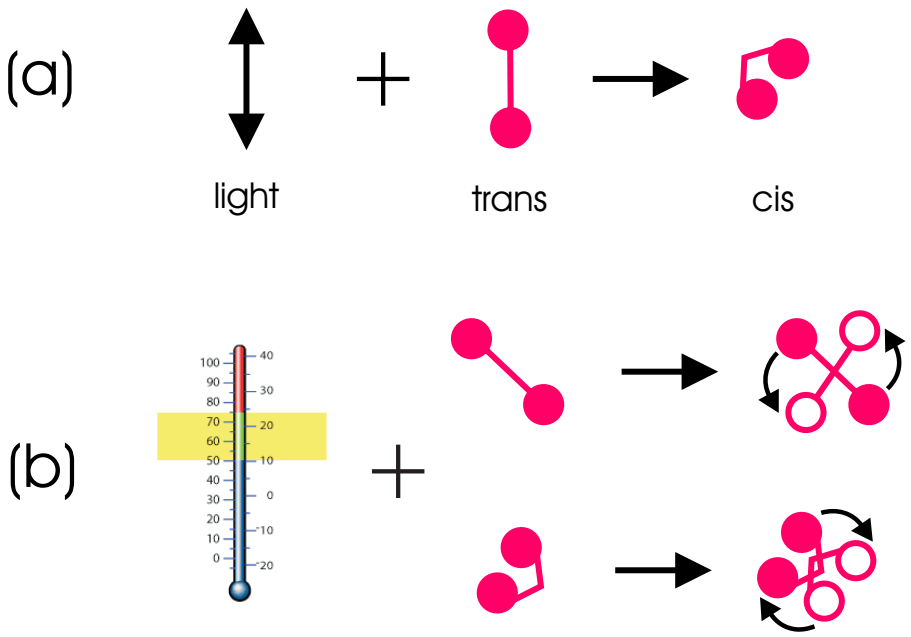

Figure 4.23: (a) Photoisomerization and (b) Photothermal diffusion.

4.3 Mechanisms

In the previous section, the theory of time-dependent Δn was presented and compared with data for various intensities, power, and beam waist.

In this section, we will discuss the physical meaning of the parameters in detail as follows:

- Quantum yield ϕ and molecular anisotropy r as a polarization-dependent local effect.
- Rotational friction ζ_r or viscosity η related to non-polarization-dependent nonlocal photothermal diffusion.

Figure 4.23 shows photoisomerization and photothermal diffusion mechanisms. Figure 4.23 (a) represents photoisomerization which increases anisotropy of the sample by angular hole burning. On the other hand, Figure 4.23 (b) represents photothermal diffusion, which randomizes the orientation of molecules. There are two methods to introduce temperature-dependent mechanisms: One is from the light source as a heat source through optical linear absorption. The other method is to control the temperature externally and globally.

4.3.1 Photoisomerization

The molecular anisotropy is defined by

$$r^{t,c} = \frac{\sigma_{\parallel}^{t,c} - \sigma_{\perp}^{t,c}}{\sigma_{\parallel}^{t,c} + 2\sigma_{\perp}^{t,c}}. \tag{4.25}$$

When a molecule is close to being 1-D such as a linear molecule ($\sigma_{\perp} \to 0$), $r \to 1$. On the other hand, when a molecule is a symmetric 2-D one such as a circularly-shaped molecule ($\sigma_{\parallel} \sim \sigma_{\perp}$), $r \to 0$. According to the fit to the data, the anisotropy of the trans-isomer, r^t is close to unity which means the molecule is approximately 1-D. On the other hand, r^c for the cis-isomer is in order of 10^{-4} which means the molecular shape is nearly circular.

The ratio of $r^t\phi_{tc}$ for circularly to linearly polarized light, namely $C\left(r^t\phi_{tc}\right)/L\left(r^t\phi_{tc}\right)$, for various intensities are shown in Figure 4.24. The average of the ratio is 0.62 ± 0.03. $C\left(r^t\phi_{tc}\right)/L\left(r^t\phi_{tc}\right)$ is equal to ϕ_{tc}^C/ϕ_{tc}^L since the molecular shape of a trans isomer, which determines r^t, is independent of light polarization. ϕ_{tc}^C and ϕ_{tc}^L are the quantum efficiencies of an absorbed photon for converting the molecule from trans to cis for circular and linear polarization, respectively.

To explain why ϕ_{tc} is larger for a linearly than for a circularly-polarized beam, we approximate the trans-isomer as a rod and the cis-isomer as a ring or disk. The moment of inertia for the trans isomer is $\frac{1}{12}ML^2$, where M is the mass and L is the length of the trans-isomer. The moment of inertia for a disk is $\frac{1}{2}MR^2$, where R is the radius of the disk. Figure 4.25 shows how the length of trans molecule is related to the radius of the cis molecule assuming that the circumference of the cis molecule is the length of trans molecule. Thus, $R = \frac{L}{2\pi}$. According to the fit of the data to the theory, the length of cis isomer is about 1/3 of that of trans isomer although the theoretical estimation counting azobenzene part only gives us 0.55 in Section 2.8.3 Appendix C. Using the model in Figure 4.25, the moment of inertia of trans molecule is about 6 times larger than cis molecule for a disk shape and about 3 times larger than the cis molecule in the ring shape. A circularly polarized photon can transfer

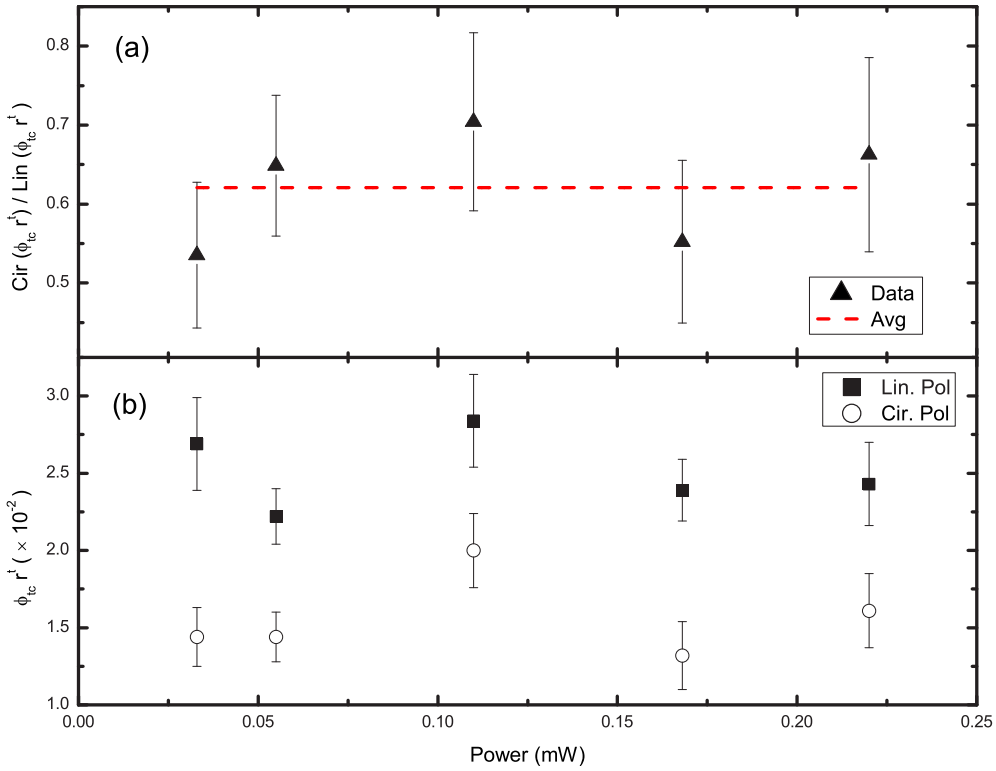

Figure 4.24: (a) Ratio $\phi_{tc}r^t$ of circular to linear polarization and (b) $\phi_{tc}r^t$ for circular and linear polarization.

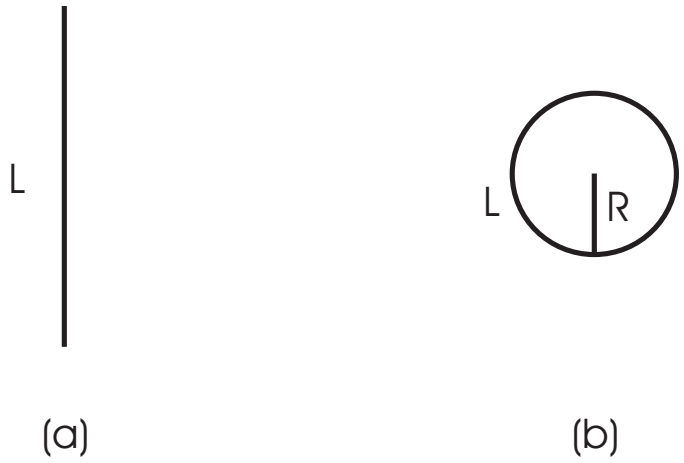

Figure 4.25: Molecular anisotropy suggested from fit parameters (a) linear-shaped trans molecule as a rod. (b) circular-shaped trans molecule as a disk or a ring.

angular momentum to an object more easily than a linear polarized photon.[16] Since the moment of inertia of trans-isomer is larger than that of cis-isomer, the angular momentum from a circularly polarized photon can be transferred to cis-isomers more easily than to a trans-isomers. In other words, incident circularly polarized photons are easily absorbed by circularly-shaped cis-isomers than absorbed by linear trans-isomers. As a result, the quantum yield of trans to cis transition, ϕ_{tc} for a circularly polarized beam is smaller than that for a linearly polarized beam.

Figure 4.26 shows the ratio of n_2^C/n_2^L as a function of time. Due to our new TZ-scan experiment, it is possible to show the ratio as a function of time. The common non-polarization dependent effect such as photothermal heating cancels when taking the ratio but polarization-dependent mechanisms are remain.

The magnitude of nonlinear refractive index depends on molecular anisotropy and quantum yield. Since the molecular anisotropy is an intrinsic property of a molecule, the quantum yield will determine the magnitude. The ratio of quantum yields agrees with the ratio of the nonlinear refractive index in Figure 4.26.

The ratio 2/3 and 1/4 are reported for nonresonant electronic nonlinearity and for molecular reorientation, respectively.[18] Since our experiments are performed with CW light source, the peak intensity is too low for Δn to originate from an electronic mechanism. The ratios observed in our experiment are not close to 1/4, which also means that in this time regime, photoisomerization more dominantly contributes to Δn than molecular reorientation. To be able to observe molecular reorientation, the exposure time scale would need to be much higher.

In limit of $t \rightarrow \infty$, the ratio of the nonlinear refractive index in disperse red 13 azo dye doped in PMMA is recently found to be 2/3[17], which agrees with our data. In the reference, angular hole burning model and HeNe laser were used, which is similar to our results.

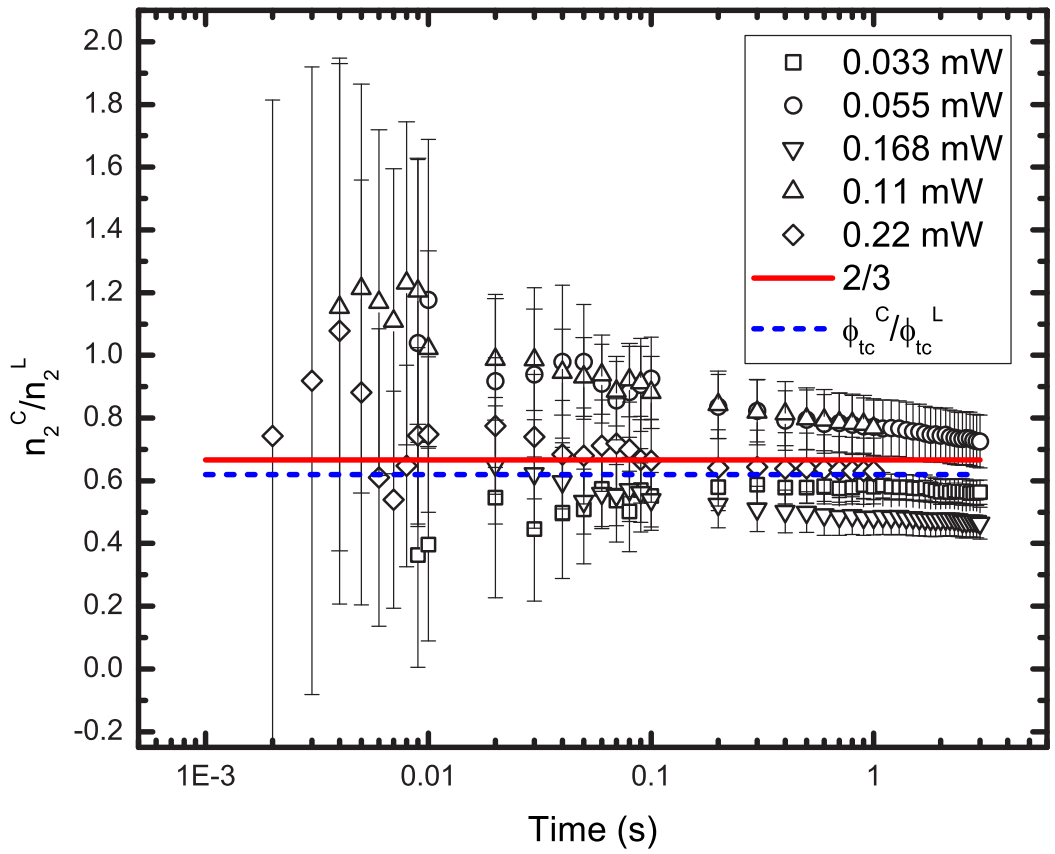

Figure 4.26: The ratio of n_2 as a function of time for different intensities. The value 2/3 (red solid line) is from a reference [17]. ϕ_{tc}^C/ϕ_{tc}^L (blue dashed line) is the value obtained from our data, 0.62 ± 0.03.

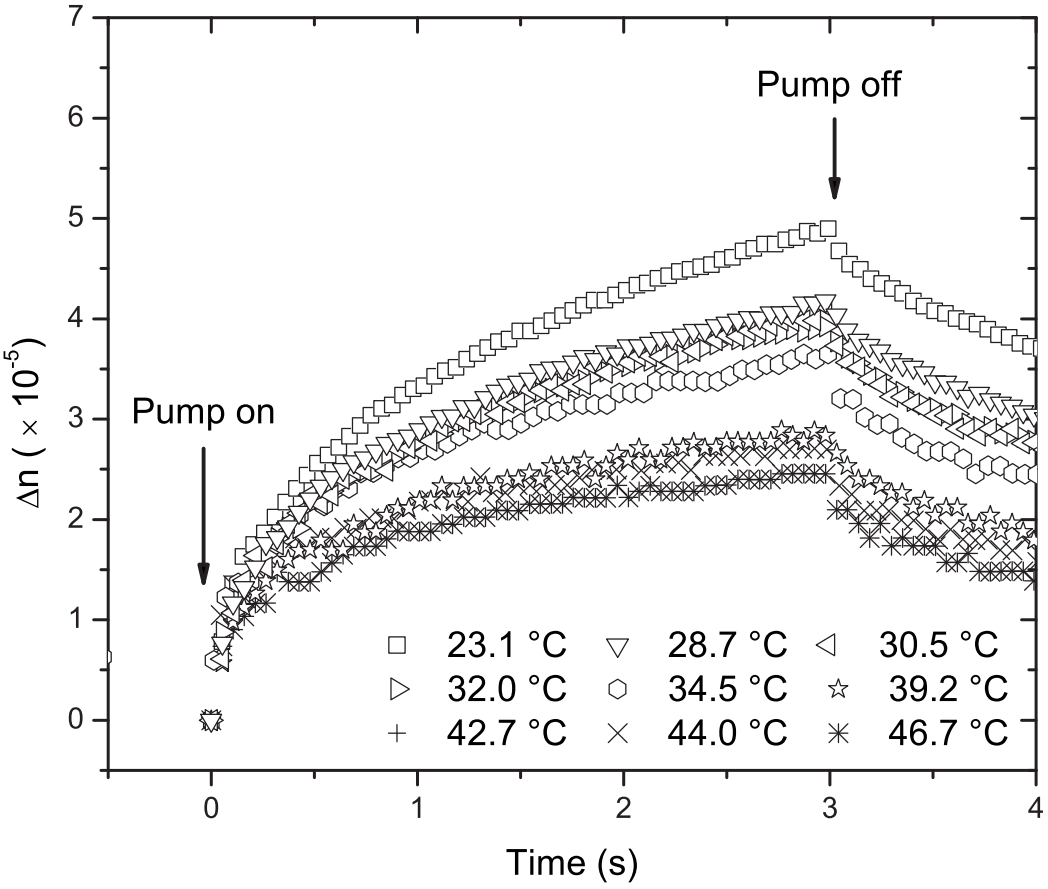

Figure 4.27: Temperature-dependent birefringence as a function of time with a 4 mW the pump beam.

4.3.2 Temperature dependent birefringence of DR1/PMMA

In DB14/PMMA, the thermal lens effect was found to be a nonlocal effect by observing the time-dependent effective 0minimum beam waist. In DR1/PMMA, the photothermal mechanism was convoluted with molecular rotational friction through the Einstein relation.

In this section, temperature-dependent birefringence of DR1/PMMA is measured. Thermal agitation can reduce molecular orientational order directly using a thermal bath.

Figure 4.27 shows the birefringence, Δn, as a function of time for selected temperatures. As the temperature of the sample increases, the transmittance decreases. The birefringence

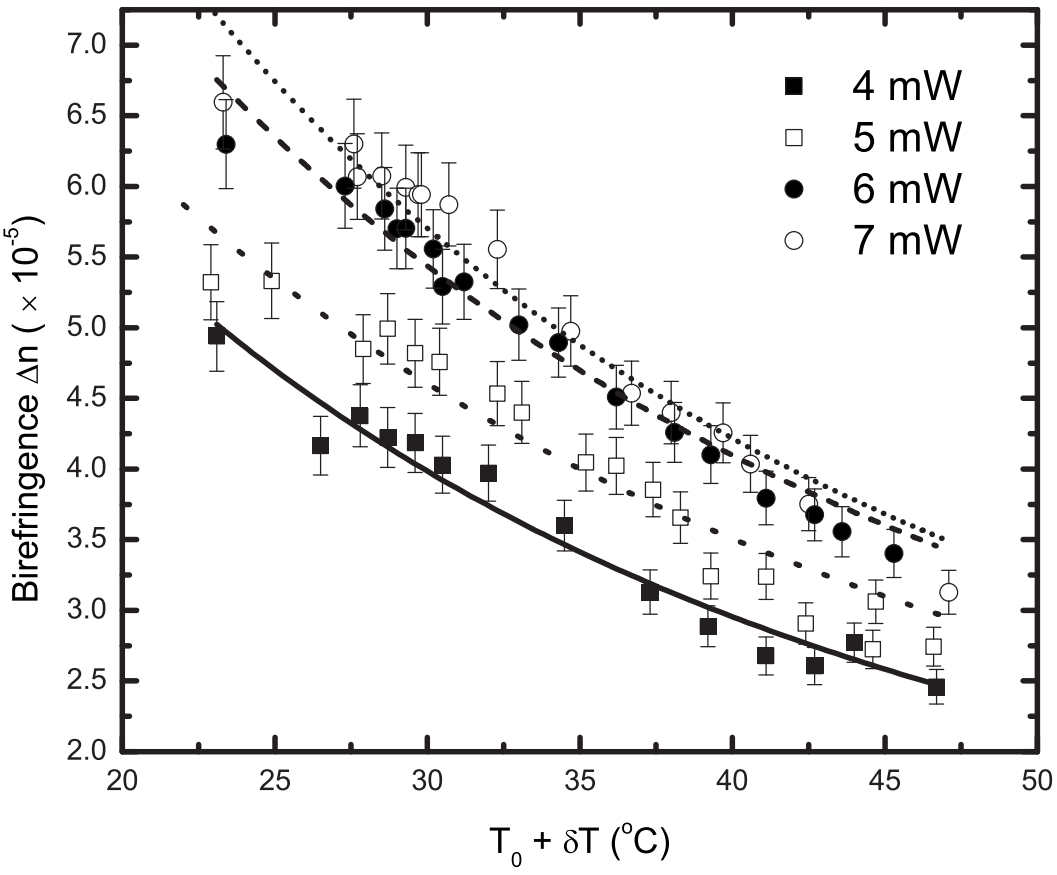

Figure 4.28: Birefringence as a function of temperature at $t = 3s$.

originates from an anisotropic molecular distribution. As temperature increases, the thermal agitation to the molecular orientation increases, which reduces the birefringence of the sample.

Figure 4.28 shows the birefringence when $t = 3s$ as a function of temperature. At each power of the pump beam, the birefringence decreases as temperature increases. T_0 is room temperature, about 22 to 25$°C$, and δT is difference between the temperature oven and room temperature. Although the temperature agitates the orientation of molecules, a larger birefringence is observed at higher intensity than at lower intensity. Our theory agrees the

decrease of birefringence at temperature for various optical input powers. Note that the temperature-dependence of the viscosity is ignored to simplify the theory.

4.3.3 Summary for DR1/PMMA

Our goal is to find how the thermal lens effect (a non-local effect) is related to photoisomerization (a local effect). By means of fitting the experimental time-dependent change of refractive index to our theory, the parameters related to those mechanisms were obtained.

For photoisomerization, the results are as follows:

- ϕ_{tc}^{C} is found to be smaller than ϕ_{tc}^{L} because the cis molecular shape is more sensitive to circularly polarized as can be understood in terms of angular momentum transfer to the molecules.

- $\phi_{tc}^{C}/\phi_{tc}^{L}$ is found to be 0.62 ± 0.03, which agrees with the time-dependence of n_2^C/n_2^L and the ratio from Reference[17] in the steady-state. Consequently, the ratio shows that the dominant mechanism in this time regime is photoisomerization.

Figure 4.29 shows the modified energy diagram based on our results. The time constant for cis $\Rightarrow$ trans transition due to the thermal relaxation is $3\frac{1}{2}$ hours.[19] Since our experimental time scale is one to 3 seconds, thermal relaxation, as shown by the dotted arrow (γ), can be ignored. The quantum yield from trans $\Rightarrow$ cis for a circularly polarized beam is marked with a dashed arrow implying a value smaller than that of the linearly polarized beam.

To understand the thermal lens effect separate from any other nonlinear optical effect, our experiments were done with a similar value of absorption coefficient for both DR1/PMMA and DB14/PMMA. The DB14/PMMA sample is prepared with the absorption coefficient $1.72cm^{-1}$ at 457 nm in close range to the absorption coefficient $5.63cm^{-1}$ at 647 nm of DR1/PMMA sample. According to our observation in Section 4.1, the time-dependent effective beam waist originating from the thermal lens effect in DR1/PMMA is small compared to DB14/PMMA.

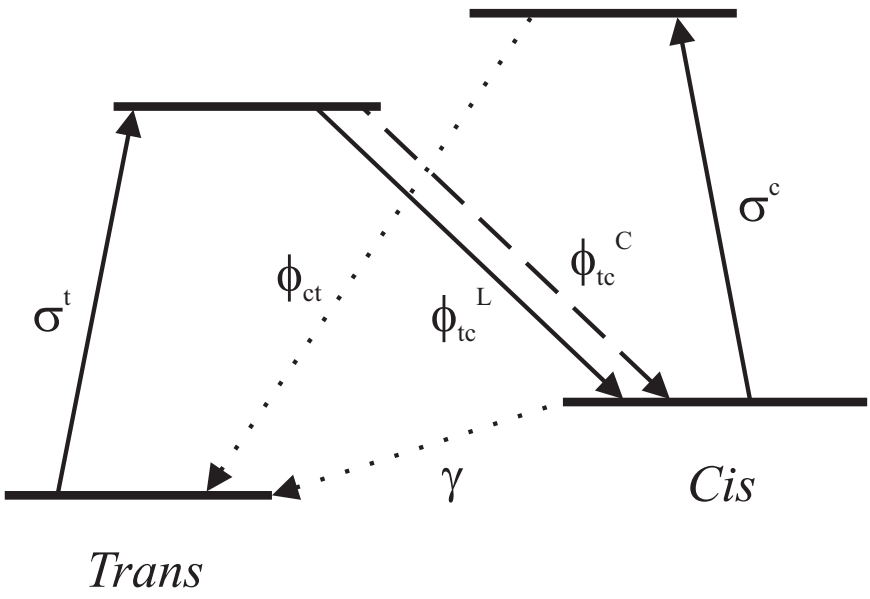

Figure 4.29: The modified energy diagram.

In DB14/PMMA, it is observed that the effective beam waist changes as a function of time, which is a nonlocal thermal effect. On the other hand, the dramatic effective beam waist change is not observed in DR1/PMMA implying mostly non-thermal local effect.

This result is peculiar because energy is being absorbed from the laser beam to the DR1 molecules; so, there must be a mechanism that stores this energy, releasing it as heat at a later time or the energy is radiated without generating heat. The longer time behavior of Figures 4.7 – 4.9 suggest such a time delay, which is beyond our measurement range.

One obvious source of energy storage is the ground state cis isomer, which has more energy than the ground state trans isomer. Since the cis lifetime is long, the heat will be given off at a later time. There are potentially other degrees of freedom that might lead to emission, such as fluorescence within the transparent window of the polymer composite. Such radiative and nonradiative processes may be quite complicated and treating them is beyond the scope of this dissertation.

The important conclusion is that the data shows either the storage of energy in an excited state of the system, which is later emitted as heat; or there are modes of de-excitation that

do not contribute to heat.

4.4 Appendix: Origin C code used for time-dependent Δn

```
#include <origin.h>


#define en 1
//linear polarization case;-0.5 for circular polarization

#define alp 0.00328
//alp is N \bar{\alpha}^{t} in Equation (4.18) and
//calculated to give n_{DR1}^{0} to be 0.01

#define k 0.00193
// thermal conductivity for PMMA (W/cm-K)

#define delt 5.63
//absorption coefficient for DR1 at 647nm in unit of 1/cm

#define rho 1.19*pow(10.,-3.)
//Density of PMMA (kg/cm^3)

#define cp 1.42*pow(10.,3.)
//specific heat of PMMA (J/kg-K)

#define n0 1.49
//linear refractive index of PMMA

#define kb 1.38*pow(10.,-19.)
//Boltzmann constant with length in cm unit (kg cm^2/s^2 /K)

//Define function T_0(t) here
double T_0(double x, double eta, double Lt, double p0, double a0, double phi_tc, double phi_ct,
double rt, double rc, double ra)
{

double y, Ip, tau,at, ac,at, ac, It, Ic, lamb_t, lamb_c, lamb_0,Dc, Dt;

tau=pow(a0,2.0)*rho*cp/(4.0*k);
//time constant defined without considering
//change of the beam waist because it's ignorable compared to DB14 case.

Dt=kb*delt*p0/(pow(pi,2.0)*eta*k*(1+tau/(2.0*x))*pow(Lt,3.0));
//angular diffusion constant of trans-isomer

Dc=kb*delt*p0/(pow(pi,2.0)*eta*k*(1+tau/(2.0*x))*pow(Lt/ra,3.0));
//angular diffusion constant of cis-isomer

Ip=2.0*p0/(pi*pow(a0,2.0));
//peak intensity of gaussian beam

It=0.51*phi_tc*Ip;
//phi_tc is quantum yield of trans to cis transition
//0.51 is obtained from the combination of one photon energy of 647nm
//and the absorption cross section of trans-isomer (See Equation (C-29, 30) in Ch. 2)

Ic=0.43*phi_ct*Ip;
//phi_ct is quantum yield of cis to trans transition
//0.43 is obtained from the combination of one photon energy of 647nm
//and the absorption cross section of cis-isomer (See Equation (C-29, 30) in Ch. 2)

lamb_0 = (It*(1.+4/5.0*pow(en*rt,2.) + 4/7.0*en*rt+6*Dt/It))/(2.0*(1+2/7.0*en*rt+3.0*Dt/It));
```

```
lamb_t = It*(1+4/7.0*rt+6.0*Dt/It);
lamb_c = Ic*(1+4/7.0*rc+6.0*Dt/It);
at=2/5.0*It*rt;
ac=2/5.0*Ic*rc;

y=exp(- lamb_0*x);

return(y);
}

//Define function T_2(t) here
double T_2(double x, double eta, double Lt, double p0, double a0, double phi_tc, double phi_ct,
double rt, double rc, double ra)
{

double y, Ip, tau,at, ac,at, ac, It, Ic, lamb_t, lamb_c, lamb_0,Dc, Dt;
tau=pow(a0,2.0)*rho*cp/(4.0*k);
Dt=kb*delt*p0/(pow(pi,2.0)*eta*k*(1+tau/(2.0*x))*pow(Lt,3.0));
Dc=kb*delt*p0/(pow(pi,2.0)*eta*k*(1+tau/(2.0*x))*pow(Lt/ra,3.0));
Ip=2.0*p0/(pi*pow(a0,2.0));
It=0.51*phi_tc*Ip;
Ic=0.43*phi_ct*Ip;
lamb_0 = (It*(1.+4/5.0*pow(en*rt,2.) + 4/7.0*en*rt+6*Dt/It))/(2.0*(1+2/7.0*en*rt+3.0*Dt/It));
lamb_t = It*(1+4/7.0*rt+6.0*Dt/It);
lamb_c = Ic*(1+4/7.0*rc+6.0*Dt/It);
at=2/5.0*It*rt;
ac=2/5.0*Ic*rc;
y=at/(lamb_t-lamb_0)*(exp(-lamb_t*x)-exp(-lamb_0*x));
return(y);
}

//Define C_2 function here
double C_2(double x, double eta, double Lt, double p0, double a0, double phi_tc, double phi_ct,
double rt, double rc, double ra, double p2)
{
double y, Ip, tau,at, ac,at, ac, It, Ic, lamb_t, lamb_c, lamb_0,Dc, Dt;
tau=pow(a0,2.0)*rho*cp/(4.0*k);
Dt=kb*delt*p0/(pow(pi,2.0)*eta*k*(1+tau/(2.0*x))*pow(Lt,3.0));
Dc=kb*delt*p0/(pow(pi,2.0)*eta*k*(1+tau/(2.0*x))*pow(Lt/ra,3.0));
Ip=2.0*p0/(pi*pow(a0,2.0));
It=0.51*phi_tc*Ip;
Ic=0.43*phi_ct*Ip;
lamb_0 = (It*(1.+4/5.0*pow(en*rt,2.) + 4/7.0*en*rt+6*Dt/It))/(2.0*(1+2/7.0*en*rt+3.0*Dt/It));
lamb_t = It*(1+4/7.0*rt+6.0*Dt/It);
lamb_c = Ic*(1+4/7.0*rc+6.0*Dt/It);
at=2/5.0*It*rt;
ac=2/5.0*Ic*rc;

y=(ac*(lamb_t-lamb_0)-at*p2*(lamb_0-6.*Dt))/((lamb_t-lamb_0)*(lamb_c-lamb_0))
   *(exp(-lamb_0*x)-exp(-lamb_c*x))
   -at*p2*(lamb_t-6.*Dt)/((lamb_t-lamb_0)*(lamb_c-lamb_0))*(exp(-lamb_t*x)-exp(-lamb_c*x));
return(y);
}

//Define \Delta n function here
double Dn(double x, double eta, double Lt, double p0, double a0, double phi_tc, double phi_ct,
double rt, double rc, double ra, double p2)
{
double y, Ip, tau,at, ac,at, ac, It, Ic, lamb_t, lamb_c, lamb_0,Dc, Dt;
tau=pow(a0,2.0)*rho*cp/(4.0*k);
Dt=kb*delt*p0/(pow(pi,2.0)*eta*k*(1+tau/(2.0*x))*pow(Lt,3.0));
Dc=kb*delt*p0/(pow(pi,2.0)*eta*k*(1+tau/(2.0*x))*pow(Lt/ra,3.0));
Ip=2.0*p0/(pi*pow(a0,2.0));
It=0.51*phi_tc*Ip;
Ic=0.43*phi_ct*Ip;
lamb_0 = (It*(1.+4/5.0*pow(en*rt,2.) + 4/7.0*en*rt+6*Dt/It))/(2.0*(1+2/7.0*en*rt+3.0*Dt/It));
lamb_t = It*(1+4/7.0*rt+6.0*Dt/It);
lamb_c = Ic*(1+4/7.0*rc+6.0*Dt/It);
```

```
at=2/5.0*It*rt;
ac=2/5.0*Ic*rc;

y=(2.*pi*alp/n0)*(
T_0(x,eta,Lt,p0,a0,phi_tc,phi_ct,rt,rc,ra)
*(1+2*rt*T_2(x,eta,Lt,p0,a0,phi_tc,phi_ct,rt,rc,ra))
+0.86*(1-T_0(x,eta,Lt,p0,a0,phi_tc,phi_ct,rt,rc,ra))
*(1+2.0*rc*C_2(x,eta,Lt,p0,a0,phi_tc,phi_ct,rt,rc,ra,p2))-1);
return(y);
}

\\Define n2 function here. Note that ip here is in W/cm^2.

double n2(double x, double eta, double Lt, double p0, double a0, double phi_tc, double phi_ct,
double rt, double rc, double ra, double p2)
{
double y, Ip, tau,at, ac,at, ac, It, Ic, lamb_t, lamb_c, lamb_0,Dc, Dt;
tau=pow(a0,2.0)*rho*cp/(4.0*k);
Dt=kb*delt*p0/(pow(pi,2.0)*eta*k*(1+tau/(2.0*x))*pow(Lt,3.0));
Dc=kb*delt*p0/(pow(pi,2.0)*eta*k*(1+tau/(2.0*x))*pow(Lt/ra,3.0));
Ip=2.0*p0/(pi*pow(a0,2.0));
It=0.51*phi_tc*Ip;
Ic=0.43*phi_ct*Ip;
lamb_0 = (It*(1.+4/5.0*pow(en*rt,2.) + 4/7.0*en*rt+6*Dt/It))/(2.0*(1+2/7.0*en*rt+3.0*Dt/It));
lamb_t = It*(1+4/7.0*rt+6.0*Dt/It);
lamb_c = Ic*(1+4/7.0*rc+6.0*Dt/It);
at=2/5.0*It*rt;
ac=2/5.0*Ic*rc;

y=Dn(x,eta,Lt,p0,a0,phi_tc,phi_ct,rt,rc,ra,p2)/Ip;
return(y);
}

//-----------------------------------------------------------

//This part is the typing available part in nonlinear fitting manu in Origin program.
//Fit parameters have to be assigned accordingly to the functions defined above.

//
void _nlsfDn_DR1_zscan(
// Fit Parameter(s):
double eta, double Lt, double p0, double a0, double phi_tc, double phi_ct, double rt,
double rc, double ra, double p2,
// Independent Variable(s):
double x,
// Dependent Variable(s):
double& y)
{
// Beginning of editable part
y=Dn(x,eta,Lt,p0,a0,phi_tc,phi_ct,rt,rc,ra,p2);
// End of editable part
}
```

Bibliography

[1] S. E. San, O. Koysal, and F. N. Ecevit, "Molecular reorientation-based grating diffraction in dye-doped nematic liquid crystals with red pumping source," Opt. Commun. **212**, 405–409 (2002).

[2] S. E. San, O. Koysal, F. N. Ecevit, S. Ozder, and D. Dvornikov, "Holographic recording study of a hybrid liquid crystal system doped with dye and fullerene," Synth. Met. **142**, 283–286 (2004).

[3] M. D. I. Castillo, J. J. Sanchezmondragon, and S. I. Stepanov, "Peculiarities of Z-Scan Technique in Liquids with Thermal Nonlinearity (Steady-State Regime)," Optik **100**, 49–56 (1995).

[4] T. Catunda, M. L. Baesso, Y. Messaddeq, and M. A. Aegerter, "Time-resolved Z-scan and thermal lens measurements in Er+3 and Nd+3 doped fluoroindate glasses," J. Non-Cryst. Solids **213**, 225–230 (1997).

[5] F. L. S. Cuppo, A. M. F. Neto, S. L. Gomez, and P. Palffy-Muhoray, "Thermal-lens model compared with the Sheik-Bahae formalism in interpreting Z-scan experiments on lyotropic liquid crystals," J. Opt. Soc. Am B **19**, 1342–1348 (2002).

[6] S. Alves, A. Bourdon, and A. M. F. Neto, "Generalization of the thermal lens model formalism to account for thermodiffusion in a single-beam Z-scan experiment: determination of the Soret coefficient," J. Opt. Soc. Am B **20**, 713–718 (2003).

[7] C. R. Mendonca, M. M. Costa, J. Giacometti, F. D. Nunes, and S. C. Zilio, "Nonlinear refractive indices of polystyrene films doped with azobenzene dye Disperse Red 1," Electron. Lett. **34**, 116–117 (1998).

[8] M. Sheik-Bahae, A. A. Said, T. H. Wei, D. J. Hagan, and E. W. Vanstryland, "Sensitive Measurement of Optical Nonlinearities Using a Single Beam," IEEE J. Quantum Electron. **26**, 760–769 (1990).

[9] J. P. Gordon, R. C. C. Leite, R. S. Moore, S. P. S. Porto, and J. R. Whinnery, "Long-Transient Effects in Lasers with Inserted Liquid Samples," J. Appl. Phys. **36**, 3–8 (1965).

[10] J. Brandrup and E. H. Immergut, *Polymer Handbook* (Wiley, New York, 1975).

[11] D. C. Chu, M. Touzelbaev, K. E. Goodson, S. Babin, and R. F. Pease, "Thermal conductivity measurements of thin-film resist," J. Vac. Sci. Technol., B **19**, 2874–2877 (2001).

[12] M. G. Kuzyk, C. W. Dirk, and J. E. Sohn, "Mechanisms of Quadratic Electrooptic Modulation of Dye-Doped Polymer Systems," J. Opt. Soc. Am. B **7**, 842 (1990).

[13] M. Sheik-Bahae, A. A. Said, D. J. Hagan, M. J. Soileau, and E. W. Vanstryland, "Nonlinear Refraction and Optical Limiting in Thick Media," Opt. Eng. **30**, 1228–1235 (1991).

[14] S. P. Bian, W. Y. Zhang, S. I. Kim, N. B. Embaye, G. J. Hanna, J. J. Park, B. K. Canfield, and M. G. Kuzyk, "High-efficiency optical phase conjugation by degenerate four-wave mixing in volume media of disperse red 1-doped poly(methyl methacrylate)," J. Appl. Phys. **92**, 4186–4193 (2002).

[15] M. G. Kuzyk and C. W. Dirk, *Characterization techniques and tabulations for organic nonlinear optical materials* (Marcel Dekker, 1998).

[16] B. E. A. Saleh and M. C. Teich, *Fundamentals of photonics* (Wiley, New York, 1991).

[17] J. C. Liang and X. Q. Zhou, "Application of continuous-wave laser Z-scan technique to photoisomerization," J. Opt. Soc. Am B **22**, 2468–2471 (2005).

[18] R. W. Boyd, *Nonlinear Optics* (Academic Press, 1992).

[19] Z. Sekkat, J. Wood, and W. Knoll, "Reorientation Mechanism of Azobenzenes within the Trans ⇒ Cis Photoisomerization," J. Phys. Chem. **99**, 17 226–17 234 (1995).

Chapter 5

Conclusion

The goal of our work is to understand the mechanisms of the intensity-dependent refractive index in azo dye-doped polymers. The mechanisms are photoisomerization, photothermal heating, and coupling between them.

We generalized the formalism of Akhmanov's self-focusing theory by introducing a variable effective minimum beam waist and calculating the transmittance through a small aperture to model the experiment. For the thermal lens effect, we take the heat source to follow the intensity profile of the laser and thermal diffusion equation. The spatial temperature distribution as a function of time is calculated. Combining our generalized formalism of self-focusing theory with a dimensionless beam width, f, the nonlinear refractive index of the thermal lens effect is calculated.

We model photoisomerization in the off resonance regime, using Sekkat's model as a starting point. We assume that the time scale of our experiment is short enough so that the excitation rate of the cis isomer through photoisomerization from the trans state is higher than the decay rate to the trans isomer. Furthermore, we assume that the molecules start out randomly oriented and that reorientation times are faster than the cis to trans population decay rate. We modified the standard theory by combining a photothermal increase of the temperature and use the Einstein relation for rod-shaped molecules as proposed by Doi and

Edward. This theory predicts that at high temperature, the angular orientation of molecules is randomized, which decreases birefringence of the sample. This prediction is experimentally confirmed in temperature-dependent our OKE experiment.

We developed a TZ-scan experiment to investigate mechanisms of a refractive index change due to light as a function of time. This is a time sequence of Z-scan measurements at fixed time frames. Combining all sequences leads us to the time-dependent refractive index.

In DB14/PMMA, the thermal lens effect is observed. We found that the effective minimum beam waist increases as a function of time, which shows that the thermal lens effect is nonlocal in time and space. Experimentally, we find the increase of the effective minimum beam waist to be comparable to the minimum beam waist without a sample, namely $w_0 \sim \Delta w_0$. The thermal conductivity of DB14/PMMA is deduced from the increased effective minimum beam waist and compared with value for PMMA in literature. A discrepancy of the time constants between theory and experiment is observed, which, we argue, comes from neglect of the boundary at the air-sample interface.

In DR1/PMMA, two dominant mechanisms, photoisomerization (polarization-dependent mechanism) and photothermal effect (polarization-independent mechanism), are found. By comparing the ratio of the nonlinear refractive indices of a linearly and a circularly polarized beam in a TZ-scan experiment, the dominant mechanism is found to be photoisomerization, and the ratio is close to the ratio of quantum yields. From molecular anisotropy parameters, the shape of trans and cis molecules are found to be rod-like 1-D and disk-like 2-D, respectively. Comparing the minimum beam waist for DR1 and DB14/PMMA under the similar conditions, the thermal lens effect in DR1 is not observed, suggesting delayed heating or non-thermal energy release. On the other hand, DB14 molecules have no means to store the photothermal energy so release the energy in the form of heat to polymer in shorter time.